Resistance Band Exoskeleton

Chantheary Lam, Michael Merritt, Patrick Sullivan, Angelo Scala.
The College of New Jersey.

1) User Need

1.a) Use Case: Gait impairment occurs in over 80% of stroke survivors. To address this, NormaGait will assist the impaired portions of gait. The swing phase is critical, as stroke survivors tend to have selective muscle weakness in the shortened range. Users would use this device during rehabilitation under the supervision of a physical therapist.

1.b) Problem Impact: Most gait recovery occurs in the first 6 months and many studies have shown that improvements after require continued effort. Current rehabilitation devices focus on the first six months of recovery, leaving individuals in the chronic phase with limited options. This disconnect leads to a mental and physical plateau in their progression and can have a broader impact on social interaction.

1.c) Scope (Objective): NormaGait will provide a channel for survivors in the chronic phase to continue their recovery/progression toward achieving improved gait.

2) Design Inputs

2.a) Constraints: The device is for chronic stroke patients, who are typically old and overweight. This constraint adds challenges when considering the sizing and compatibility of the device. NormaGait will operate under parameters comparable to a healthy individual, which is seen within all device requirements.

2.b) Requirements: Stroke survivors have increased difficulty during the extension of muscles. Resistance training has increased benefits in stroke therapy. The device must provide 5-10 ft-lbs of musculoskeletal resistance and assistance during flexion and extension respectively. NormaGait allows for a normative knee joint angle during the four phases of walking gait, which translates to a net range of motion of 65º. NormaGait will operate under a maximum angular velocity at the knee joint of 270º/sec during flexion and 280º/sec during extension.

3) Solution

3.a) Design - Intended Use: Linear actuators are used to stretch elastic cables attached to the shin to provide additional torque at the knee. By actuating these cables on top of and underneath the shank, a resistive or assistive torque can be created at the knee during the different walking phases of gait. Initially, a servo motor was thought to be used for this, but because of weight and cost, linear actuators were chosen instead. IMU sensors at the knee and buttons on the sole of the device detect which phase of gait the user is in and the speed they are traveling. With this data, an Arduino will tell the linear actuators when to extend and retract to provide resistance and assistance.

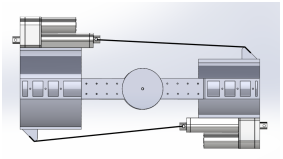

3.b) Build - DEMO:

NormaGait is not fully assembled or functioning yet, however, some of the components are being tested and the results show a promising outcome.

4) Verification Results

4.a) Introduction: NormaGait's design requires two tension cables, one on the anterior side and one on the posterior side of the leg. The cables each apply assistance on one side of the device and resistance on the other as the device cycles through each phase of gait. This protocol was implemented first to research which strength cable would meet the force requirements. Once the ideal cable was determined, it was further tested to understand the force-per-displacement relationship. Ultimately the cable must allow 5-10 ft-lbs of torque at the knee joint by producing 4-8 lbs of force before 4 inches of displacement

4.b) Methods: The first measurement taken was the cross-sectional area of each cable with calipers. A gauge length of 6 inches was measured for each cable to be clamped into the tensile testing machine with a 5 kN load cell. The cable was displaced by ½ inch per second for 8 seconds. The output data was time in seconds, extension in inches, and load in lbf. This data was collected for four trials on the ideal cable.

The cross-sectional area and gauge length were used to generate stress and strain with equations $\sigma=F/A$ and $\varepsilon=L/L$. The acceptance criteria for the cable is in terms of stress and strain is then within 1.5 standard deviations of 191 ft-lbs at .5 in/in.

4.c) Results: For the four trials conducted on the cables, the average stress in the bands at .5 in/in strain was 237.02 +/- 13.06 ft-lbs. Using Origin software, the distribution of the band stresses was found within the acceptance criteria

5) Conclusion

5.a) Summary: With the progress that has already been made, NormaGait is projected to satisfy all said requirements. All materials we have projected to need have been bought and we are still under financial constraints. If further testing calls for additional materials, an extended budget will be requested.

5.b) Revisions: The validation testing could have also been more accurate in regards to purchasing a calibrated device that mimics certain velocities and torques comparably to that of a human. Each mechanism could have been tested under these conditions which lead to less error and higher fidelity.

5.c) Impact (Future Version): NormaGait has the potential to be a high-fidelity rehabilitation device that brings survivors in the chronic phase to their most optimal gait capability. This device will expedite the recovery rate which will facilitate more social interaction and foster more independence.

Acknowledgements We'd like to thank The College of New Jersey for funding this project and providing the space to work on it. We'd also like to thank Dr. Anthony Lau for his continued advising on the project.

Development of a Fully Degradable Suture-Based Electrode for Temporary Peripheral Nerve Stimulation

Danny V. Lam[1,2], Derrick X. Liu[1], Yingyi Gao[1], Elizabeth S. Fielding[1],
Kevin Yang[1], Andrew J. Shoffstall[1,2]
[1]Department of Biomedical Engineering, Case Western Reserve University, Cleveland, OH, USA.
[2]APT Center, Louis Stokes Cleveland VA Medical Center, Cleveland, OH, USA.

Introduction: Advancements in neuromodulation have provided clinicians and researchers the tools to develop therapeutic interventions to various disease models, including chronic pain [1]. Percutaneous leads are widely used for peripheral nerve stimulation (PNS) to manage patient pain in clinical practice [1]. Temporary leads are implanted for 3-7 days to assess potential benefits of PNS. Whether or not pain relief was achieved, the temporary leads are removed. In avoiding potential complications related to lead removal, we developed a fully degradable lead based on bioinert and biocompatible materials with predictable dissolution. In this study, off-the-shelf bioresorbable medical sutures were sputter coated with thin layers of titanium and gold. We showed that the proposed suture-based electrodes are electrically functional for up to 4-weeks on the bench and optimally for 2-weeks *in vivo*. Further refinements to the design are necessary as nerve implants successfully evoked motor responses but failed after a few days. Future studies will look into protective coatings to extend functional device longevity.

Methods: Thin layers of titanium (~5nm) and gold (~100nm) were deposited onto a 5-0 poliglecaprone (PGC) bioresorbable suture via DC magnetron sputtering (Discovery 18 Sputtering System, Denton Vacuum LLC). Electrochemical impedance spectroscopy (EIS) were collected in phosphate buffer solution at 37ºC until device failure via a potentiostat (Interface 1010E, Gamry). Compared to bench measurements, suture-based electrodes were implanted in the subcutaneous space and onto the sciatic nerves of Sprague Dawley Rats (n=4). Charged balanced biphasic pulses (cathodic-leading) were applied to sciatic nerves at submotor threshold with increasing current amplitudes at step size of 0.1 mA. Electromyography (EMG) and electrode impedances were recorded via LabRat (Tucker-Davis Technologies) at ~25kHz and 1kHz, respectively. EMG quantification conducted as time integral within the time window of 1-6 ms after the stimulation artifact.

Results: Samples (n=5) were submerged in PBS at 37ºC for a month. Weekly EIS were collected and averaged to verify electrical function. Electrode impedance in response to 1 kHz were analyzed. Electrodes failed on the bench at 4-weeks (2.22 +/- 1.14kΩ) when compared to baseline measurements (0.07 +/- 0.006kΩ) ($p<0.05$), **Fig. 1A**. In vivo conductivity measurements of implanted electrodes were analyzed for devices in the subcutaneous back (SQ) and on sciatic nerves. Compared to the bench results, implanted electrodes in the SQ were electrically functional for up to 2-weeks prior to failure (4.3 +/- 3.57kΩ) when compared to baseline measurements (2.02 +/- 0.12kΩ). Electrodes implanted on the sciatic nerve had comparable impedances to those implanted on the back (1.50 +/- 0.22kΩ). Visual inspection shows that gold was completely degraded on the electrode's surface at 2-weeks post-implantation, **Fig. 1B**. Although an evoked motor response was achieved in response to increased current stimulation amplitudes, the nerve implants had very poor performance in terms of longevity as most failed in a matter of days, **Fig. 1C**. EMG quantification showed increased motor recruitment in response to current, **Fig. 1D**. We believe the main driver of device failure is in part due to shear strain caused by muscle contraction. Subcutaneous back maintained electrical conductivity for 2 weeks. To prolong functional outcomes of the proposed electrode platform, future studies will investigate additional polymer coatings.

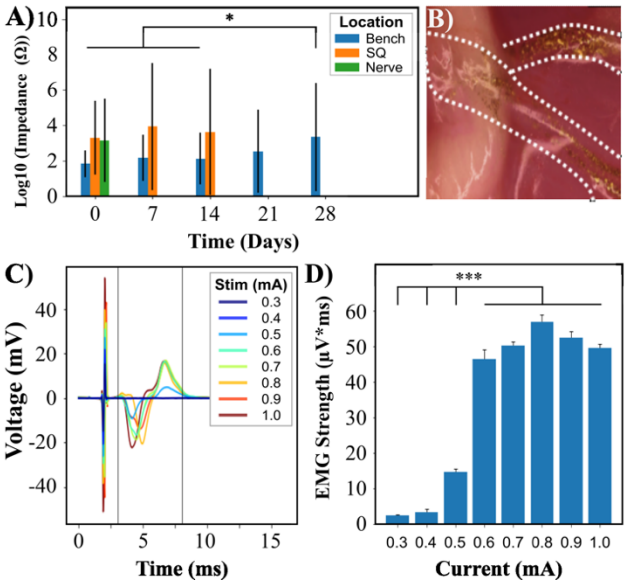

Figure 1: Degradable suture-based electrodes are electrically conductive and functional for weeks on bench and in vivo. A) Impedances at 1kHz from weekly EIS measurements indicated optimal functionality for up to 4 weeks. Implanted electrodes in SQ were stable up to 2 weeks, but were only viable for a few days at the site of stimulation. B) Explant reveal gold has degraded from polymer substrate after 2 weeks. C, D) Evoked EMG showed PNS was feasible with saturation at 0.6 mA ($p<0.001$).

Conclusions: We present a novel electrode design based on bioresorbable suture with low-cost fabrication. Early results show PNS was feasible as the device degrades. We hope to optimize the device for rapid clinical translation in developing temporary neuromodulation applications.

References:

1. Deer TR. et al. Pain Medicine.2020; 21(8): 1590–1603.

Acknowledgements: Funding provided by Case Western Reserve University Startup Funds.

The Role of Hyaluronic Acid in the Synergistic Lubrication of Articular Cartilage

Emily P. Lambeth, David L. Burris, Christopher Price
University of Delaware

Introduction: Articular cartilage is a phenomenal lubricating material, facilitating remarkably low friction coefficients *in vivo* ($\mu \leq 0.005$).[1] Only recently has this unmatched lubricity been replicated on the benchtop, through our redeployment of the convergent stationary contact area (cSCA) testing configuration.[2,3] In the cSCA, sliding promotes speed-dependent, hydrodynamically mediated recovery and maintenance of high fluid load support (FLS), interstitial lubrication (ISL), and low friction values ($\mu \sim 0.03$ in PBS) in cartilage, via a mechanism termed 'tribological rehydration'.[2] If synovial fluid (SF) is introduced into high-speed cSCA studies, truly *in vivo*-like equilibrium frictions ($\mu < 0.004$) are observed.[3] We've termed this frictional benefit, arising from the presence of SF and hydrodynamically driven recovery of ISL by tribological rehydration, 'synergistic lubrication'.

The unanticipated discovery of SF-mediated 'synergistic lubrication' in cSCA contacts raises an important question: what aspect(s) of SF mediate this synergy? SF contains numerous molecules that can influence cartilage lubrication.[3,4] One of these is hyaluronic acid (HA), a high-molecular weight glycosaminoglycan (typically >7MDa) found at concentrations of 1-3mg/mL in SF.[5]

While HA contributes to SF's viscosity[5-7] and has been thought to aid in articular cartilage boundary lubrication[5,8,9], the role of HA in synergistic lubrication is unknown. Here, we explored friction mitigating interactions among hydrodynamics and ISL recovery (titrated through sliding speed in the cSCA) and HA presence (titrated by varying HA concentration and molecular weight [MW]).

Methods: Φ19mm osteochondral explants (n=9/study) were extracted from skeletally mature bovine stifle femoral condyles[2,3] and stored in 1X PBS + sucrose to approximate SF's osmolarity (400mOsm[10]; hereon referred to as PBS).

The effects of HA concentration and MW on cSCA lubrication were investigated using a custom reciprocating tribometer.[2] All explants underwent loading and sliding preconditioning before tribological characterization.

In study 1, sliding "speed sweep" tests were conducted (at 5N) to investigate the effect of HA concentration on cSCA tribology. Explants were sequentially tested at 0, 0.1, 1.5, & 5.0mg/mL HA (1.4MDa in PBS). Sliding conditions (*e.g.*, sliding speed or bath solution) were only changed upon achieving deformation & friction equilibria. In study 2, "speed sweep" tests were performed to explore the effect of HA MW (~30kDa, 375kDa, and 1.4MDa; 3.0mg/mL in PBS) on cSCA lubrication. Equilibrium compressions and kinetic friction coefficients for each condition was recorded in LABVIEW and analyzed in MATLAB.

Results: In a manner unique to the cSCA configuration, the lowest observed equilibrium frictions (μ_{eq}) always occurred at sliding speeds >40mm/s, while peak μ_{eq} values occurred at <5mm/s regardless of HA concentration (**Fig 1A**). Both peak and minimal μ_{eq} decreased with increasing HA concentration (study 1, **Fig 1B,C**), with the lubrication benefit associated with tribological rehydration at high sliding speeds increasing from 8.8-fold in PBS to 25-fold in 5mg/mL HA in the cSCA.

When HA M.W. was varied from ~30kDa to ~1.4MDa (3.0mg/mL; study 2), a further effect of HA M.W. on lubrication synergy was observed (**Fig 1D**).

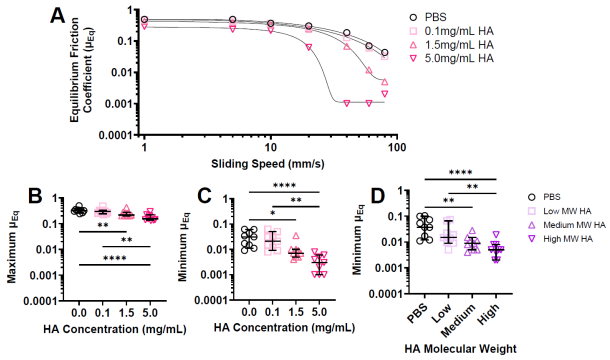

Figure 1: (A) Representative equilibrium friction vs. sliding speed curves for an explant in PBS vs. three HA concentrations (1.4MDa). (B) Maximum and (C) minimum μ_{Eq} at each concentration, and (D) minimum μ_{Eq} at each molecular weight (*p<0.05, **p<0.01, ****p<0.0001; one-way ANOVA).

Conclusions: The cSCA configuration, by precisely titrating FLS and ISL via speed-dependent control of tribological rehydration presents a novel tool for studying HA's and SF's role in mitigating articular cartilage friction.

In the absence of hydrodynamic driven tribological rehydration (*e.g.*, at slow sliding speeds), HA was found to function as a modest, concentration- and M.W.-dependent, boundary lubricant (reducing μ_{eq} by 50%). With increasing sliding-speeds and tribological rehydration, HA's effect on friction evolved dramatically in cSCA explants. Upon the sliding-dependent recovery of FLS and ISL, HA became a tremendously powerful synergistic lubrication partner (reducing μ_{eq} by >95%). These synergistic benefits were HA concentration and M.W. dependent. Most importantly, upon ISL recovery/maintenance by sliding, high concentration high M.W. HA supported vanishingly small μ_{eq} that were at the limit of our detection (μ_{eq} ~0.002) and comparable to those seen with SF.

Overall, the present study highlights the crucial synergy between interstitial hydration and HA-presence in regulating cartilage lubrication under biofidelic sliding conditions (*e.g.*, high FLS and high sliding speeds). These insights continue to advance the development of a unifying framework to explain cartilage's unmatched lubricity *in vivo* and to better understand how cartilage naturally works.

References: [1] Linn *J Biomech* 1968; [2] Moore *OA&C* 2017; [3] Farnham *Trib Let* 2021; [4] Bonnevie *J Biomech Eng* 2020; [5] Fam *Biorheol* 2007; [6] Krause *Biomacromol* 2001; [7] Miyazaki *J Appl Polym Sci* 1998; [8] Ogsten *J Physiol* 1953; [9] Bonnevie *PloS One* 2015; [10] Baumgarten *J Bo Join Surg* 1985.

Mobile Sports Science Lab

Eric Hawkinson, Alex Hemmat, Omar Jack, Conor D. Landry, John F. Drazan, Ph.D
4th Family

1) User Need:

1.a) Use Case

This project is focused on community outreach and service. Our project is focused on designing a new approach to engage underrepresented youth by implementing STEM ideas and designs with sports science applications. This project will design a STEM engagement platform that will seek to build on middle school and teenage student's skills in collaborative working and information literacy while focusing on engaging and informing them on STEM disciplines through the use of equipment designed in this project.

1.b) Problem Impact

Youth participation in STEM activities during their free time encourages and inspires the next generation to pursue careers in the fields of science, technology, engineering and math (STEM). One limitation of existing programs, such as robotics clubs, is that they preferentially engage youth who are already interested in STEM. Therefore, the students most in need of an introduction to STEM, those without a pre-existing interest, are not engaged by these existing programs. This project aims to engage and inspire these students, who have no pre-existing interest in STEM.

1.c) Scope (Objective)

The goal of the kit is to introduce children in the middle school age range to STEM. The devices we are designing utilize sports as a pathway to interest underprivileged youth in subjects they may not have been interested in before. Through our project, we hope to not only design technology and devices that will help develop and build students' interest in STEM; but our focus is to design a new platform and plant a seed in young developing minds that will grow.

2) Design Inputs

2.a) Constraints:

In order to keep the MSSL (Mobile Sports Science Lab) kit cost effective, we have a total estimated cost requirement of $600 per kit, including the devices, software, and shipping. This kit must also be easily shippable to anywhere across the country. It also should be easy to assemble with instructions to make the devices operational.

2.b) Requirements:

The devices should also be more durable than previous iterations as older devices and issues with electrical connections disconnecting. This is so that the kit can be left behind and used for future use by youth, coaches and teachers. The devices must withstand a weight limit of 250 lbs. They should then also be easy to disassemble for storage.

3) Solution

3.a) Design - Intended Use:

The sports science kit, along with the shipping and packing, is intended to be used primarily for STEM outreach programs and after school programs to develop student interest in STEM. The sports science kit must also be easily replicable, which would allow us the possibility to sell and or donate the kits towards after school programs all around the country.

3.b) Build – DEMO

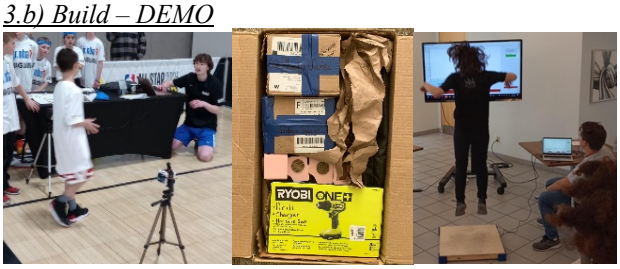

NBA All Star Event, Salt Lake City (Left), Example of packed kit (Middle), ORS Conference, Dallas (Right)

4) Verification Results

4.a) Introduction

Our kit was deployed at four you events across the country (Hawaii, Arizona, Dallas, Salt Lake City). The requirments for these kits were that it had to be transported through air travel without complications, the kit could be easily assembled on site, and be able to successfully engage local youth students at every outreach event.

4.b) Methods

Measurements for the kit were primarily observational, i.e whether the kit travelled successfully, if it was able to be easily assembled and if the outreach events were run successfully without major issues. We would also engage with participants to determine if they had an improved interest in STEM and enjoyed using our devices.

4.c) Results

The kit preliminary tests (Hawaii and Arizona) were successful such that the devices functioned as intended. The two main tests were the events ran Dallas and Salt Lake City, both of which were massive succesess.

5) Conclusion

5.a) Summary:

Our kit was successful. It travelled well, successfully going to four events across the country and back safely to Fairfield, Connecticut. On-site assembly was simple and easy without the use of power equipment. Running tests and experiments with the kit was easy and every student we had use the devices were engaged. Many students would also ask follow-up questions about the kit and STEM ideas.

5.b) Revisions:

Light box and toe tapper need structural updates.

5.c) Impact (Future Version):

This kit has the potential to inspire millions of kids all over the country to consider career paths in STEM fields. This project specifically aims to inspire those who do not come from a STEM background, those that had no prior interest in STEM. This will position a new generation of youth to consider and persue STEM careers. The low cost portability and replicability of the kit will also make it incredibly accessible.

Acknowledgements: NBA Cares, WNBA, NBA G-League, Microsoft, Forth Family, Fairfield University, Orthopedic Research Society

Variable Frequency OPEP Device for Improved Airway Secretion Removal

Matthew Lange, Leonardo Campos, Hannah Matin, Julia Zhao, Skylar Li, Athena Tsu
Department of Biomedical Engineering, Columbia University, New York, NY

1) User Need:

1.a) Use Case

This device is designed for patients with pulmonary diseases like bronchiectasis, cystic fibrosis, COPD, and other respiratory issues that cause mucus buildup in the airways. Utilizing airway vibrations powered by the patient's own breath, the device breaks up mucus and phlegm, making it easier to expel the retained secretions.

1.b) Problem Impact

For all existing devices, there exists minimum requirements for a person to operate such a device, entailing threshold flow rates and pressures provided by the user, thus excluding individuals with more severe respiratory conditions who may arguably be in greatest need of such devices [1]. In addition, the mechanical nature of such devices leads to variability in the operational frequency, peak pressure, and pressure amplitude which can thereby lead to variability in therapeutic effect for each device, convoluting the treatment process for an individual [1]. Beyond variability, these factors are highly interrelated and each device suffers from a sacrificial nature regarding optimization [1]. Frequency determination is also necessary for optimal mucus breakup, but this process is complicated by unintuitive means of adjusting the angle of the device or resistance dials.

1.c) Scope (Objective)

This device aims to address the shortcomings of current market OPEP devices, specifically the lack of precise frequency calibration and continuous frequency control. Existing devices do not offer options for optimal frequency calibration, despite the fact that there is a spectrum of frequencies that promote mucus breakup and secretion movement, dictated by natural cilia vibrations. By incorporating a variable-frequency system, patients can better match these frequencies, resulting in more efficient treatment.

2) Design Inputs

2.a) Constraints:

The device must be portable and easy to use, and not rely on the patient's expiratory capacity to maintain oscillations. The valve is controlled electronically to maintain the desired oscillatory frequency, making it accessible to patients with weaker breathing capacities. Portability is a priority to encourage consistent use, and weight minimization is important to address physical strain, especially for elderly patients who typically use market OPEP devices for 15-20 minutes at a time.

2.b) Requirements:

The device's central function is to vary the oscillatory frequency, achieved through electronic control of a solenoid valve. The device's frequency range is limited to match that of existing OPEP devices (10-30 Hz), but it has the capacity to oscillate outside this range if further testing proves it beneficial and safe. Patients can easily manipulate the frequency range through a knob and a display shows the current frequency in use.

3) Solution

3.a) Design - Intended Use:

Our device is intended to be used similarly to established commercially available devices, with the patient blowing into the device to initiate the oscillation. Frequency and pressure amplitude are actively controlled using an electronic solenoid-valve programmed to open and close at a baseline frequency. This frequency can be manually tuned by the user for patient-specific optimization using a knob, which is readily displayed on an LCD screen.

3.b) Build - DEMO

We have produced a prototype that satisfies our design constraints and requirements. Specifically, the device has tunable oscillation frequency in the 10-30 Hz range and generates sufficient pressure in the airways. We are finalizing an outer case and potential additional functionalities.

4) Verification Results

4.a) Introduction

Initial proof of concept testing requires our device to generate sufficiently similar pressure vs. time profiles as the Flutter, the current standard of care.

4.b) Methods

Measurements of pressure (psi) versus time (s) were recorded for both the Flutter and our device with a digital pressure sensor and Arduino. Constant laboratory airflow was provided to simulate patient exhale. Data collection occurred over a time interval of 60 seconds per round, with 10 repetitions for each device. Baseline (initial) pressure was subtracted for each fluctuation and the resultant dataset was tested with a t-test to determine statistical significance.

4.c) Results

We are currently collecting final results for our verification experiment.

5) Conclusion

5.a) Summary:

Creation of a device with automated opening and closing at an adjustable frequency was successful in addition to the LCD implementation. We did observe frequency and pressure amplitudes within therapeutic ranges comparable to those of established devices. Further tests determining effectiveness at mucus breakdown are needed.

5.b) Revisions:

Future iterations may seek to include a system for increasing pressure buildup at the valve interface. This may be potentially achieved using a diaphragm system that artificially increases pressure via changes in volume.

5.c) Impact (Future Version):

Thus far, we've tested our device against breathing comparable to mild COPD patients or those with mild symptoms of occluded airways. This additional aspect may increase the breadth of patients that may utilize the device by reducing patient expectations to achieve the necessary pressure or pressure amplitude.

References:

1. Fleet HV et al. 2017 Respiratory Care 62 (4) 451-458

Acknowledgements: Columbia University Department of Biomedical Engineering

Hybrid Continuous Flow Pediatric Total Artificial Heart: Pumps, Magnetics & Motors

Jonathan Lawley[1], Matthew D. Hirschhorn[2], Arthur P.T. Johnson[2], Andrew J. Roof[2], Vakhtang Tchantchaleishvili[3], Randy Stevens[4], Steven W. Day[1], Amy L. Throckmorton[2]

Rochester Institute of Technology[1]; Drexel University[2]; Thomas Jefferson University[3]; St. Christopher's Hospital for Children[4]

Introduction: To address the unmet clinical need for pediatric circulatory support devices, we are developing an operationally versatile, hybrid, continuous-flow, total artificial heart (*Dragon Heart)*. A compact design is accomplished by using a centrifugal pump that uniquely encompasses an axial pump to support each side of the heart. Both pumps share a common rotational axis and utilize third generation magnetic suspension and motor drive systems.

Methods: A previously validated axial flow pump was utilized, thus here we focused on development of the centrifugal blood pump. We performed simulations of the pump regions using computational fluid dynamics (ANSYS CFX) as well as of the motor components using magnetic finite element analysis (COMSOL). A hybrid centrifugal pump prototype was constructed by bio-compatible 3-D printed parts and machined metal parts. Testing was initially conducted using water and then bovine blood. Finally, the fully combined nested device was tested to ensure proper operation when the two pumps were used in tandem.

Results: The centrifugal prototype was able to achieve target pressure-flow requirements for pediatric circulatory support. The new 3-phase brushless DC motor design led to a reduction in the motor's size relative to prior iteration and improved portability. The fluid and magnetic models have shown to be a valid form of predicting the behavior of these two domains. Furthermore, we demonstrated the performance of the two nested pumps operating in tandem and found that neither pump was adversely impacted by the simultaneous operation.

Conclusions:
The current iteration of the Dragon Heart centrifugal pump design achieved a wide range of operating conditions, including our target physiological range. Future design iterations will further reduce the overall footprint of the design and incorporate active magnetic levitation.

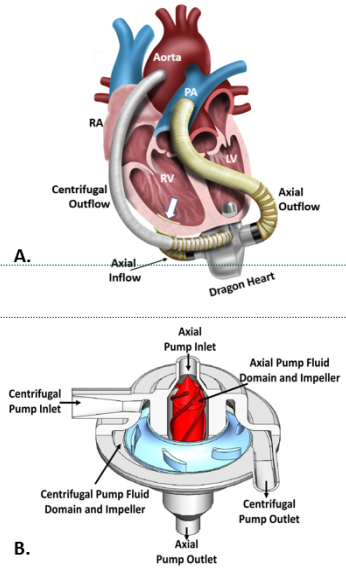

Figure 1. **Hybrid, Continuous-Flow, Magnetically Levitated, *Dragon Heart* TAH.** A. Implantation of the *Dragon Heart* Technology. The centrifugal blood pump is designed to support the systemic circulation and the left ventricle, and the axial flow blood pump is designed to support the pulmonary circulation and the right ventricle. RA: right atrium; RV: right ventricle; LV: left ventricle; PA: pulmonary artery; B. TAH design details of the integrated axial and centrifugal pumps into a single device having with only two moving parts, the magnetically levitated impellers.

Acknowledgements: Funding has been provided by the NIH NHLBI R01HL153536 grant.

Deleted: (1)

Deleted: and (2)

Robust modRNA-based Gene Editing and Epigenetic Activation systems for human stem cells

Xiaojun Lance Lian, Tahir Haideri, Alessandro Howells
The Pennsylvania State University

Introduction:

CRISPR systems, including Cas9, base editors (ABE or CBE), and dCas9-based epigenetic activation (dCas9-VPR, dCas9-VP64+MPH), have revolutionized biomedical research because they offer an unprecedented opportunity for genome editing and altering cell fate in human stem cells. Most genetic variants that contribute to disease can be corrected by Cas9 or base editors. However, a bottleneck of applying CRISPR systems in human pluripotent stem cells (**hPSCs**) is how to deliver large CRISPR effectors into hPSCs easily and efficiently.

Methods:

Cas9, ABE8e, or dCas9-based epigenetic effector DNA was PCR amplified using appropriate primers. The PCR product was run on a 1% Agarose gel and the band at the appropriate size was excised and the DNA extracted using the ZymoClean Gel DNA Recovery kit. Purified insert DNA was cloned into our linearized modRNA plasmid using the In-Fusion Cloning Kit. The DNA template for modRNA synthesis was PCR amplified from the successfully cloned modRNA plasmid followed by PCR purification using DNA Clean & Concentrator-5. ModRNA was synthesized from the PCR DNA template via in vitro transcription (IVT) using the MEGAscript T7 Transcription kit supplemented with N1-methyl-pseudo-UTP, and Cap 1. The IVT reaction product was treated with DNase I to remove DNA template and then purified using the MEGAclear transcription clean-up kit. RNA concentration was measured using the NanoDrop.

Results:

We developed chemically modified mRNA (modRNA)-based CRIPSR systems that utilized a Cas9 and a p53 dominant-negative fragment (p53DD) modRNA for the purposes of knocking out genes in hPSCs. Our modRNA vector contained 5'UTR and 3'UTR from beta-globin gene, a Cap 1 structure (CleanCap AG), and a poly(A) tail (120 As). Importantly, we used N1-methyl-pseudo-UTP to completely replace UTP during modRNA synthesis. All of these contributed to better modRNA with improved stability and less immunogenicity.

With our modRNA CRISPR-Cas9 system, we achieved up to 84% knockout efficiency across multiple genes (GFP, CD90, CTNNB1) and multiple hPSC lines. We also used base editor (ABE8e) modRNA to disrupt the splice donor site of the B2M gene, resulting defective splicing of B2M transcript, and ultimately leading to B2M knockout. We achieved 69.6 ± 3.8% B2M knockout efficiency using ABE8e modRNA, while plasmid-based method only achieved 12.3 ± 2.2% knockout efficiency (**Fig 1**).

To directly program hPSCs into desired somatic cell lineages, we used modRNA-based epigenetic activation system and robustly activated several key transcription factors (SOX17, PDX1, MAFA) in hPSCs (**Fig 2**).

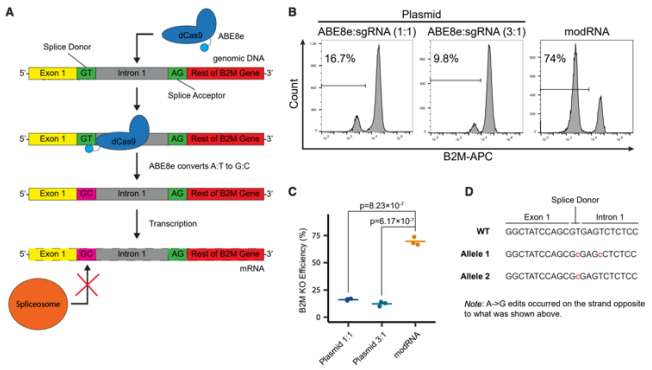

Figure 1. ModRNA ABE8e is more efficient over plasmid-based method. A) Schematic of modRNA base editing. B-C) B2M knockout efficiency measured by flow cytometry. D) Genome sequencing of mutated cells.

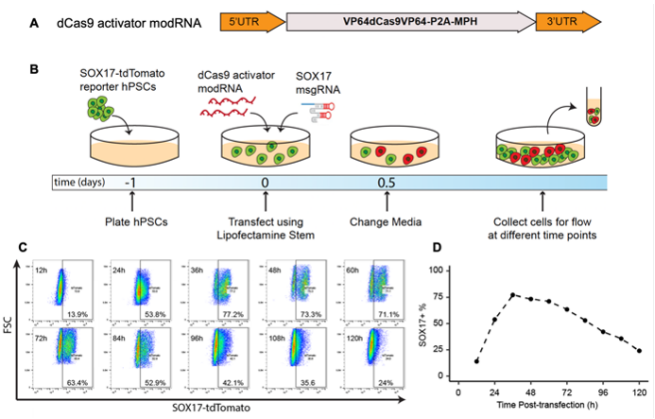

Figure 2. **ModRNA-based epigenetic activation system in hPSCs**. A) Schematic of dCas9 activator modRNA. B) Schematic of experimental steps. C) Cells harvested at different time points were subjected to flow cytometry of tdTomato expression. D) Quantification of results present in panel C.

Conclusions: In summary, we demonstrate that our non-integrating modRNA-based CRISPR methods hold great promise for genome editing and cell fate engineering of hPSCs.

References:

Haideri et al., ***Cell Reports Methods*** 2, 100290, 2022

Acknowledgements: This work was supported by NIH NIBIB R21EB026035, NIH NIAMS R01 AR072731, NSF CBET-1943696, NSF CBET-2143064, and Penn State startup funding.

Novel Bioreactor for Enhanced Fluid Flow and Electrical Stimulation of Engineered Cardiac Tissues

Joseph P. Licata, Jonathan A. Gerstenhaber, Yah-el Har-el, and Peter I. Lelkes
Temple University, Department of Bioengineering

Introduction: The process of differentiating stem cells into matured excitable tissues, such as cardiac or neural tissue, can be aided by exposure to electrical stimulation (ES)[1]. These excitable tissues seem to benefit most from periodic exposure to a uniform electric field. Since stem cell differentiation procedures include both 2D and 3D cell culture, we have aimed to develop a bioreactor that will be usable in both situations. It is well known that cells, especially those in 3D tissue constructs, benefit from fluid flow to increase nutrient and oxygen availability to the cells[2]. However, high shear can often be detrimental to cell development.

In this work, we are developing a bioreactor capable of both electrical stimulation and low-shear fluid flow for enhanced differentiation and maturation of stem cells into cardiomyocytes (CMs). Our device is designed to be 3D-printed using low-cost materials and inserted into a standard 6-well tissue culture plate, making it inexpensive and easy to use.

Results:

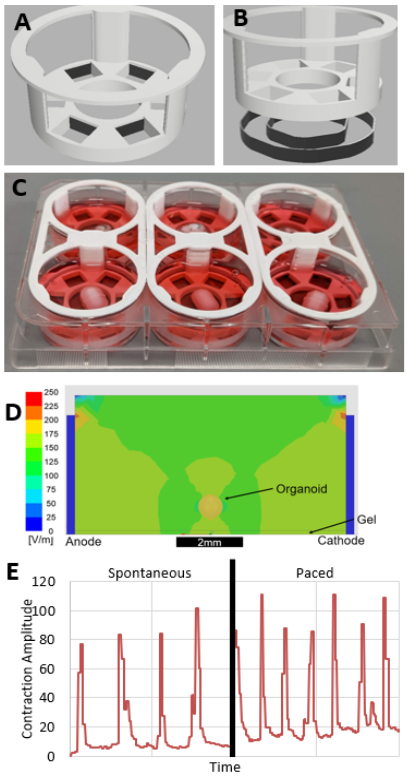

Figure 1. A) Bioreactor CAD model. B) Exploded CAD model showing electrode placement. C)Assembled bioreactor in 6-well plate, with stir bars in place. D)Electric field modeling, cross-section of a single mini-well. Modeling includes electric field within an organoid in the center of the well. E) Cardiomyocyte pacing in the bioreactor, showing increased beating rate when stimulation is applied.

We designed a bioreactor to "drop-in" to either a standard 6-well plate or 35mm petri dish. This bioreactor consists of "mini-wells" in a circular pattern, each about the size of a 96-well plate single well, with a large center chamber for high speed mixing. A stir bar inserted into the center chamber is used for media mixing. The separation between the mixing chamber and mini-wells reduces the shear stress on cells, while still allowing enhanced nutrient availability to the cells. Mini-wells have electrodes on the inner and outer walls to enable electrical stimulation of cells with a homogenous and symmetrical electric field.

Computational modeling of both electric stimulation and fluid flow was performed in Ansys, with subsequent technical validation experiments performed to validate the computational modeling and assess actual conditions within the bioreactor. For these evaluation studies, we used dye tracing assays to estimate fluid flow and electrical measurements to assess the electric performance. Cardiomyocytes were derived from human induced pluripotent cells (hiPSCs) and cultured in the bioreactor under electrical stimulation, starting at day 7 after initiation of differentiation. Analysis on day 10, the cells showed an increase in beating rate, following the pacing, when compared to non-paced conditions, showing cell reaction to electrical stimulation. Preliminary results have also shown that electrical stimulation in the bioreactor enhances contraction speed coordination throughout the cardiac tissue construct, an important indicator of cardiac tissue maturation. We will show comparative analysis between cells grown with and without stimulation using flow cytometry and fluorescent imaging.

Conclusions: We have designed and constructed a novel bioreactor capable of both low shear nutrient transfer and consistent electric stimulation of hiPSC derived cardiac tissue culture constructs. Computation modeling has shown homogenous electric fields within the cell culture areas, and adequate low-shear flow for nutrient mixing in the same areas, and these have been validated with practical testing. Next steps for this device will include optimizing different ES regimes and fluid mixing speeds. We expect to see enhanced growth and maturation of cardiac organoids due to optimized electrical stimulation and nutrient availability due to increased flow. Our long-term goal is to direct differentiation, maturation, and subtype determination of cardiomyocytes using ES and to enhance the growth and maturation of 3D cardiac organoids.

References:

1. Ronaldson-Bouchard. Nat protocols, v.14 Oct 2019, DOI: 10.1038/s41596-019-0189-8
2. Goto-silva. BMC Dev Biol 19, 3 (2019). https://doi.org/10.1186/s12861-019-0183-y

Acknowledgements: Thanks to Temple University for their support via the Temple University Presidential Fellowship.

Tendon Overload Using A Rodent Model Of Synergistic Ablation Leads To Mechanical Degeneration

L.M. Lin[1], E.T. Bloom[1], J.M. Peloquin[1], M.H. Santare[1], J. Parreno[1], K.G. Silbernagel[1], D.M. Elliott[1]
[1]University of Delaware, Newark, DE

Introduction: Tendon degeneration is widespread and asymptomatic until later stages, making it difficult to determine mechanisms that lead to degeneration, therefore animal models of altered loading are needed. Most animal models cause tendon degeneration by overuse, such as treadmill running. [1] However, many tendon disorders are related to overloading, not overuse, thus, we recently established a rodent overload model of synergist ablation (SynAb). The Achilles tendon was resected, overloading the synergist plantaris tendon, without increasing the number of loading cycles.[2,3] We showed multi-scale structural changes associated with tendon overload, such as an increased cross-sectional area (CSA), increased fibril diameter and density, increased cell density, and decreased collagen alignment. While these outcomes suggest tendon degeneration, it was unclear whether the degeneration was induced exclusively from structural changes. As such, it was necessary to evaluate mechanical changes of tendon following overload, as a decrease in stiffness and strength is a key hallmark of tendon degeneration. Therefore, the objective of this study was to investigate the mechanical changes induced by tendon overload. We hypothesized that there would be a decrease in mechanical properties at 8 weeks post-surgery, indicating tendon degeneration.

Methods: Bilateral plantaris tendons from 7-month-old female Long Evans rats were randomly assigned to three groups: SynAb (Achilles resected to overload plantaris), Sham (incision made but Achilles not transected), and Intact (n=6 tendons/group). At 8 weeks post-surgery, rats were sacrificed and stored in a -20°C freezer until the day of testing. Each rat was thawed at room temperature and the plantaris tendons were dissected. Each tendon was gripped and mounted on a uniaxial device. [4] The sample was preloaded to 5mN and preconditioned for 5 cycles between 0 and 5% strain. Testing included 1) a Ramp and Hold at 25% strain for 10 minutes, unloaded to reference length for a 15-minute recovery, and 2) Ramp to Failure. All loading and unloading rates were 1%/s. The stress-strain curves were analyzed for transition point, yield point, failure point, and linear region modulus. Non-parametric t-tests were performed between the Intact and Sham groups and there was no difference between the groups for any of the parameters, so they were combined as one Control group to compare with the SynAb group. Differences in material properties were analyzed using Mann-Whitney t-tests. All material properties were compared between treatment groups and the linear region modulus and transition point were additionally compared between Ramp & Hold and Ramp to Failure.

Results: The modulus in SynAb was 54% lower than Control in the Ramp & Hold and 47% lower in the Ramp to Failure ($p<0.05$), but there were no differences in modulus between ramps (Fig 1A). There were no differences in the transition strain between the treatment groups or loading ramps ($p>0.6$). The transition stress in SynAb was 41% lower than Control during the Ramp to Failure ($p=0.02$) and the transition stress was 52% higher during the Ramp & Hold than the Ramp to Failure in the Control group ($p=0.03$, Fig 1B). Yield and failure strain were not statistically different between the treatment groups, however, the SynAb yield stress was 52% lower than Control ($p=0.07$, Fig 1C) and the SynAb failure stress was 65% lower than Control ($p=0.08$, Fig 1D).

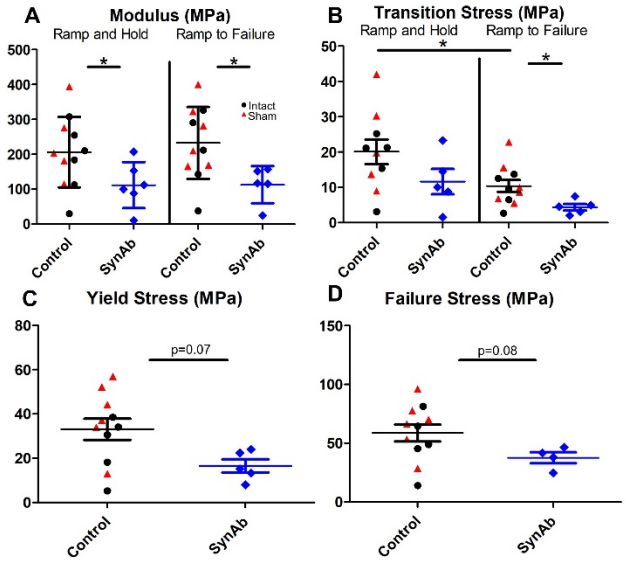

Figure 1: Tendon A) Modulus, B) Transition stress, C) Yield Stress, and D) Failure stress * indicates $p<0.05$

Conclusion: This study showed degenerative mechanical changes following 8 weeks of tendon overload from synergistic ablation in a rat model. Specifically, we observed a decrease in modulus in the SynAb group indicating that increasing mechanical load from SynAb impairs mechanical function. The decrease in modulus could be caused by the observed decrease in matrix organization and collagen alignment from our previous work using the SynAb model. [2,3] The yield stress and failure stress also decreased, with trending significance, likely due to the limited sample size. The mechanical and structural outcomes in our SynAb overload model are similar to the outcomes observed in overuse treadmill running models. [1] Although both model types cause a degenerative change in mechanical and structural properties, the mechanisms leading up to this degenerative state and the clinical manifestations (rupture versus painful tendinopathy) may be different. Therefore, we will use the SynAb model of tendon overload in future work to explore these potential mechanisms and the progression of these degenerative changes.

References: 1. Hast, M et al., *Bone Joint Res;3:193–202.2014* 2. Bloom E., et al. *ORS Abstract 2022* 3. Lin L., et al. *BMES Abstract 2022* 4. Bloom, E., et al. *Biomed Eng;49:1058–1068*. 2021

Acknowledgements: Funding for this research was provided by NIH/NIAMS R01 AR080059-01 & NIH F31 AR078005-02.

Newly-synthesized Glycoprotein Profiling to Identify Molecular Signatures of Warm Ischemic Injury in Donor Lungs

Zihan Ling[1,+], Kentaro Noda[2,+], Brian L. Frey[3], Michael Hu[1], Shierly W. Fok[1], Lloyd M. Smith[3], Pablo G. Sanchez[2,*] and Xi Ren[1,*]
[1]*Department of Biomedical Engineering, Carnegie Mellon University, Pittsburgh, PA 15213, USA*
[2]*Division of Lung Transplant and Lung Failure, Department of Cardiothoracic Surgery, University of Pittsburgh, Pittsburgh, PA 15213, USA*
[3]*Department of Chemistry, University of Wisconsin, Madison, WI 53706, USA*
[+]*Equal contribution*
[*]*Correspondence*

Introduction: Lung transplantation (LTx) is the ultimate treatment for end-stage respiratory diseases. However, due to warm ischemia injury (WII), lung grafts are susceptible to developing primary graft dysfunction following LTx. *Ex vivo* lung perfusion (EVLP) has been developed as a robust platform to sustain lung graft metabolism and function between procurement and transplantation but current LTx outcomes remain unsatisfactory. New therapeutic developments are hampered by limited understanding of pathogenic mediators of ischemic injury to donor lung grafts. While transcriptomic analysis has been useful to uncover temporal-specific expression, it remains unclear how this is correlated with the production of proteins that ultimately mediate the bulk of cellular activities. Traditional proteomic analysis using mass spectrometry detects proteins with probabilities proportional to their abundances and falls short in identifying de novo protein synthesis due to the highly abundant pre-existing protein background. Here, to identify novel proteomic effectors underlying the development of lung graft dysfunction, using bioorthogonal protein engineering, we selectively captured and identified Newly Synthesized glycoproteins (NewS-glycoprotein) produced during EVLP with unprecedented temporal resolution of 4 hours.

Methods: In this study, we administered Ac_4GalNAz, an azide-bearing galactosamine analog to lung grafts with or without prior WII during 4-hour EVLP to label NewS-glycoproteins. (Fig 1) The lung proteins were extracted, reacted to alkyne-PEG4-Desthiobiotin under copper-catalyzed cycloaddition (CuAAC) condition, precipitated and re-dissolved in SDS buffer to remove extra Desthiobiotin reagents. The protein samples were then pulled down by streptavidin resins and eluted with free biotin. The eluates were analyzed by liquid chromatography-tandem mass spectrometry (LC-MS/MS) for proteomic characterization. Upon identifying a few differentially expressed glycoproteins between WII and control lung grafts, we found two proteins upregulated in WII lung with close connection to calcineurin pathway. We administered cyclosporin A (CyA), a calcineurin inhibitor to the WII lung grafts during EVLP and assessed lung function 2 hours post-LTx.

Results: We first observed robust azide labeling signal on lung grafts administered with Ac_4GalNAz during 4-hour EVLP, in comparison to vehicle control. Our results also suggested that Ac_4GalNAz administration did not alter lung morphology, compliance, or vascular resistance throughout the EVLP. Our streptavidin western blot and total protein staining also showed efficient pull-down and release of desthiobiotinlyted glycoproteins with the streptavidin resins. Comparing the eluate samples between Ac_4GalNAz-labeled and vehicle control groups, we identified 1984 proteins with significantly higher abundance in Ac_4GalNAz-lung samples, and thus focused on these proteins in the comparison study. We then validated the WII model and observed unaffected lung compliance and vascular resistance during EVLP, but significantly reduced PiO_2/FiO_2 (P/F ratio) 2 hours after LTx, as compared to non-WII controls. We then implemented the NewS-glycoproteomic approach to the WII lung grafts and compared the NewS-glycoproteomes between WII and non-WII control and identified 7 proteins upregulated and 23 proteins downregulated during EVLP in WII lung grafts. 2 of the 7 upregulated proteins, Ppp3r1 and Ca8 were associated with calcineurin pathway as suggested by a few studies. Upon treating the WII lung grafts with CyA during EVLP, we observed attenuated lung inflammation, elevated P/F ratio, and reduced pulmonary edema 2 hours post-LTx.

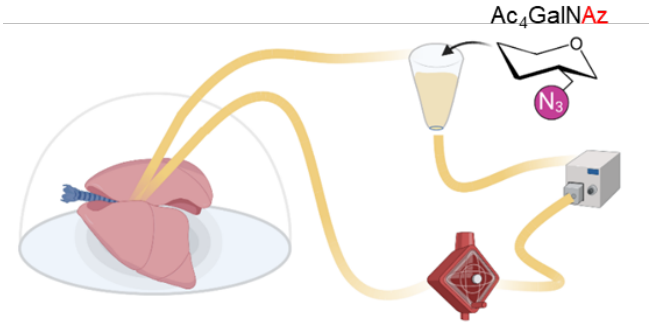

Figure 1. Ac_4GalNAz administration during EVLP to label newly synthesized glycoproteins.

Conclusions: In this study, we established the feasibility of effective bioorthogonal protein labeling during EVLP, enabling chemoselectively enrichment and profiling of Newly Synthesized (NewS)-glycoproteins within donor lungs. The reported analytical pipeline allowed sensitive detection of *de novo* protein synthesis during EVLP with unprecedented temporal resolution of 4 hours by the highly abundant pre-existing protein background. Comparing the EVLP-NewS glycoprotein profiles between control and ischemic lungs, we identified 7 upregulated and 23 downregulated NewS-glycoprotein signatures associated with WII. Inspired by these discovered protein signatures, we showed that inhibition of the calcineurin pathway during EVLP offered protection to lung grafts with prior exposure to WII.

Acknowledgements: This work is supported by National Institute of Health. Z.L. is partially supported by scholarships from the China Scholarship Council. We thank Pitt Biospecimen Core for histological processing.

Functional Grasp Training using Mixed-Mode Reality after Spinal Cord Injury

Mingxiao Liu[1], Samuel Wilder[1], Sean Sanford[1], Sophie Dewil[1], Noam Harel[2], Raviraj Nataraj[1]
[1]Department of Biomedical Engineering, Stevens Institute of Technology, Hoboken, NJ, USA
[2]Spinal Cord Damage Research Center, James J. Peters VA Medical Center, Bronx, NY, USA

Introduction: Spinal cord injury (SCI) can impair the hand function needed for activities of daily living. Physical therapy is crucial to rehabilitating function but is time- and effort-intensive. Thus, advanced training approaches that foster engagement and leverage cognitive factors, e.g., the sense of agency [1], are needed to accelerate motor learning. In a previous study [2], we established how training with *augmented feedback* (i.e., providing sensory cues to inform the user when a "secure" grasp was achieved) from an instrumented glove with computational intelligence improved functional performance. In this study, we newly created a mixed-mode environment that adds virtual reality to enhance the feedback further. Furthermore, we assessed the effects on persons with SCI in this study.

Methods: Six persons with incomplete cervical-level SCI participated in this study after signing informed consent forms approved by the Bronx VA Medical Center IRB. Each participant wore a 64-channel scalp-surface cap for EEG recording (Brain Vision) and our custom-built instrumented glove with force and flex sensors. The experimental procedure asked participants to perform a grasp-and-place task of a small cubic object onto a designated target (Fig. 1). Participants executed three blocks of trials: *1)* an initial block of 15 trials without feedback to establish baseline performance (i.e., "pre" training), *2)* a block of 30 trials to train with augmented feedback (audio and visual) about secure grasp at progressively shorter time intervals to induce intentional binding, an implicit measure of agency [3], *3)* a block of 15 trials without feedback to determine effects after (i.e., "post") training. During training, participants received feedback cues upon and during secure grasp. The three blocks of trials were repeated for three different feedback conditions. For "Glove Feedback," an onboard beeper and LED were activated during secure grasp. For "VR Feedback," participants experienced mixed-mode reality whereby they viewed a VR environment (Unity) through a headset (HTC Vive with LEAP) while continuing to grasp a real object. Participants observed virtual representations of the object and the grasping hand in VR. The VR-enhanced audio and visual feedback cues were provided through earpiece sounds and changing the virtual object's color from red to green. Participants also completed a "No Feedback" condition (control case) with no additional feedback about grasp during training.

Results: Training feedback with VR produced a significant ($p<0.05$) improvement (reduction) in completion time and motion pathlength compared to no feedback (Fig. 2). Glove feedback demonstrated intermediate results with inconclusive differences. Feedback with VR also significantly increased average alpha band activity across all EEG channels. Alpha activity changes were especially notable in the primary motor cortex and sensorimotor regions [4].

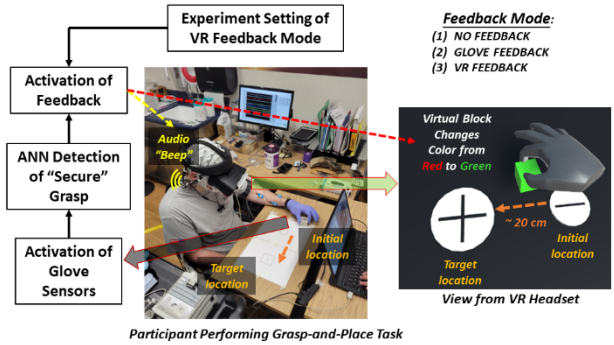

Figure 1. The experimental flow of participant training to perform a grasp-and-place task in mixed-mode reality.

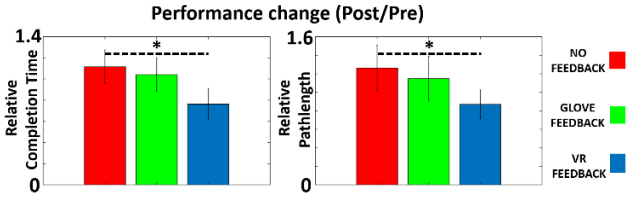

Figure 2. Relative change in performance metrics from pre- to post-training with augmented feedback.

Conclusions: Our results suggest that training with augmented feedback enhanced in VR could support improved grasp training for persons with SCI. Furthermore, a concurrent increase in alpha-band EEG activity, especially in brain regions associated with sensorimotor adaptations, may offer a clear neural basis for this phenomenon. Specifically, increases in alpha-band activity can suggest early consolidation of motor learning features from a pre-learning state [5]. Thus, augmented feedback provided with VR appears to be a potentially valuable tool for rehabilitating motor function after SCI. Furthermore, our study's results should motivate future investigations into leveraging cognitive factors for motor rehabilitation through computerized interfaces. Such paradigms could readily optimize how training feedback is provided to individual users to maximize movement performance and cognitive outcomes jointly [6].

References:

1. Moore J.W. et al. Front. Psychol. 2016;7.
2. Liu M. et al. Sensors. 2021;21(4):1173.
3. Moore J.W. Cons & Cog. et al. 2012; 21(1): 546-561.
4. Riemann B. et al. J. Athl. Train. 2002;37(1): 71-79.
5. Henz D. et al. Front. Behav. Neurosci. 2016 10:199.
6. Nataraj R. et al. Front. Human. Neurosci. 2020;14.

Acknowledgements: The authors acknowledge support from the Stevens Schaefer School of Engineering and Science and funding by the Department of Veterans Affairs (grant no. I21 RX003582-01).

Sensor-Based Aviation Headset for Pilot Safety

Jacob Loranger, Anna Johnson, Maher Alsamsam, Emily Hanscom, Michael Mason, PhD
Department of Biomedical Engineering, University of Maine

1) User Need:

1.a) Use Case:

The purpose of this device is to obtain, analyze, and convey information to non-commercial pilots, thus improving communication to provide preventative and diagnostic measures for emergencies.

1.b) Problem Impact:

Currently, no existing products evaluate cabin condition and pilot health for post-accident investigations. This would be beneficial, given that medical factors are found to cause up to 8% of fatal general aviation accidents.

1.c) Scope:

The goal of this project is to build a device that allows pilots to access biometric and environmental data mid-flight. An integrated sensor system interfaces with an iOS application to analyze and display information.

2) Design Inputs:

2.a) Design Constraints:

The FAA requires aircraft devices to be battery-powered and have enclosed electronics. Devices that collect and store biometric information must comply with HIPAA regulations. Ideal ergonomic design is necessary for comfort during extended use.

2.b) Design Requirements:

The sensor-system must transmit data to the iOS application via bluetooth. Real-time analysis of data should be displayed with alerts within the iOS application. The device must connect to a remote server to store data globally for diagnostic purposes.

3) Solution:

3.a) Build - DEMO:

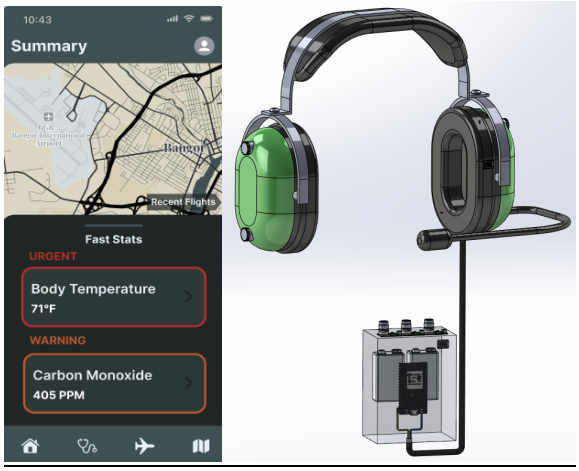

Figure 1. Example user-interface (left) and sensor system CAD model (right).

3.b) Design - Intended Use:

The hardware consists of a microcontroller, thermistors, accelerometers, gas sensors, and an electret microphone to record body and cabin temperature, breathing rate, carbon monoxide, air quality, smoke, and movement. The software utilizes python and swift to store, analyze, and display data.

4) Verification Results:

4.a) Introduction:

Each sensor was tested and calibrated against a gold standard and analyzed to ensure accuracy.

4.b) Methods:

Calibration curves were created for the thermistors and confirmed against a medical grade thermometer. Fast Fourier transform was performed on the microphone data to extract breathing frequency. Accelerometers were tested within a simulated flight scenario. Gas sensors were evaluated in a controlled hazardous environment.

4.c) Results:

The device displayed 98% accuracy in determining temperature, 99% accuracy in determining breathing rate, and the ability to flag flight events (e.g., turbulence, head slumping, hazardous gasses).

5) Conclusion:

5.a) Summary:

The device and corresponding application accurately depicts an improvement for diagnostic and communicative efforts for aviation emergencies, including medical and cabin events.

5.b) Revisions:

User-studies should be conducted to evaluate functionality and identify potential improvements.

5.c) Impact (Future Versions)

In the future, additional sensors, co-pilot data sharing, and flight metrics will be implemented to enable further prevention and identification of fatal emergencies.

References:

1. Taneja N. et al. HFES. 2002;46(1):155-159
2. Furman, G. et al. JMIR Form Res. 2022;6(7):e31200

Acknowledgements: The authors thank Dr. David Neivandt, Dr. Bowie, Lightspeed Aviation, DEEMI Search & Rescue, and the Orono Fire Department for all their support.

Injectable Bioorthogonal Hydrogel Accelerates Tissue Regeneration in Degenerated Intervertebral Discs [1]

Jeffrey Luo [1], Anjani Darai, MS [2], Thanapat Pongkulapa, PhD [1], Brian Conley, PhD [1], Letao Yang, PhD [1], Inbo Han, MD PhD [2], Ki-Bum Lee, PhD [1]

[1] Rutgers University, Piscataway, NJ, USA. [2] CHA University School of Medicine, Seongnam-si, Republic of Korea

Introduction: Intervertebral disc (IVD) degeneration is a major cause of back pain. Current growth factor therapies suffer from poor efficacy, while artificial discs exhibit mismatched stiffness, poor biodegradability/remodeling potential, and require invasive transplantation procedures. Injectable hydrogels are minimally invasive treatments that permit native cells to regenerate the damaged IVD and recapitulate the biological/mechanical properties of healthy tissue. Here, we conjugated bioorthogonal ligation groups tetrazine and norbornene onto gelatin (i.e., denatured mammalian collagen) to form an *in-situ* crosslinking hydrogel called BIOGEL. This hydrogel system was adapted to target IVD degeneration by (1) optimizing the biomechanical properties to mimic healthy IVD tissue and (2) loading TGFβ to induce the body to remodel the BIOGEL matrix.

Methods: Gelatin (~225g Bloom) was treated with succinic anhydride followed by EDC-NHS conjugation of 4-(1,2,4,5-tetrazin-3-yl)phenyl)methanamine hydrochloride or 5-norbornene-2-methylamine to form gelatin-tetrazine (GelTz) or gelatin-norbornene (GelNb), respectively [1]. GelTz and GelNb were resuspended in phosphate buffered saline at 5% w/v for all subsequent experiments. Viscosity and crosslinking measurements were conducted on 200 µl samples using a rheometer (Malvern, Kinexus Ultra).

In vivo experiments were performed on Sprague-Dawley rats (220-240g) in accordance with CHA Bundang Medical Center IACUC200141 [1]. In short, nucleotomies were performed to mimic IVD degeneration and administer TGFβ, BIOGEL, and TGFβ-loaded BIOGEL into the nucleus pulposus void spaces. Animals were tested for allodynia via Von Frey filaments and sacrificed at six weeks post-surgery to harvest IVD tissue for histological staining.

Results: GelTz and GelNb solutions are low viscosity across a wide range of temperature, indicating high injectability (**Fig. 1a**). Moreover, the mixed GelTz-GelNb (i.e., BIOGEL) solution undergoes gelation after 5 minutes without external stimuli, eventually reaching a plateau after 90 minutes (**Fig. 1b**). Crosslinked BIOGEL mimics the biomechanical properties of healthy IVD (**Fig. 1c**).

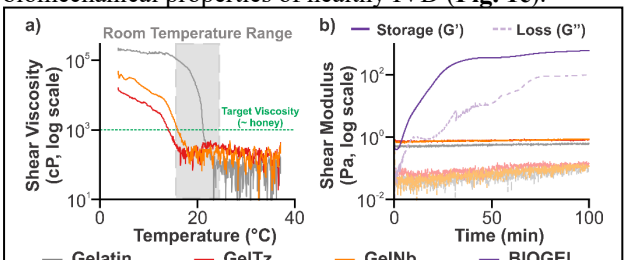

	Stiffness (kPa)		Viscoelasticity
	Elastic Modulus	Shear Modulus (0.10 rad)	Loss Factor (tan(°), 10 rad)
IVD (NP)	5.8 ± 0.5	0.18	0.43
Optimized BIOGEL	7.0 ± 0.2	0.48	0.36

*Note: **NP** = Nucleus pulposus; **AF** = Annulus fibrosus*

Figure 1. Rheometric Measurements of GelTz/GelNb/BIOGEL Solutions. (IVD reference values [2] and [3])

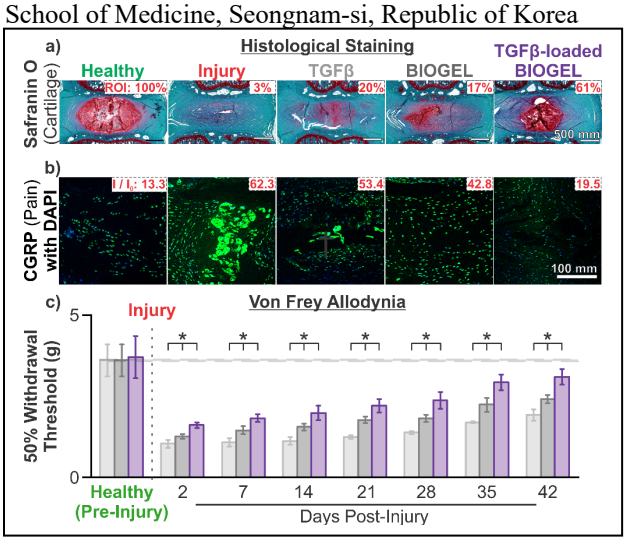

Figure 2. TGFβ-loaded BIOGEL Enhanced IVD Regeneration and Reduced Pain

To adapt the injectable hydrogel to regenerate damaged IVD, TGFβ was added to the mixed BIOGEL solutions for injection into degenerated IVD. TGFβ-loaded BIOGEL promoted the greatest restoration of secreted ECM components and tissue architecture (**Fig. 2a**). Concurrently, rats treated with TGFβ-loaded BIOGEL experienced less neuropathic pain (**Fig. 2b**) and allodynia (**Fig. 2c**) compared to control, TGFβ, and bare BIOGEL treated animals.

Conclusions: In summary, we developed an injectable hydrogel (BIOGEL) that utilizes gelatin, tetrazine, and norbornene to form a biocompatible and biodegradable tissue regeneration template. Moreover, BIOGEL can be injected into a patient for minimally invasive, *in situ* crosslinking. This technology was combined with TGFβ to target damaged IVD. Animals treated with TGFβ-loaded BIOGEL experienced greater *de novo* tissue regeneration and less pain. Since BIOGEL relies on bioorthogonal chemistry to crosslink mammalian gelatin, this technology can be extended to encapsulate a wide variety of other payloads and regenerate other damaged tissues.

References:

1. Luo JL. et al. Bioact. Mater. 2023;23:551-562.
2. Umehara S. et al. Spine. 1996;21:811-819.
3. Iatridis JC. et al. J. Orthop. Res. 1997;15:318-322.

Acknowledgements: K-B Lee acknowledges funding from the NSF (CBET-1803517), the New Jersey Commission on Spinal Cord Research (CSCR17IRG010; CSCR22ERG023), SAS-Grossman Innovation Prize, and NIH (1R01DC016612, 3R01DC016612-01S1, and 5R01DC016612-02S1). Inbo Han acknowledges funding from the Korea Health Technology Research and Development Project, Ministry for Health and Welfare Affairs (HR16C0002), and National Research Foundation of Korea (NRF-2020R1A2C4001870). Jeffrey Luo

acknowledges the NIH T32 Biotechnology Training Fellowship (GM008339).

Strain Gauge Measurement System on a Dynamized Fixator

Jeffrey Luong, Vidur Joshi, John Suarez, Ryan Kim
Stevens Institute of Technology

1) User Need:

1.a) Use Case

Hospitals regularly deal with femur and other long bone fractures that require extended fixation periods to properly heal. One way to stabilize bone is with an external fixator that connects to the fractured components of the bone, aligning them and allowing for proper healing. Despite properly fixated segments, there is the possibility of nonunions. That is the case where the bone segments do not fuse together, thereby requiring additional surgery, recovery time, and costs.

1.b) Problem Impact

Many currently available external fixators are adaptable to fixate different kinds of fractures. However, most, if not all, fixators do not provide feedback as to the status of the fracture and healing progression. Within a small sample of tibia fractures, about 20% of fractures treated with external fixation resulted in nonunions[1]. Imaging techniques are available to visualize healing, but there is no method to get real-time data on the fracture. Healing conditions where bone fragments are misaligned while fixated will only be detected when imaging is used.

1.c) Scope (Objective)

Our solution aims to prove the ability for uniaxial external fixators to use an external measurement system which can provide real-time information about the fracture site. The system can be applied to most current fixators of a similar type, employing pins into long bones.

2) Design Inputs

2.a) Constraints:

The trial fixator design must have accurate data that is available in real time. The trial fixator must also be of sufficient mechanical integrity to support bone externally, but should adjust to prevent stress shielding. Finally, the trial fixator must be able to be adjusted while in use. The fixator pin material must be biocompatible.

2.b) Requirements:

The highest priority is that the fixator must provide accurate strain gap data in real time. Currently, dynamized fixators have been adjusting without real time data, which can result in non-union. The measurement system needs to provide data up to 10% strain on the bone to maximize healing[2].

3) Solution

3.a) Design - Intended Use:

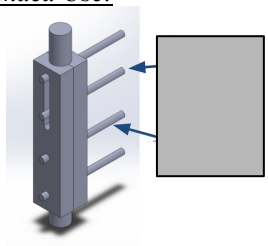

The proposed solution will place a transducer between the fracture gap pins. The model fixator is able to adjust the distance between the 2nd and 3rd pins, which results in the fracture distance change. The change in gap distance is calibrated to the transducer output prior to use, resulting in measurable data that can be converted to gap displacement.

4) Verification Results (anticipated)

4.a) Introduction (i = 1 … N)

i) The most important test we will perform will be the calibration of the transducer output voltage to gap displacement. As the novel addition to the fixator, it is required to go through verification to ensure the system works as intended.

ii) The strength of the fixator needs to be determined to ensure effective load sustainment.

4.b) Methods (i = 1 … N)

i) Using the transducer, the calibration curve will be obtained by performing a linear regression between displacement and voltage change. A minimum of 50 data points will be used.

ii) The fixator will be loaded under natural full body weight bearing of approximately 25%. The properties of the fixator will be observed and compared to typical bone.

4.c) Results (i = 1 … N)

i) It is expected that the calibration curve will be a linear relationship. Over the course of the test, the data points are expected to yield an $R^2 > 0.9$.

ii) The fixator is expected to display stronger physical properties than bone when fully deployed, but can be adjusted to 25% of body weight.

5) Conclusion

5.a) Summary:

The design is successful in implementing a sensor to a dynamized fixator to accurately measure the fracture gap. It is a proof of concept to see the effectiveness of accurately measuring the deflection across the fracture gap. Future work will involve patients, to test its effectiveness.

5.b) Revisions:

Revisions that are necessary in order to increase our device impact include pin design. Furthermore, we would need to verify if our fixator design can sustain acceptable fatigue resistance throughout the healing process.

5.c) Impact (Future Version):

Our solutions will allow the user the ability to adjust the fixator depending on the fracture gap data and thus promoting a more effective pathway to heal bone. This in turn will mitigate surgeries associated with stress shielding and fragment migration.

References:

1. Papaioannou N. et al. EJOST. 2001;11:(231-235)
2. Hak DJ. et al.Orthopedics. 2010;33(10):752-5.

Experimental Virtual Reality Setup for Applications in Neuroergonomics and Spatial Cognition Studies

Felix A. Maldonado[1], Adrian Curtin, PhD[1], Nick Jushchyshyn[2], Suri Rajneesh, PhD[1], Hasan Ayaz, PhD[1]
[1] School of Biomedical Engineering, Science, and Health Systems, Drexel University Philadelphia, PA, USA,
[2] Antoinette Westphal College of Media Arts & Design, Drexel University Philadelphia, PA, USA
[3] Lebow College of Business, Drexel University, Philadelphia, PA

Introduction: Virtual Reality (VR) is an image simulation for immersive presentation of 3D environments enabling more ecologically valid user-environment interaction, consistent with Neuroergonomics [1]. Through dynamic multimodal stimuli, VR provides an immersive experience that can be controlled by the user and or researcher. In recent years, improvements in form-factor, graphics processing, and ability to replicate realistic controlled environments have made VR an attractive technology in professional training, particularly in fields such as medical and military training [2]. In this study, we propose an experimental setup for VR studies incorporating 3D omnidirectional treadmill, eye-tracking technology, and physiological sensors (heart rate, electrodermal activity) and brain activity monitoring to study spatial cognition in navigation tasks. Previous research on mental workload during navigation has used VR but required joystick-based locomotion [3]. Our study will use functional near-infrared spectroscopy (fNIRS) as the primary tool to measure mental workload by capturing changes in prefrontal cortex hemodynamics [4]. The proposed setup attempts to create an immersive VR platform that can be utilized to study cognitive processes related to navigation and memory tasks.

Methods: The setup comprises of two main hardware: the VIVE Pro Eye VR (HTC Corp.) head mount display (HMD) and a Kat Walk Mini S (KAT VR) omnidirectional treadmill system. The Kat Walk treadmill system allows the user to walk or run and collects the speed and direction, which is then used to translates the avatar within the virtual environment. The VIVE Pro Eye (VIVE) HMD has a resolution of 1440x1600 pixels per eye (2880x1600 combined) and a refresh rate of 90 Hz. The VIVE has a built-in Tobii eye-tracker sampling at 120 Hz. Eye-tracker data can be accessed via HTC's SRanipal UE SDK. Eye-tracking can be used to infer affective state, cognitive load, and working memory [5]. To ensure accurate sensor readings, the Kat Walk, VR system, and eye-tracker needs to be calibrated for each subject to account for user forward direction, height, eye geometries. The VR environment is being developed using Unreal Engine 4 (UE), published by Epic Games. UE is an open-source all-purpose game engine, suitable for developing 2D or 3D games, virtual environments, or mixed media. UE was selected because it allows for the integration of 3rd-party hardware into the VR game via their C++ API. Lastly, the wearable fNIRS system with flat sensors can be included in VR experiments without interfering with the HMD. During the experiment, the subject is placed into a complex 3D environment , modelled by Drexel University's Immersive Media Lab at the Antoinette Westphal College of Media Arts and Design. Prior to the beginning of the task, the subject is presented a map with the target landmarks and specific order in which they must be reached. This task requires the subject to locate and navigate towards the designated landmarks in the virtual environment as quickly as possible. Along the way, they are asked to read a placard with information describing a major landmark within the environment. The task is repeated with modified landmark locations in each trial. Upon completion of the experiment, the participants complete a quiz to assess their recollection on this information. This task aims to modulate PFC hemodynamics by introducing a degree of mental workload related to navigation and wayfinding [1].

Expected Results: The proposed method combines the Kat Walk omnidirectional treadmill to facilitate natural movement within VR environments. Users can freely explore a 3D rendering of indoor environments during navigation tasks evaluating cognitive load via fNIRS.

Figure 1. Kat Walk Treadmill and subject with VR HMD

Conclusions: The proposed experimental setup aims to create an immersive virtual platform for the study of spatial cognition allowing researchers to investigate navigation and memory tasks. by employing state-of-the-art VR technologies. The omnidirectional treadmill allows the subject to perform natural gait and have a more immersive experience. The system is limited to local data storing for offline processing. Future work includes adding Apache Kafka data streaming to provide a medium for online data processing and assessment. Additional work includes making improvements in computational processing (reduce lag and increase frame rates) and user-interface to create a more immersive user-experience.

References:

1. Ayaz, H., & Dehais, F. (2021).In Handbook of Human Factors and Ergonomics (5th ed., pp. 816-841). Wiley.
2. Ryan L. et al. JBJS. 2020; 102(6):1-10.
3. Armougum, A. et al. J. Env. Psych. 2019; 65:101338.
4. Ayaz H. et al. Neurophotonics. 2022: 9(S2), S24001: 1-65.
5. Rahal., R. & Fiedler, S. (2019) J.Exp.S.Psych.;85:103842.

Acknowledgements: Study was supported by Drexel Solutions Institute. HA has equity in fNIR Devices LLC that licensed IP from Drexel University and manufactures optical brain imaging sensor used in the study.

Design of an Adaptive Seating System for Children with Disabilities

Connor Maloney, Caitlin Tatro, Emily Wambach, Dr. Andrea Kwaczala
Western New England University

1) Identifying User Need:

Neuromuscular diseases such as Cerebral Palsy, affect the development of postural and trunk control which limits a child's ability to perform independent activities [1]. Using a segmental assessment of trunk control (SATCo) Physical Therapists (PTs) can identify exactly how much support is needed and encourage children to develop additional control through muscular strength exercises such as sitting reach [2]. There is a need for an adaptive seating system to provide targeted support to the child's trunk when performing rehab exercises. Current adaptive seating devices on the market can provide trunk support, but none are modular to provide targeted control in exercise therapy. Current solutions lack adjustability to varying patients of sizes, cannot be used in different therapeutic exercises or at-home environments, or be transported easily between a rehab gym and for at-home care. The device must effectively utilize SATCo straps to align the pelvis and hips, as well as provide adaptable lateral supports that can adjust up and down, and cranial supports for children who lack head control. A universally adaptive seating system for physical therapists needs to be easily transported to be used in both clinical settings and at-home visits.

2) Design Inputs:

The device must be able to accommodate children varying in age between the ages of 3 and 8 years old, and also maintain an appropriate level of comfort for the children for a period of 1 to 2 hours. The support for the patient will stem from a series of straps on the lower half of the body, which will adhere to SATCo standards, as well as padded seating and lateral supports which will help to stabilize the patient in the seat, along with a headrest, which will provide cranial support. The device must incorporate SATCo straps, as well as adjustable components regarding the lateral, posterior and cranial supports in order to fit patients between the ages of 3 and 8. Modularity must also translate to portability in order to allow the physical therapist to use the device in multiple settings. The material used for the device must be easily sanitized for the convenience of the physical therapist. The device must be safe and stable, as well as physically appealing to the patient.

3) Solution:

The adaptive seating system for exercise is designed to allow physical therapists to adjust various components based on child's size and support requirements of their patient. Adjustability allows for increased seat depth, breadth of the child, and girth, to accommodate children as small of 18 months up to 8 year olds. Adaptive mechanisms allow lateral support, head control and pelvic control that can be adjusted for each individual patient. The exercise seating system is novel in its design with several important features:

1. Seat base has a tilt connection to allow a 30-45 degree backwards tilt and accommodates SATCo strapping mechanism at the pelvis
2. The base mounts a seat back sliding mechanism that allows the back support to adjust forward and backwards
3. A seat back peg board design optimizes the location of the lateral supports to provide custom fit orthotics
4. The peg board interacts with a bracket system complete with a quick release pin that is universal to all detached components
5. A head rest can be added when needed using the same quick release pin mechanism

The chair can be used as a simple seat base, providing SATCo straps for the lowest need (SATCo level 5) up to a high-need patient with full trunk and head support (SATCo Level 1).

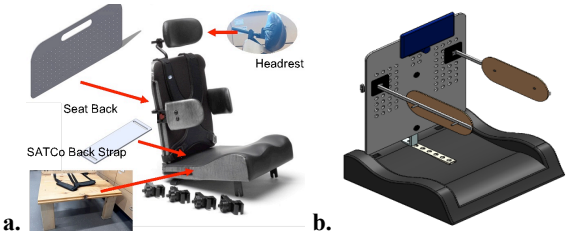

Figure 1: *Adaptive Seating System.* ***A****. Original prototype,* ***B.*** *Full assembly of a SolidWorks model of the adaptive seating system for exercise.*

4) Verification Results:

For this device to be successful SATCo strapping and lateral orthotics are required that can adapt to SATCo levels were required in making this device. To assess the verification of design specifications, modularity, weight requirements and adjustability of componentry to accommodate 95% of patient population were assessed on the final prototype. To assess user needs were met, validation studies included timing tests to determine how long it took to assemble the seat, and an IRB approved study to measure application in a single-subject design on an able-bodied child (age 4). The device performance was measured against the current seating system built by the previous research team. Data were compared using a Student's t-test, where significance level, α, was set to 0.05. The first iteration prototype was tested and met several design requirements, including incorporation of SATCo straps, as well as accommodation of children of the patient population. Improvements to the lateral orthotics, adaptability of placement, and a way to secure the laterals using quick connectors are still ongoing.

5) Conclusion:

Verification testing has revealed a successful implementation of the seating system. Continued testing is needed to verify specs and validate user requirements. Stronger lateral supports that can change to appropriate SATCo level is required. This device has the potential to change how children with disabilities can engage during exercise therapy by providing targeted trunk control that is adjusted based on growth and development. Children can improve strength and work to reduce their SATCo needs. A portable, modular device allows PTs to optimize their patient experience and help them reach new potential by providing an innovative therapeutic seating system for exercise.

References:

1. CDC, What is Cerebral Palsy? 2022.
2. Butler PB, Segmental Assess of Trunk Control, 2010.

Design of a High Voltage, Bipolar Pulse Generator for Reversible Electroporation Applications

Yuvaraj Manchukan, George McConnell.
Department of Biomedical Engineering, Stevens Institute of Technology, Hoboken, NJ

Introduction: High voltage, reversible electroporation is a technique that uses brief high voltage electrical pulses to create temporary openings in the cell membrane, which allow molecules such as drugs and DNA into the cell. We designed a high voltage, bipolar pulse generator for reversible electroporation application using an inexpensive, commercially available low voltage, low power DC power supply as a source. The majority of prior studies employed Marx generator and H-bridge based designs for such kind of bipolar high voltage generators [1,2]. Marx generator based designs provide high voltage output depending on the number of switching stages [2]. However, the number of components or switches required for higher voltage boosting is increased along with the cost. Here, we propose a combination of boost converter and Marx generator based circuit topologies, which reduces the number of stages in the Marx generator while providing higher voltage boost and higher controllability. Simulation results show approximately 7X voltage boost compared to Marx generator *per se* can be achieved with two switching stages.

Methods: The circuit was simulated using LTSpice. Two identical monopolar generators (Generator 1, Generator 2) were made, and a load was connected in between the output of the generators (Figure 1). The source of the generator is taken to be a 140W/28V (USB PD 3.1 standard) DC power supply. When the switch S1 is closed, the magnetic fields around the inductors (L1, L2) store energy. When the switch S1 is opened, stored energy is released to the next stage. The input voltage for the switching stage 1 is the summation of the source voltage and the voltage across the inductor ($V_S + V_L$). The voltage across the inductor can be controlled by the duty cycle of switch S1. In switching stages, switches S3 and S5 connect the capacitors (C1, C2, C3, C4) in parallel with the source and charge them to the voltage ($V_S + V_L$), and switches S2 and S4 connect capacitors in series with the load which increases the voltage across the load ($2(V_S + V_L)$). Both generators were controlled such that the output across the load produced bipolar pulses. The output voltage, frequency, pulse interval and polarity are controlled by externally generated switching pulses produced by an Arduino.

Results: The proposed circuit was designed with two switching stages. MOSFETs are used as switches. Inductors L1=50 µH and L2=50 µH and capacitors C1, C2, C3, C4 were all equal to 56 nF. Duty cycle for switch S1 = 0.27. The load was set as a 100 Ω, resistive load. An output bipolar pulse (amplitude = ±200V; pulse width = 6µs) was generated (Figure 2). Approximately 7X voltage boost was achieved vs. a traditional Marx generator circuit using 4 stages of switches (2 stages on each side). The duty cycle of S1 can be increased for higher voltage and S2, S3, S4, S5 can be controlled for various pulse width, pulse interval and frequency of pulse. The proposed system is scalable by increasing the number of switching stages to produce higher voltage output pulses.

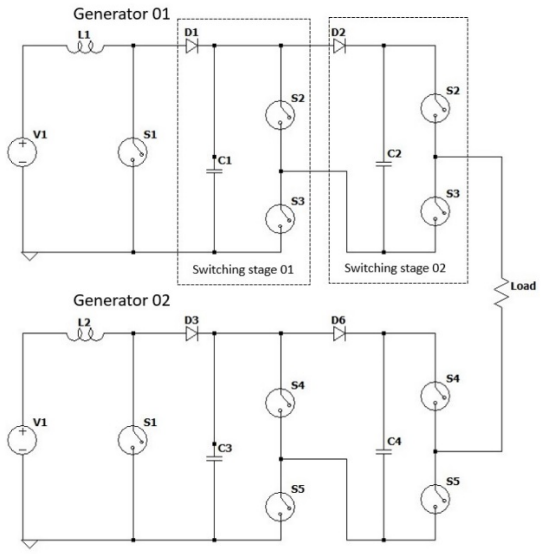

Figure 1: Proposed circuit design

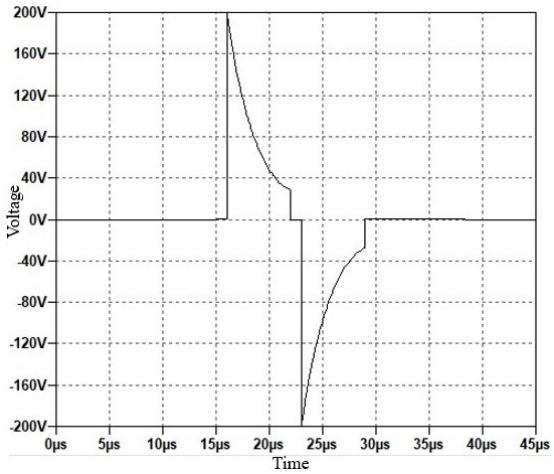

Figure 2. Generated pulse measured across the load resistor.

Conclusions: The results support the feasibility of a circuit design capable of delivering bipolar voltage pulses (amplitude=±200 V; pulse width=6µs) using a standard 140W/28V DC power supply. Future work will focus on building a working prototype of the circuit and *in vivo* characterization of the effects of stimulation parameters on reversible electroporation of fluorescent dyes.

References:

1. M. R. Q. R. Abadi, M. H. Marzebali, V. Abolghasemi and M. H. Anisi, "High-Voltage Pulse Generators for Electroporation Applications: A Systematic Review," in IEEE Access, vol. 10, pp. 64933-64951, 2022, doi: 10.1109/ACCESS.2022.3184015.
2. L. M. Redondo, M. Zahyka and A. Kandratsyeu, "Solid-State Generation of High-Frequency Burst of Bipolar Pulses for Medical Applications," in IEEE Transactions on Plasma Science, vol. 47, no. 8, pp. 4091-4095, Aug. 2019.

Development and Characterization of MCP-ELP and α-MSH-ELP Nanoparticles for Pressure Ulcer Healing after Spinal Cord Injury

Greeshma Manjunath, MS[1*], Francois Berthiaume, PhD[1], Suneel Kumar, PhD[1]

Introduction: Pressure ulcers, a challenging complication, are seen in patients with spinal cord injury (SCI). Every year 17,700 new patients are diagnosed with SCI of which 40% report pressure ulcers. It affects patients' quality of life and causes physical, social, and physiological burdens. This demands novel techniques to treat pressure ulcers caused by SCI. In this study, we developed elastin-like polypeptide (ELP) nanoparticles incorporating MCP-1 (MCP-ELP), a chemoattractant protein-1 known to restore the macrophages resulting in better wound healing and α-MSH (α-MSH-ELP) that has shown promising results in chronic wound healing in recent studies. The fusion protein approach of ELP conjugation, proven to deliver better bioavailability, stable bioactivity, and half-life was used.

Materials and methods: Media Preparation-Nutrient agar, LB broth, and Terrific Broth (TB) media were prepared to culture transformed E.coli. 3.45g media (Difco Nutrient Agar) was mixed in 150ml distilled water to prepare the agar. 1X LB Broth (Gibco) was used. 47g of TB media (Life Technologies) was dissolved in 1L distilled water to prepare TB broth and 4ml/L glycerol was added before autoclaving at 121°C and 15psi pressure.

Development of fusion nanoparticles-Recombinant MCP-1 and α-MSH was cloned in front of elastin cassette V40C2 in the cloning vector pET25b+ using the protocol developed by members of our lab. Full length coding sequences of MCP-1 and α-MSH was used to produce the plasmids which were made by Genscript. Post-transformation, the re-transformation of bacteria was done using heat shock method. In this mechanism, 1 µL of recombinant plasmid was added to 20 µl of thawed E. coli in a 1 mL tube and kept on ice for 5 minutes. The tubes with plasmid and E. coli underwent heat shock-placed in water bath at 42°C for 2 minutes followed by cold treatment by placing it on ice for 2 minutes. This assures competent bacteria to take up the recombinant plasmid. 80 µL of SOC media (Novagen) was added to the tube containing bacterial host and plasmid and the solution was incubated at 37°C for 1 hour. Bacteria was inoculated on to agar plate and was incubated at 37 °C overnight. The following day the colonies were transferred to 25ml LB broth with 1:1000 ration of Carbenicillin and it was incubated for 16-18 hours (37 °C 220 RPM). The bacterial cultures were then transferred to TB broth media with 1:1000 ration of Carbenicillin the next day. Optical density was read using spectrophotometer at 620nm at every hour until it reached a range of 0.6 - 0.8. Then 5ml prolene and 1ml of IPTG was added to each flask and was incubated overnight (220 RPM and 37°C).

Purification of fusion nanoparticles-The bacterial culture was centrifuged at 30000g at 4°C for 10 minutes. The supernatant was discarded and pellet was dissolved in 25 mL PBS with 1:100 ratio of Halt ™ protease inhibitor cocktail (100X) and 0.5 M EDTA solution (100X) (Thermo Scientific). The suspension was sonicated twice on ice and then centrifuged at 15000 x g, 4°C for 30 minutes. The pellet was discarded and 2 mL of 10% w/v of poly(ethyleneimine) (PEI) solution (Sigma Aldrich) was added to the pellet. PEI, a positively charged polyelectrolyte results in the precipitation of any negatively charged contaminants like DNA from the cell lysate. The solution was centrifuged at 20000 x g, 4°C for 15 minutes. 0.08 grams/mL of sodium citrate was added to the supernatant and incubated at 40°C for 30-40 minutes till it turned cloudy and was then centrifuged (10000 x g) at 40ºC for 15 minutes. This is the first hot cycle or spin (H1). After centrifugation the pellet was dissolved in 4 ml of PBS buffer and centrifuged again at 15000 g at 4°C for 10 minutes. This is the first cold cycle or spin (C1). The supernatant was then used to repeat the hot and cold cycle two more times. 10µL samples were collected between each cycle to conduct SDS PAGE.

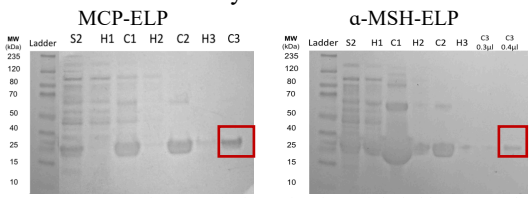

Figure 1. SDS PAGE gel: Lane 1 is the molecular weight ladder; Lane 2 has the protein in the bacterial lysate before purification(S2); Lane 3 has the protein after hot cycle-1(H1) with impurities with several bands indicate; Lane 4 depicts protein after cold cycle (C1) with lesser bands. Lane 5 depicts protein with contaminants after H2 cycle. Lane 6 shows protein after C2 with a few bands after purification. Lane 7 shows supernatant with not many bands as the contaminants have been removed after 3 cycles of ITC purification. Lane 8 represents the purified protein after final cold cycle (C3). Molecular weight of purified MCP-ELP is 33.4 kDa and α-MSH-ELP is 26.3 kDa.

Conclusions-

Successfully designed and characterized the purified nanoparticles- MCP-ELP and α-MSH-ELP. Tested preliminary viability and toxicity of fusion proteins on fibroblasts. Scratch assay and migration assay will be conducted to analyze the ability of cell migration.

References-

1. Yeboah, A., et al (2016). The development and characterization of SDF1α-elastin-like-peptide nanoparticles for wound healing. Journal of controlled release, 232, 238-247.
2. Meyer, D. E., & Chilkoti, A. (1999). Purificationof recombinant proteins by fusion with thermally responsive polypeptides. Nature biotechnology, 17(11), 1112-1115.
3. Theocharidis, G., & Veves, A. (2020). Autonomic nerve dysfunction and impaired diabetic wound healing: The role of neuropeptides. *AutonomicNeuroscience*, *223*, 102610.

Acknowledgement- This work was funded by Rutgers Busch Biomedical Grant 2021. Authors thank Dr. Rick Cohen from Department of Biomedical Engineering, Rutgers University for his technical support.

Central Venous Catheter Securement Method Using Suture Wing Plugs

Elpida Manolas, Aditi Kaveti, Julia Capobianco, Faith Fernandez
Stony Brook University

1) User Need:

1.a) Use Case

Over 5 million central venous catheters (CVC) are inserted every year by medical professionals to safely administer medical care to those in intensive care and surgical settings [1]. To preserve the safety of a CVC, it must be properly sutured to the patient's neck, posing a time limitation in procedural situations and difficulties in patient treatment.

1.b) Problem Impact

Traditional CVC suturing poses a limitation in high stress, time sensitive scenarios. Suturing on the neck can cause discomfort, as the skin undergoes necrosis [2]. This may result in the need for resuturing, increasing the chance of infection which can lengthen patient hospital stay and cause health complications [1].

1.c) Scope (Objective)

Our solution will utilize an alternative securement mechanism that secures the suture wing to the patient's neck. This will replace the need for knotting the suture string repeatedly on the suture wings, in turn reducing procedure time, limiting patient infection, and increasing patient comfort.

2) Design Inputs

2.a) Constraints:

A main constraint of this design the need to be compatible with current CVCs, as well as easily customizable to fit amongst multiple suture wing sizes. This was necessary to ensure that our design did not impede or overcomplicate the care patients were receiving from current CVCs, and that their experience remained as comfortable as possible.

2.b) Requirements:

The patient's safety is the top priority, timeliness and decrease of infection were requirements to ensure this. Much of the risk of infection comes from sutures being knotted far too tight, potentially leading to skin necrosis [2]. Our design sought to get rid of the knotting process overall, decreasing that risk of necrosis, and also decreasing the amount of time necessary to secure the CVC.

3) Solution

3.a) Design - Intended Use:

This design consists of two pieces, an applicator and a plug. The plug itself has been designed to fit into standard CVC kit suture wings, with a notch at the bottom to catch the thread, helping it push against the walls of the suture wing hole and secure the CVC. The applicator is designed to fit perfectly into the top of each plug, pushing in to create an attachment, and pushing the plug into the suture wing hole.

3.b) Build - DEMO

Our design is used in tandem with traditional suturing of the CVC. The user begins by suturing each hole of the suture wing as normal, but does not go through the knotting process. The applicator is utilized first to fit into the plug, and extract it from a custom container. This plug is then inserted into the suture wing, securing the thread.

*Currently, our group is pursuing a provisional patent for this design. Our group is unable to provide images or drawings of our design, until the patent has been filed.

4) Verification Results

4.a) Introduction (i = 1 … N)

Our subjects for surveying were all licensed clinicians, giving us accurate information regarding the process [2]. Our time trial subjects were all properly trained in suturing, and have never been introduced to our new method. Analysis included a paired t-Test, which is valid as we look for a difference in two variables from single subjects [3].

4.b) Methods (i = 1 … N)

A survey was implemented to collect preliminary data where clinicians provided the average time to traditionally secure a CVC. Randomized, controlled trials were used to collect time measurements for time needed to secure a CVC using suturing versus our method. Our solution was tested in real time, with side-by-side comparison. Each participant used both methods in paired trials. A paired t-Test was used to determine a statistically significant change in performance. This method is widely used in clinical research with a recommended 40 to 60 outcomes [4].

4.c) Results (i = 1 … N)

Our results verify that our solution meets the requirement of reducing the total time it takes to secure a CVC. The paired t-Test, revealed the two-tailed P-value to be 0.0305. By conventional criteria, this difference is considered to be statistically significant. The results are shown in Table 1.

t-Test: Paired Two Sample for Means		
	Traditional Suturing	*Our Method*
Mean (unit = s)	115.3333333	72.5
Variance	1627.066667	129.5
Observations	6	6
Pearson Correlation	0.57164482	
Hypothesized Mean Difference	0	
df	5	
t Stat	2.989463632	
P(T<=t) one-tail	0.015233065	
t Critical one-tail	2.015048373	
P(T<=t) two-tail	0.03046613	
t Critical two-tail	2.570581836	

Table 1: Results of paired t-Test

Note the sample size is relatively small. Future research would require more participants to verify our solution.

5) Conclusion

5.a) Summary:

Our product successfully achieved our objective of creating a more timely and efficient way to secure CVCs. The plug component of our product allows the suture string to be held in place without additional knotting.

5.b) Revisions:

The small size of the plug may cause complications in usage. To optimize the impact of our product, our plugs should fit snugly into our plug case. This will allow for users to easily load the applicator with the plug for insertion.

5.c) Impact (Future Version):

Further models will be developed to allow for greater force dispersion and better handling during insertion. A potential design would include attached plugs on a pushpin-like piece to fit over the suture wing.

References:

1. Deere M. et al. NIH. 2022. Central Line
2. Han Z. et al. Infect Drug Resist. 2010;3:147-63.
3. Rupps S. et al. Anesthesiology. 2012 Mar;116(3):539-73
4. Xu M. i et al. Shanghai archives. Vol. 2017.;3 184-188.

Acknowledgements: We would like to thank Dr. Yin and Dr. Schwartz for guiding our research in this topic. We would also like to thank Dr. Fernandez for his feedback in testing.

Effects of Concurrent tDCS and fMRI on Neural Connectivity During Flight Tasks

Jesse Mark[1,2], Hasan Ayaz[1,3-6], Daniel Callan[2]

1 School of Biomedical Engineering, Science and Health Systems, Drexel University, Philadelphia, PA United States 2 Neural Information Analysis Laboratory, Advanced Telecommunications Research Institute International, Kyoto, Japan 3 Department of Psychological and Brain Sciences, College of Arts and Sciences, Drexel University, Philadelphia, PA, United States 4 Drexel Solutions Institute, Drexel University, Philadelphia, PA, United States 5 Department of Family and Community Health, University of Pennsylvania, Philadelphia, PA, United States 6 Center for Injury Research and Prevention, Children's Hospital of Philadelphia, Philadelphia, PA, United States

Introduction: Neurostimulation is a rapidly developing technique that is being used to enhance performance in a variety of cognitive and motor skill domains. Transcranial direct current stimulation (tDCS) has been demonstrated to improve working memory, attention, cognitive flexibility, multitasking, and complex perceptual motor skills [1]. Moreover, the effects on neural activity have been analyzed using electroencephalogram (EEG), functional magnetic resonance imaging (fMRI), and functional near-infrared spectroscopy (fNIRS). However, very few studies have used simultaneous tDCS and fMRI to probe deep brain areas to determine the effects of stimulation during a complex realistic task on functional activity and connectivity changes. In this study, we recruited experienced pilots to perform a realistic flight simulator landing task while receiving either active stimulation or sham high definition (HD)-tDCS directed to the right dorsolateral prefrontal cortex (DLPFC), an area associated with flying. The task was presented at various difficulty levels, and feedback was provided on task performance to assist in self-evaluation.

Methods: Twenty-six trained pilots were recruited to participate in the study and randomly assigned to active stim or sham groups. Prior to the experiment, a practice session was held to familiarize participants with the task, controls, and feedback. The task itself consisted of 30-45 second trials of landing a single-engine plane on a runway, and difficulty was modulated by wind condition, the size of the runway, and a secondary auditory task. The plane was controlled by a single joystick held in the right hand. Feedback on the force of landing and speed of descent was provided after each trial. The experiment itself consisted of three runs: pre-training, training, and post-training, where tDCS and feedback were only provided during the training session. HD-tDCS was given using an MRI-safe system, and anodal stimulation at 1.5 mA for 30 minutes was delivered to the right DLPFC (AF8) with two cathode returns at Fpz and T8. The stimulation condition received 30 seconds of ramp-up and ramp-down plus constant 1.5 mA, whereas the sham condition received ramp-up and ramp-down but no further stim. The highest difficulty trials contained wind that made it more difficult to control the plane, a narrow runway difficult to land on, and a secondary auditory task requiring attention and working memory to respond correctly with a controller held in the left hand. The easiest difficulty trials contained no wind, a wider runway, and no secondary task. Combinations of these three conditions created eight levels of difficulty. Behavioral performance was analyzed using linear mixed models with the main factor of tDCS condition and experience level, with cofactors of wind, runway, and secondary task. For the fMRI data, fixed effect GLM with mixed block and event-related design was used. The contrast between the most difficult and least difficult trials was compared using t-tests to determine significantly activated functional areas. In addition, a psychophysiological interaction analysis (PPI) was used to assess connectivity between the site of stimulation and task-related brain areas.

Results: A significant main effect of tDCS (active stim vs sham), experience level, and their interaction was found (all $p<0.001$) for the landing g-force, a measure of how softly the plane landed, which is part of the feedback given. The fMRI analysis revealed a significant ROI activation of the right DLPFC ($p<0.001$), the area of stimulation, only in the active stim group given the contrast of high difficulty over low difficulty (Figure 1A). The PPI analysis additionally showed significant connectivity between this area and the left cerebellum ($p<0.001$) (Figure 1B).

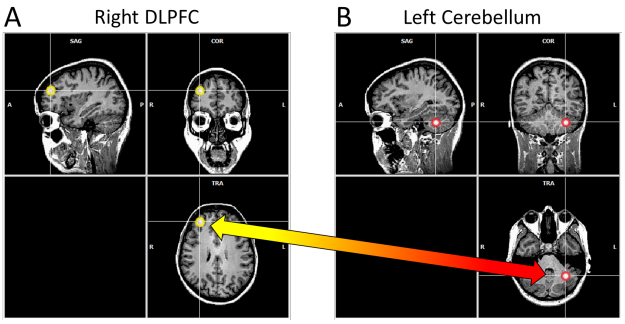

Figure 1. Neural connectivity between the right DLPFC (A) and left cerebellum (B) for Stim > Sham and high difficulty > low difficulty. Images were generated with BrainVoyager [2].

Conclusions: Active tDCS stimulation to the right DLPFC during flight simulator task training with feedback improves the landing performance, activates the site of stimulation specifically for the more difficult trials, and fosters functional connectivity with the left cerebellum, an area associated with error-based feedback learning and perceptual motor skill in flying [3]. These results suggest a method of neurostimulation and feedback training that could be applied to a wider variety of real-world tasks in the field of neuroergonomics [4].

References:

1. Chase, H.W. et al., Mol. Psychiatry. 2020;25(2) 397-407
2. Goebel, R. et al., Hum. Brain Map. 2006;27 392-401
3. Callan, D. et al., Neuroimage. 2013;72 55-68
4. Dehais, F., Karwowski, W., & Ayaz, H. Frontiers in Neuroergonomics, 2020; 1(1).

Acknowledgements: The research was supported in part by the US Institute of International Education grant number PS00295104.

A Six-Modality Cognitive Workload Assessment of Inhibitory Control Training

Jesse Mark[1], Amanda Kraft[2], Matthias Ziegler[2], Hasan Ayaz[1,3-6]

1 School of Biomedical Engineering, Science and Health Systems, Drexel University, Philadelphia, PA **2.** Advanced Technology Laboratories, Lockheed Martin, Arlington, VA **3** Department of Psychological and Brain Sciences, College of Arts and Sciences, Drexel University, Philadelphia, PA, **4.** Drexel Solutions Institute, Drexel University **5.** Department of Family and Community Health, University of Pennsylvania, **6.** Center for Injury Research and Prevention, Children's Hospital of Philadelphia.

Introduction: Cognitive workload is a measure of the mental effort required to perform a mental or physical task, and is a function of the performer's skill and the difficulty of achieving success [1]. Training is required to learn a new skill, and at each step of the process, a learner's workload may fluctuate in response to their increasing experience and the level of the task's difficulty. Although performance outcomes can be measured to give one estimate of expertise, this does not take into account the internal effort required to achieve success. Cognitive workload correlates can be obtained by primary performance, secondary performance, and subjective measures, but each has disadvantages in accuracy or disruptiveness. Instead, neuro and physiological imaging techniques can be applied noninvasively and non-intrusively to obtain objective measures of workload correlates [2]. Available physiological measures include those of the heart and pulse using electrocardiogram (ECG) and photoplethysmography (PPG), eye movement and pupil measuring using eye tracking and electrooculogram (EOG), and brain measures using electroencephalogram (EEG) and functional near-infrared spectroscopy (fNIRS). These techniques can be applied to measure the changes in workload correlates over time to determine the effectiveness of training. In this study, we focused on an inhibitory control task based on the go/no-go paradigm and developed low and high workload conditions to train over three separate sessions one week apart [3]. We present the results from six modalities and the related performance improvements over time.

Methods: Twenty-three participants were recruited to perform the inhibitory control task as part of a larger cognitive task battery. The modified go/no-go task was programmed in PsychoPy. During each trial, a series of visual stimuli were presented sequentially, and participants were told to respond to the appearance of a target cross with a keyboard button press. Stimuli lasted for 500 ms with an inter-stimulus interval of 1 s ± 250 ms. Twenty stimuli were presented per block, and two kinds of blocks, low workload and high workload, were presented three times each per session. In the low workload blocks, half of all trials changed the target cross to a flag symbol after 150 ms, which participants were told to ignore (and click as usual). In high workload, the symbol changed to a skull, which requited the inhibition of response. EEG, EOG, ECG, and PPG data were recorded with a Cognionics HD-72 dry electrode cap and extensions (500 Hz). fNIRS was acquired with fNIR Devices Model 1200 (2 Hz). Eye tracking was recorded with the Smart Eye Aurora (60 Hz). All data was manually inspected for bad channels and preprocessed in Matlab. Statistical analysis was conducted in NCSS 2019 with Linear Mixed Models run for each session and workload condition as main factors.

Results: All six modalities as well as performance were analyzed across sessions to determine the training effect on cognitive workload correlates for inhibitory control. Reaction time for correct button responses to targets changed significantly across the three sessions ($p<0.01$). A selection of significant workload correlates follows (Table 1): ECG measures of heart rate and heart rate variability changed across sessions ($p<0.01$). PPG measures of pulse width and high frequency varied with training ($p<0.05$). With eye tracking, saccade velocity, and pupil diameter were significant ($p<0.05$). EOG confirmed these measures with peak saccade velocity, duration, and amplitude ($p<0.01$). EEG was significant, widely in the delta power spectra and also in the theta-alpha/beta-alpha parietal cortex ($p<0.05$). Finally, fNIRS across the whole prefrontal cortex changed significantly with training ($p<0.01$).

Table 1. A selection of significant measures for each modality across sessions (*p<0.05, **p<0.01, ***p<0.001)

Modality	Measure	F	p
Performance	Reaction time	4.58	**
ECG	HRV	5.45	**
PPG	High frequency	7.48	*
Eye tracking	Pupil diameter	12.3	*
EOG	Saccade velocity	6.84	**
EEG	Theta AFF3	5.14	**
fNIRS	Oxy left DLPFC	28.9	***

Conclusions: We have found robust measures of the change in cognitive workload due to training across all of our chosen non-invasive neuro and physiological imaging modalities for the cognitive domain of inhibitory control. These provide complementary objective measures of workload that can be used in conjunction with behavioral performance, expert assessment, and subjective surveys to acquire a comprehensive understanding of internal and external expertise levels. Knowledge of these factors together provide a more accurate evaluation of actual skill level on a task and can be used to alter training to personalize it for each individual learner. In the future, we will extend this analysis to the full task battery targeting six separate cognitive domains as well as analyze it in the context of difficulty level.

References:

1. Parasuraman, R and Jiang, Y., *Neuroimage*. 2012; 59(1) 70-82
2. Dehais, F., Karwowski, W., & Ayaz, H. *Frontiers in Neuroergonomics*; 2020; 1(1).
3. Rodrigo, A. et al., *Neuroimage*. 2014; 85(1) 423-431.

Acknowledgements: This research was supported in part by the Air Force Research Laboratory's Human Performance Sensing BAA call 002 under contract number FA8650-16-c-6764. HA has equity in fNIR Devices LLC that licensed IP from Drexel University and manufactures the optical brain imaging sensor used in the study.

Emotional Response to Naturalistic Tasks in Children With and Without Autism Spectrum Disorder using EEG

Jesse Mark[1], Andrea T. Wieckowski[2], Kevin L. Ramirez-Chavez[1], Felix Maldonado Osorio[1], Hannah Register[2], Annie Resnikoff[2], Giacomo Vivanti[2], Diana L. Robins[2], Hasan Ayaz[1]

[1] School of Biomedical Engineering, Science and Health Systems, Drexel University, Philadelphia, PA, USA

2 A.J. Drexel Autism Institute, Drexel University, Philadelphia, PA USA

Introduction: Autism Spectrum Disorder (ASD) affects one in 44 children in the United States [1]. Children with ASD have difficulty recognizing, expressing, and regulating emotions as well as developing social interactions. This condition impedes children's development and social intelligence and may have effects much later in life [2-3]. Ensuring a healthy environment for them to grow and mature is of importance; thus, early detection and subsequent early intervention can mitigate some of these effects. Previous literature has studied emotional processing in behavioral reactions to facial expressions and play as well as comparing brain activity using EEG between ASD and typically developing (TD) children [4]. In this study, we designed an experiment meant to elicit joyful and frustration emotional states during real-world immersive playtime with a trained clinician. Children with and without ASD were monitored with mobile and wireless EEG to measure brain activity during joyful and frustration emotional states. Preliminary results suggest that a lightweight, mobile EEG may be an effective modality to explore emotional expressivity in children. The study objectives are: 1) to compare the emotional states (joy and frustration) using EEG, and 2) to determine the differences between ASD and TD children. Here we present our preliminary results from seventeen participants demonstrating our ability to elicit different emotional states from tasks.

Methods: A total of 17 children (mean age = 3.42 ± 0.94 years old) with nine children with ASD (mean age = 3.27 ± 1.05) and eight TD children (mean age = 3.58 ± 0.82) to date were included for this preliminary analysis. EEG was recorded at four locations (F3, F4, C5, C6) using the Mentalab Explore (Mentalab GmbH, Munich, Germany), a wireless, battery-operated, and miniaturized EEG system that samples at 250 Hz. Four interaction tasks designed to elicit distinct joy and frustration periods were presented in a balanced pseudorandom order and analyzed. The first Joy task involved popping **bubbles** from an electric bubble blower. The second Joy task was a **car race** using toys and small plastic ramps alongside a clinician. The first Frustration task presented a **car tower** toy that was used in guided play for three minutes. This was then taken away without explanation to elicit frustration before returning it to the child. The second Frustration task used a transparent **plastic box**, and a toy the child selects is locked inside. They are provided with a key that does not work and told to try and unlock the box for three minutes, before the correct key is given. The EEG data for each joy and frustration segments were preprocessed using artifact subspace reconstruction (ASR) to clean noisy segments, bandpass filtered between 1-50 Hz, and notch filtered at 60 Hz. Alpha, theta, beta, and alpha-theta ratio band-power asymmetry (Left-Right) were analyzed as described previously [5] to observe predominance or higher activation. Linear mixed models in NCSS (Kaysville, Utah, USA) were used to test the significance of task condition and group and their interaction.

Results: The block segments eliciting joy and frustration were isolated and processed, and these initial results suggest a potential significance of the central alpha-theta power band based on their group (ASD and TD) between joy and frustration task blocks ($p < 0.05$).

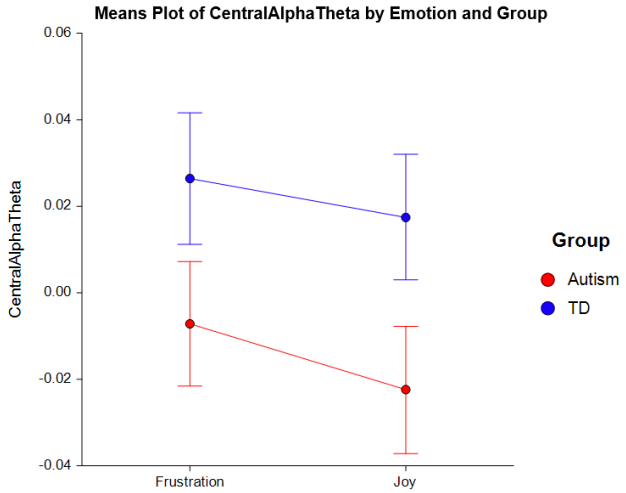

Figure 1. Joy and Frustration conditions elicited significance based on their group (ASD or TD) on the central alpha-theta power band ($p < 0.05$)

Conclusions: These preliminary results support ASD and TD differences in emotional processing and confirm the feasibility of our experimental protocol to collect electrophysiological brain activity with ultra-mobile EEG on TD and ASD children cohorts. Our current analysis does not include behavioral factors and interactions with the clinician, which will be processed for future publications. In addition to these realistic interaction tasks, we will also analyze another task of the experiment in which children observed a series of videos also designed to elicit joy and frustration, and together with the current results, will provide a more comprehensive understanding of emotions in ASD and TD children to guide potential treatment and therapy.

References:

1. Maenner MJ. et al. MMWR Surveill Summ. 2021;70(11):1-16.
2. Monteiro R. et al. Rev J Autism Dev Disord. 2017;4:255-276.
3. Velikonja, T. et al. JAMA Psych 2019;76(2):135-151.
4. Stavropoulos, K. Research in Autism Spec Disord 2017;35:62-73.
5. Sargent, A. et al. Front Hum Neurosci. 2020;14:175.

Acknowledgement: Study was funded in part by Eagles Autism Challenge.

An *In Vitro* Analysis of the Subharmonic Response of Definity, Sonazoid, and Lumason in a Closed-loop Flow System

Hailee Mayer, BS[1,2], Cara Esposito, PhD[1], Priscilla Machado, MD[1], Trang Vu, RDMS[1], Ga Won Kim, BS[1,2], Kirk Wallace, PhD[3], Flemming Forsberg, PhD[1].

1. Department of Radiology, Thomas Jefferson University, Philadelphia, PA 19107, USA
2. School of Biomedical Engineering and Health Sciences, Drexel University, Philadelphia PA 19103, USA
3. GE HealthCare, Niskayuna, NY 12309, USA.

Introduction: The subharmonic response of ultrasound contrast agents (UCAs) can be used to noninvasively estimate ambient pressures using the SHAPE technique [1]. Previous studies have shown that most commercial UCAs, such as Definity (Lantheus Medical Imaging, N Billerica, MA, USA) and Sonazoid (GE HealthCare, Oslo, Norway), have an inverse linear relationship between subharmonic signal and hydrostatic pressure [2]. However, the observed subharmonic behavior of Lumason (aka SonoVue; Bracco), has varied across studies; from inversely linear, linear, to a triphasic relationship experiencing a linear dependency at low pressures followed by a plateau and ending with an inversely linear dependency with hydrostatic pressure [2-4]. Hence, this study directly compared the subharmonic responses of Lumason, Sonazoid, and Definity in an *in vitro* flow system using a commercial ultrasound scanner.

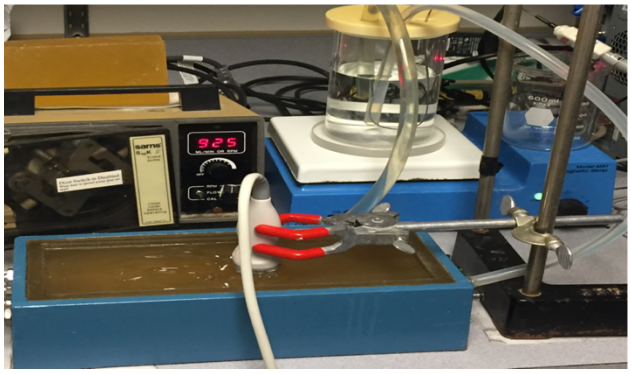

Figure 1. Closed-loop dynamic flow system for data acquisition.

Methods: The UCAs were suspended into a closed loop, dynamic pressure pump flow system (Figure 1), which produced pressures ranging from 0-40 mmHg [5]. In order to acquire the subharmonic signal, UCA was injected into 750 mL of DI water to be pumped through the Doppler Flow System (ATS Laboratories, Inc., Bridgeport, CT) using a roller pump (Sarns Inc., Ann Arbor, MI). Consistent solution was maintained via a magnetic stirrer. The volumes of each agent were predetermined as follows: .1, .2, and .3 mL for Definity, Sonazoid, and Lumason respectively. Once injected, a Logiq E10 scanner (GE HealthCare, Waukesha, WI, USA) and a C1-6 probe with 2.50/1.25 MHz transmitting/receiving frequencies was used to visualize the bubbles and extract the subharmonic signals. Calibration for each agent consisted of a five second optimization run, starting with a mechanical index (MI) of 0 and gradually increasing to 0.5. The curve of the acoustic power was then analyzed, and the inflection point was selected, which corresponded to the optimal MI [6]. Once the optimal MI was set, data was acquired over five seconds, in triplicates. The system was then cleaned out to be prepared for the next agent. Following data acquisition, the average hydrostatic pressures were correlated with subharmonic amplitude using linear regression.

Results: As demonstrated in Figure 2, Definity and Sonazoid showed an inverse linear relationship with pressure as expected (slope=-0.33 dB/mmHg, r=0.82 and slope=-0.24 dB/mmHg, r=0.91), while Lumason showed a direct linear relationship (slope=0.47 dB/mmHg, r=0.82). The subharmonic amplitude decreased by approximately 10 dBs over the pressure range for Definity and Sonazoid, while there was a 10 dB increase in the subharmonic amplitude for Lumason.

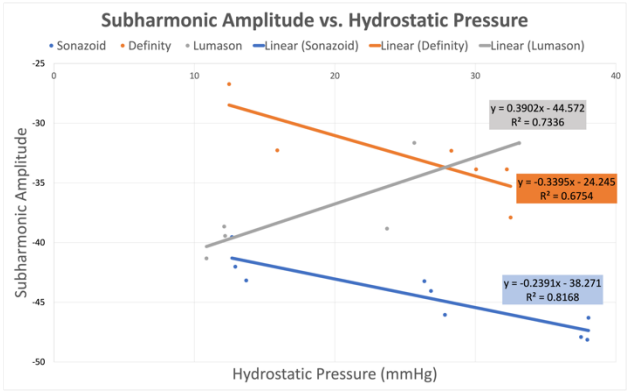

Figure 2. Linear regression results

Conclusions: Lumason's behavior, as a function of the hydrostatic pressures tested, was opposite to that of Definity and Sonazoid. Given these conflicting results, compared to the published literature, further investigations into Lumason's subharmonic response to ambient hydrostatic pressure changes are needed.

References:

1. Forsberg F. et al. J Vis Exp. 2020; 166.
2. Nio A.Q.X. et al. IEEE Trans Ultrason Ferroelectr Freq Control. 2020;67(557-567).
3. Xu G. et al. IEEE Trans Ultrason Ferroelectr Freq Control. 2021;68(3583-3591).
4. Andersen K.S. and Jensen, J.A. Ultrasonics, 2010;50(294–299).
5. Esposito, C. et al. IEEE Trans Ultrason Ferroelectr Freq Control. 2021;68(579–585).
6. Dave, J. K. et al. Ultrasonics, 2013;53(880–888).

Acknowledgements: This work was supported in part by NIH R01 DK098526 and R01 DK118964.

Quantitative Visualization Tool for the Assessment of Risky Dense Mammographic Tissue

Margaret McCarthy, B.S.,[1,2] Kendra Batchelder, M.A.,[1,2] Andre Khalil, PhD[1,2]

[1]*Department of Chemical and Biomedical Engineering, University of Maine, Orono ME, USA*

[2]*CompuMAINE Lab, University of Maine, Orono ME, USA*

Introduction: Breast cancer is the second most occurring cancer type and is ranked fifth in terms of mortality.[1] X-ray mammography is the most common methodology of breast imaging and can show radiographic signs of cancer, such as masses and calcifications. From these mammograms, radiologists can also assess breast density, which is a known cancer risk factor.[2] However, since not all dense tissue is cancer-prone, we hypothesize that dense tissue can be segregated into healthy vs. risky subtypes. We propose that risky dense tissue is associated with tissue microenvironment disorganization, which can be quantified via a computational characterization of the whole breast to provide an image-based risk assessment.[3,4]

Methods: The two-dimensional wavelet transform modulus maxima (2D WTMM) method is a strategy previously utilized on mammographic images to characterize the loss of tissue homeostasis and tissue disorganization.[3,4] A sliding window protocol is used within the 2D WTMM to analyze thousands of overlapping small subregions of size 256x256 pixels from the original mammogram. This approach starts in the top left corner and ends in the bottom right corner in a step size of 32-pixel increments. The subregions of mammographic breast tissue are categorized according to Hurst exponent (H) values and colors based upon these values: fatty ($H \leq 0.45$, blue), healthy dense ($H \geq 0.55$, red), and risky dense tissue ($0.45 < H < 0.55$, yellow).[3,4] To decrease computational time and cost, an investigation into the efficiency of the sliding window approach was conducted by considering different pixel step size increments.

Results: Increments of 32, 64, 128, and 256 pixels were compared using the percent composition of each tissue type and a statistical Wilcoxon Rank Sum test (Figure 1).

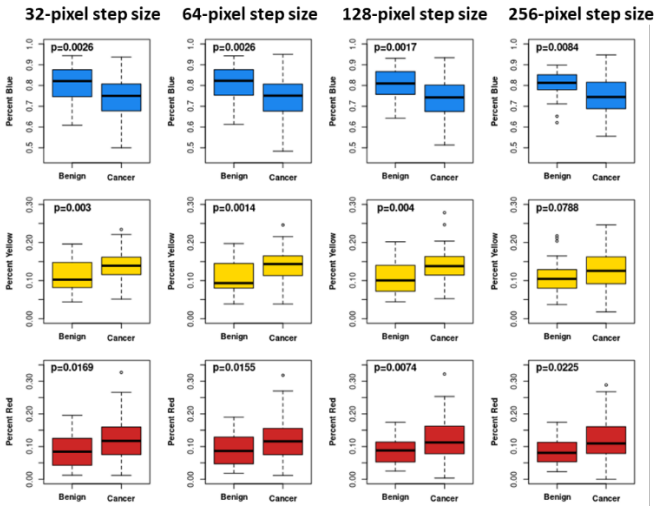

Figure 1. Comparison of percent fatty tissue (percent blue), risky dense tissue (percent yellow), and healthy dense (percent red) tissue across all step size scales (32, 64, 128, 256) to assess statistical differences between cancerous and benign tissue.

Altering the step size increment from 32 to 64 and 128 provides comparable levels of statistical significance in determining differences between cancerous and benign fatty tissue, risky dense tissue, and healthy dense tissue. To accompany the statistical analysis of tissue composition, multi-layered heatmaps can be overlaid onto the raw mammogram as a diagnostic tool (Figure 2).

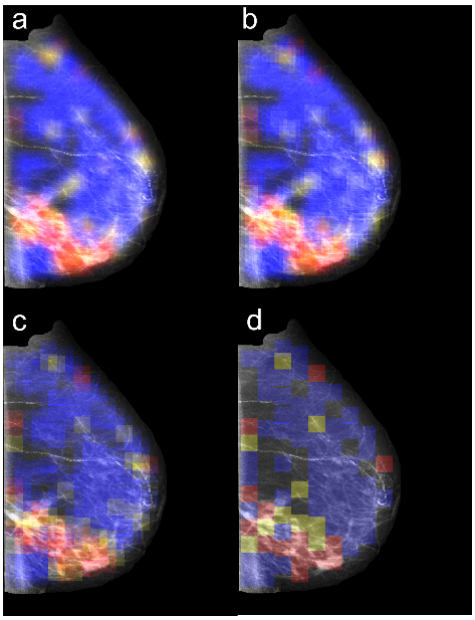

Figure 2. Multi-layered heatmap of proposed tissue types overlaid with a mammogram at a) 32, b) 64, c) 128, and d) 256 increment step sizes.

Conclusions: Utilizing a different step size increment provides the same levels of statistical significance in categorizing mammograms with cancerous versus benign lesions (Figure 1). This may lead to a 1600% acceleration in the computational analysis of proposed tissue types within mammographic images when compared to previously developed methodologies.[3,4] As a result of the 2D WTMM method, multi-layered color representations of mammographic tissue types can be created as an early diagnostic tool for radiologists (Figure 2a-d). Further optimization of these multi-layered visuals will provide a more accurate, useful tool that allows medical professionals to identify breast tissue composition may put them at a higher risk of developing invasive cancer.

References:

1. Siegel, R. L. et al. CA Cancer J Clin. 2015;65, 5-29
2. Boyd N. et al. Lancet Oncol. 2005; 6:798-808
3. Marin, Z. et al. Med Phys. 2017; 44, 1324-1336
4. Gerasimova-Chechkina, E., 2021;12:660883

Acknowledgments: Research within this abstract was supported by the National Cancer Institute of the National Institutes of Health under award number R15CA246335.

Noninvasive Transcutaneous Electrical Stimulation Device

Emily McCormick, Kamran Rajput, Jennifer Yim, Linda Vataksi, Dr. Jennifer Kang-Mieler, Dr. Spencer Brinker
Stevens Institute of Technology Biomedical Engineering Department

1) User Need:

Trigeminal Neuralgia (TGN) is a rare neurological disorder characterized by severe facial pain triggered by facial movements such as brushing teeth, eating, or talking. These excruciating paroxysms of pain can last between a few seconds to a couple minutes and tend to recur frequently throughout the day and night. Approximately 150.000 people are diagnosed with trigeminal neuralgia every year and it is most common in women over the age of 50 [1]. Currently, there is no ideal treatment for neuropathic pain management related to TGN. The "gold standard," surgery can lead to severe risks and pharmaceutical treatments, such as anticonvulsant drugs, can have long term adverse effects [2].

2) Design Inputs

The TGNAid device prioritizes portability and ease of use for the patient which inspired the wearable headset design. The wearable aspect will allow trigeminal neuralgia patients to rapidly administer their own electrostimulation and heat for an immediate and customized form of pain relief. The device also utilizes dry electrodes to eliminate the additional steps of applying a gel electrode and to quicken the process from the onset of pain to the application of treatment. Additionally, the final product will be an untethered device which will require a housing unit that can both safely encase the circuitry while also maintaining the device's low-profile and non-obtrusive nature. Our highest priority requirements are to stimulate the peripheral trigeminal nerves up to a depth between 1 to 2cm with a current no higher than 5 mA for up to 45 minutes of treatment with an adjustable square pulse wave. The heating element must also heat up to around 105 degrees Fahrenheit and all these parameters must have the capability for user input.

3) Solution

The TGNAid is designed to be used as a standalone unit that is configured through a mobile application. The earpiece will target the mandibular and maxillary branches of the trigeminal nerve, as they can be accessed from the temple, which means that setup of our device is simple and quick, making it ideal for daily use during the onset of pain. The user will be able to preset their preferred parameters on the app, so the setup time is further decreased. Physical knobs on the earpiece will be used to fine tune the parameters to provide optimal pain relief.

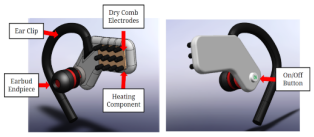

Figure 1: TGNAid Earpiece SolidWorks Prototype

4) Verification Results

To validate the safety and efficacy of the device, the electrical stimulation device's functional properties were tested using agarose gel and a pulse wave electrical signal. A safe exposure of current to the human body through electrical stimulation is between 0-3mA. Any current level above 5mA would create painful shocks that could lead to severe muscular contractions.

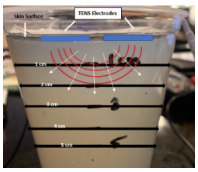

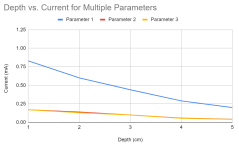

Figure 2: Electric Field Simulation **Figure 3:** Depth vs. Current for all Parameter Sets

Electrodes were placed on the surface of the gel and measurements were recorded to confirm the extent to which the signal would penetrate the skin to the required depth, while maintaining a safe and effective signal amplitude. The testing results show that maximum settings of the TENS device are substantially lower than the safety threshold of current level for a safe distance.

5) Conclusion

The TGNAid Earpiece is an easy-to-use, portable, and self-administrable medical device that safely and effectively provides immediate pain relief using TENS and a heating component concurrently. Further research includes improving aspects and features of the design that have variability in its parameters so the standard of use and application can be updated with current research. Trigeminal Neuralgia is a pathology that results in excruciating facial pain that can either come as sustained dull pain, or acute stabbing pain, which affects individuals' everyday life. As such, the TGNAid earpiece aims to provide a safer alternative to pharmaceutical drugs and surgical procedures which offers patients more flexibility and bodily autonomy.

References:

1. Obermann M. Therapeutic Advances in Neurological Disorders. 2010; 3(2); 107115
2. Diana C et al. Journal of oral and maxillofacial surgery. 2021; 79(11), 2227–2239.

Commented [1]: Retain the subsection titles 1a 1b 1c etc

Commented [2]: Same figure-related comment as before, you can get rid of the 0 and 6 on the x axis of your figure to save some horizontal space and then resize the figure accordingly.

Development, adaptation, and persistent, stimulus-independent neural activity in a sensorimotor circuit in *Drosophila melanogaster.*

Brennan W. McFarland[1], HyoJong Jang[1], Yerbol Z. Kurmangaliyev[2], Aljoscha Nern[3], Michael J. Parisi[4], Kristen C. Davis[4], Timothy J. Mosca[4], Tanja A. Godenschwege[5], Catherine R. von Reyn[1,6]

[1]School of Biomedical Engineering, Science and Health Systems, Drexel University, Philadelphia, PA, [2]Department of Biological Chemistry, Howard Hughes Medical Institute, David Geffen School of Medicine, University of California, Los Angeles, Los Angeles, CA, [3]Janelia Research Campus, HHMI, Ashburn, VA, [4]Department of Neuroscience, Thomas Jefferson University, Philadelphia, PA, [5]Department of Biological Sciences, Florida Atlantic University, Boca Raton, FL, [6]Department of Neurobiology and Anatomy, Drexel University College of Medicine, Philadelphia, PA

Introduction: Central to all animals is the ability to interpret relevant external stimuli and react appropriately. For animals to be able to recognize and react appropriately to stimuli, neurons must first develop and wire with appropriate partners to build functioning neural circuits. The visual system has served as a model system to investigate neuronal development and target specificity, but rarely has the relationship between connectivity and downstream neuronal output been investigated in the same system. A major barrier to studying neural circuit development and investigating how neurons integrate inputs from many pre-synaptic partners is the lack of systems amenable to genetic and physical accessibility over development necessary for impactful, direct experimentation. Here, we take advantage of the genetically tractable animal *Drosophila melanogaster* and explore the development of a functionally well-characterized sensorimotor circuit, the convergence of visual projection neurons (VPNs) onto the dendrites of a large descending neuron called the giant fiber (GF).

Methods: All flies were reared at 25°C and 60% humidity on a 12-hour light/dark cycle. For developmental experiments, flies were dissected at the appropriate developmental time (hours after pupa formation, hAPF), and immunohistochemistry was performed following an established protocol [1]. Antibodies are listed in the figure legends. All images were taken on an Olympus Fluoview 1000 confocal to achieve a voxel size of .103µm x .103µm x .45µm, and all imaging parameters were kept consistent unless otherwise stated. No image processing was performed prior to image analysis. Image analysis was performed using custom Matlab scripts. For our scRNA-seq data analysis, we used a published dataset [2], and performed a non-parametric Kruskal-Wallis test by ranks for statistical analysis. For electrophysiology recordings in adult flies, we used a recently published setup and protocol [3]. For *ex-vivo* electrophysiology recordings, we used the same reagents for recording used in adult recordings.

Results: We found two partner VPNs, encoding different visual features that target the same GF dendrite, occupy distinct territories on the GF dendrite, in part, through sequential axon arrival during development. We found that during the initial partner matching stage, pre- and post-synaptic proteins are already present and opposed to one another. Physical occupancy is important to maintain territories, as we found the ablation of one VPN results in expanded dendritic territory occupied by the surviving partner VPN, and that this compensation enables the GF to remain responsive to ethologically relevant visual stimuli. Lastly, we developed a novel *ex-vivo* electrophysiology preparation and performed the first electrophysiology recording from a pupal CNS neuron. Using this preparation, we recorded persistent, stimulus independent neural activity in the GF in pupal stages, suggesting neural activity may be important for appropriate GF development.

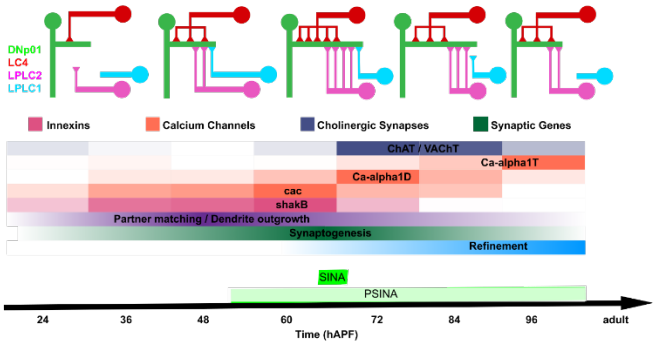

Figure 1. Schematic of GF development with respect to LC4, LPLC2, and LPLC1. The five representative drawings represent connectivity at 24hAPF, 48hAPF, 72hAPF, 96hAPF, and adulthood. Relative gene expression levels are colored from light (lower levels) to dark (higher levels). **Conclusions:** Our data highlight temporal mechanisms for visual feature convergence and promote the GF circuit, and the *Drosophila* optic glomeruli where VPN to GF connectivity resides, as an ideal developmental model for investigating complex wiring programs and plasticity in visual feature convergence. We also find that the GF adapts in response to developmental perturbations, suggesting that neuron physiology is largely preserved and even enhanced in some aspects, suggesting strong adaptive mechanisms to preserve function.

References:

[1] McFarland, B. W., et al. bioRxiv. (p. 2022.08.20.504653).

[2] Kurmangaliyev, Y.Z., et al. Neuron, 2020. **108**(6): p. 1045-1057 e6.

[3] Jang, H., et al. (2022). bioRxiv. (p. 2022.07.15.500271).

Acknowledgements: We would like to thank the Cell Imaging Center at Drexel University for providing the facilities to perform confocal microscopy. Funding was provided by the National Science Foundation Grant No. IOS-1921065 (CRvR) and the National Institutes of Health NINDS R01NS118562 (CRvR).

Physiological Storage Solution Effects on Passive Muscle Mechanical Properties

Timothy McGinley[1] and Benjamin I Binder-Markey[1,2]
[1]School of Biomedical Engineering, Science and Health Systems &
[2]Department of Physical Therapy & Rehabilitation Sciences College of Nursing & Health Professions

Introduction:
Understanding muscle structure and function relationships are essential to determining muscle performance and recovery following injury or disease. Muscle active force generating mechanics have been widely characterized across muscle tissue's scales from the whole muscle down to the single muscle fiber, scaling linearly across scales [1]. However passive muscle mechanics (the muscle's elastic properties) do not scale linearly across scales, and it is unknown the sources of passive mechanics across scales. One problem contributing to this dearth of knowledge is multiscale mechanical testing cannot be completed in a single day due to the time required to test the samples. Thus, samples are often stored in a physiological storage solution to preserve the sample. This storage solution preserves the active mechanics; however, it is unknown how the storage solution affects the passive mechanics of the muscle. Thus, the purpose of this study is to begin to understand how physiological storage solution affects whole muscle passive mechanical properties.

Methods:
Passive mechanical characteristics of fresh and stored samples were collected across four muscles, differing in structure and function, from 12 to 16-week C57BL6 mice. Muscles were lateral gastrocnemius (LG), rectus femoris (RF), semimembranosus (SM) and tibialis anterior (TA) (n_{fresh}=7-9; n_{stored}=6-7). Fresh muscles were dissected from origin to insertion, placed in a physiological bath, and mechanically tested. Stored muscle samples were dissected from origin to insertion, placed in a physiological storage solution that contained 170mM potassium propionate, 5mM EGTA, 2.5mM Mg, 2.5mM ATP, 10mM imidazole, and 50% (v/v) glycerol at pH 7.0[2]. Samples were stored at 4ºC for 48hours and then placed in -20ºC freezer for 2-weeks. For mechanical testing, the samples were fastened to a 5 N force transducer and muscle slack length determined. Then the muscle was lengthened in ~5% fiber strain increments from 0%-50% being held for 3-minutes at each strain. Force and displacement at the end of each 3-minute hold were recorded. Following testing the samples were weighed. Muscle passive forces were normalized to physiological cross-sectional area (PCSA), and muscle strain was converted to fiber strain using fiber length-ratio [2]. The normalized passive stress-strain data were fit to an exponential curve, from which the stiffness was compared across muscles and storage solution.

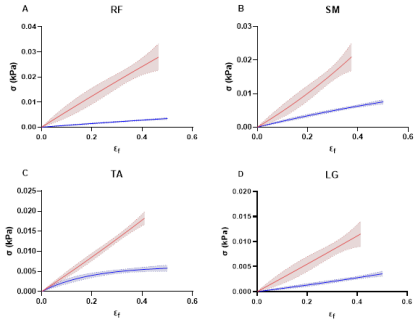

Figure 1: Normalized Stress-Strain Curve for fresh (red) and stored (blue) of the A) RF, B) SM, C) TA, & D) LG. Data shown as averages±SD. n_{fresh}=7-9; n_{stored}=6-7

Results:
Muscles stored in storage solution demonstrated significant swelling (Table 1) swelling an average of XXX% across all muscle. Normalized stress-strain curves shown in Figure 1, with moderate to good fits, and stiffness coefficients (Table 1) demonstrate sustainable decreases in stiffness following storage.

Conclusions:
Unlike active muscle mechanics, storage solution does not preserve the passive mechanics of muscle at the whole muscle scale. Following storage muscles demonstrate swelling and reduce muscle stiffness indicating potential damage to the extracellular matrix. Future studies will explore the mechanics of the fascicle and single fiber scale.

References:
1. Winters, T.M et al. J. Biomech. 2011. **(44) 109–115**. 2. Eastwood A.B. et. al., Tissue & Cell 1979. **11 (3) 553-566** 3. Ward et al., Front. Phys. 2020. **11 (211)** 4. Burkholder et al. J. Morph, 1994. **(221) 177-190** 5. Lieber, R.L., Blevins, F.T., J. Morph. 1989. **(199) 93–101**. 6. Lieber, R.L., Fridén, Jan, J. Ap. Phys.. 1993. **(74-2) 520-526.**

Table 1: Physiological Properties of Fresh and Stored Muscle

	Mass (mg)		% Swelling	Stiffness, b		r^2±SEM	
	Fresh	Stored	M_{STORED}/M_{FRESH} * 100%	Fresh	Stored	Fresh	Stored
RF	69.53 ± 9.07	116.07 ± 6.63	166.93	-0.23	-0.31	0.47±0.01	0.73±0.00
SM	92.91 ± 21.87	131.16 ± 13.16	141.15	1.13	-0.82	0.50±0.01	0.78±0.00
TA	50.66 ± 12.95	57.57 ± 6.30	113.64	0.35	-5.12	0.79±0.00	0.53±0.00
LG	77.59 ± 18.46	106.4 ± 9.81	137.15	0.12	0.55	0.35±0.01	0.65±0.00

Deleted: mechanics,
Deleted: RF
Formatted: Font: 6.5 pt
Deleted: 1)demonstrate
Deleted: Unlike with
Deleted: mechanic
Deleted: at
Deleted: ¶
Formatted: Font: 1 pt
Formatted: Font: (Default) +Body (Calibri), 1 pt, Font color: Auto
Deleted: ¶
Commented [BB1]: Only do 2 sig figs
Formatted: Font: 10 pt
Formatted: Space After: 0 pt, Line spacing: single

Duraspine Pedicle Hole Integrity Monitor

Sydney Mellage, Madison Schmidt, Danielle Cornetta, Jenna Hassan, Camryn Rogers
Stevens Institute of Technology, Hoboken, NJ

1) User Need:

1.a) Use Case

There is a need to verify wall integrity during placement of posterior pedicle screws during spinal fusion surgery. More specifically, real-time tactile and quantitative feedback verifying the traditional pedicle wall integrity is warranted. The proposed solution will mitigate screw breaching complications and thus mitigate the need for revision surgery associated with this issue. The device and process of use will be substantially equivalent to current pedicle probes and thus entail a shallow learning curve for integration into current surgical procedures.

1.b) Problem Impact

A total of 130,000 cervical spinal fusion surgeries are performed every year. The average cost of $50k per surgery creating a $6.5 billion market. Approximately 1 in 300 of these primary surgeries will require revision due to malpositioning of screws or breaching of the pedicle wall. This specific complication results in approximately an additional $25 million in annual costs. The solution will reflect the need to accurately provide real time feedback on pedicle hole integrity and screw trajectory while also limiting patient morbidities associated with a revision surgery. Current solutions are cost and time prohibitive.

1.c) Scope (Objective)

In current practices, there are limitations associated with the pedicle probes utilized for cervical spinal fusions. The current standards of care entail robotic equipment (increasing surgical costs and time), fluoroscopy, or are performed completely blind. Regardless of method, no tactile/mechanical feedback is provided. The Duraspine pedicle probe plans to address these limitations with an innovative and unique design.

2) Design Inputs

2.a) Constraints:

Fabrication of the device will include biocompatible materials that have strong biomechanical properties. While in use, little or no interference of the feedback system with external electrical signals in the surgical suite must be demonstrated. The mechanical response of the device is to be shown, reliable and repeatable.

2.b) Requirements:

The pedicle probe design is targeted for use in the cervical spine from C4 to C6. The team anticipates a diameter range for the pedicle screw is 3-4.5mm, a pedicle depth of 35mm and a mean cross-sectional diameter of 1.5mm.

3) Solution

3.a) Design - Intended Use:

The design includes a real-time feedback system to determine the pedicle hole integrity to ensure mechanically viable bone is available for pedicle screw placement prior to screw insertion. The design includes a
blunt tip to allow for reduced damage to the surrounding area as well as a curvature in the body to allow for probe bending to measure bone viability. This probe will be used along with our circuitry components.

3.b) Build - DEMO

The team has created a feedback system that includes differential instrumentation amplifiers, supporting electrical properties of the pedicle wall.

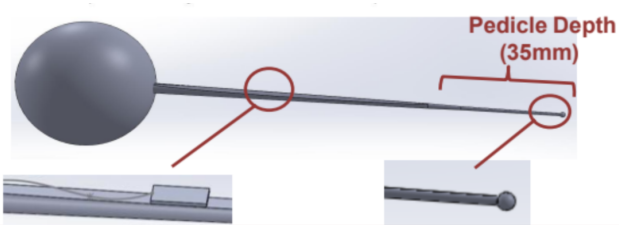

Figure 1: Duraspine's Cervical Pedicle Probe

4) Verification Results [Anticipated]

4.a) Introduction (i = 1 … N)

Our tests are designed to verify proof of concept and to provide validation/accuracy of output as related to the mechanical environment of the pedicle wall.

4.b) Methods (i = 1 … N)

Calibration of the sensor will be conducted using various bone density models. Solidworks FEA analysis will determine the ultimate failure point of the probe design. Bone blocks will be utilized to test linear response between bending and applied force.

4.c) Results (i = 1 … N)

Expected results from bone block testing will determine accuracy of transducer design to indicate a safe and viable range of data for response of bending and applied force to ensure integrity of the pedicle hole.

5) Conclusion

5.a) Summary:

The design will successfully output real-time force readings during spinal fusion surgery to evaluate the integrity of the pedicle prior to screw placement. The results from our tests will demonstrate a linear response between probe deflection and applied force that can be applied to determine bone integrity.

5.b) Revisions:

The team plans on using data collected from various tests to assess any changes that can be made to the probe design for optimal performance. This could include revisions to the dimensions, sensors, or configuration of the design.

5.c) Impact (Future Version):

This pedicle probe is unique and has the potential to alter the way orthopedic surgeons monitor pedicle screw insertion. Duraspine will appeal to hospitals and orthopedic surgeons by reducing surgical times, supplying numerical real-time feedback, reducing the risks associated with exposure to radiation, and ensuring an increased rate of spinal fusion success and decreased need for corrective surgeries or future complications.

References:

1. Martin BI. et al. 2019 Mar 1;44(5):369-376
2. El-Desouky A. et al. 2021 Apr 1;205:106623

Accurate & Simple Goniometer to measure 3D movement of the knee joint post-operatively

Jake Millburn, Steven Zederbaum, Carl Colditz, Tianyuanye Wang
Stevens Institute of Technology

User Need:

Orthopedic surgeons and physical therapists utilize rotational measurements of the knee to evaluate quality of care and current status of rehabilitation. Specifically, they collect flexion-extension, varus-valgus, and internal-external rotation. Current solutions to collect rotations, such as the KT-1000 and the universal goniometer, are either prohibitively expensive or imprecise. As a result, traditional goniometry is not regularly used in orthopedic postoperative care. Mechanical loosening is the second-leading cause of knee replacement revision surgery, but it is unclear whether imperfections in surgical technique are to blame due to the difficulties in attaining consistent and high-resolution measurements[1]. The objective of this project is to provide orthopedic surgeons and physical therapists with a reliable tool with which to collect and compare 3D rotations of the knee, following knee constructive surgery.

Design Inputs

This device must be aligned with the tibia and femur in order to work correctly. The device must record full range of motion through active and passive measurement sets, as well, for a complete picture of knee function. This device is successful if a series of users can apply the device and achieve an inter-operator error of less than six degrees while providing a measuring resolution of one degree or finer for all rotations.

Solution

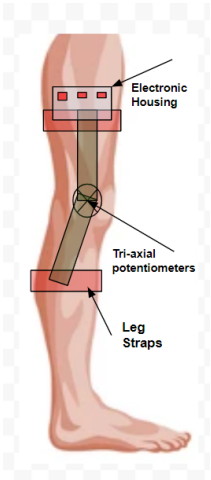

Figure 1. Intended Use

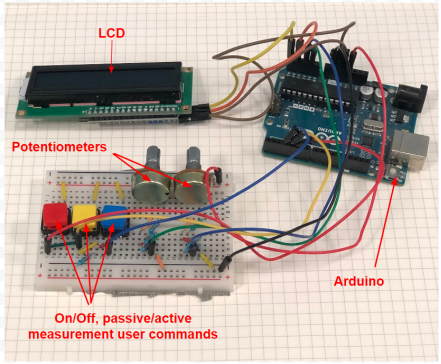

Figure 2. Circuit Demo

Figure 3. Design Workflow

Verification Results

To determine consistency in the device and ensure our results are of value, a calibration test will be conducted. The purpose of our calibration test is to determine the circuit output per increment of angle. Each potentiometer will have its own calibration test which consists of connecting the potentiometer to the circuit and placing it in a rotary calibration wheel. The potentiometer will step through 5-degree & 1-degree increments, with the output voltage measured with a multimeter and graphed accordingly.

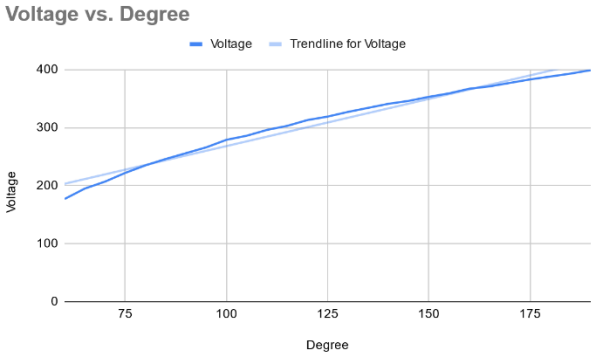

Figure 4. Calibration Test Volage vs Degree

We have two different circuit designs for different knee rotations. The average rotation shows an acceptable range of angles with a consistent displacement greater than 1 mV per degree between 0 and 100 degrees with an R^2 value of 0.975, as determined by linear regression.

Conclusion

The circuit design provides clinical viable results through the first round of testing conducted. The trends observed in the graph confirmed that the potentiometers can collect measurements in the angular range required. Improved resolution of the potentiometers may be attained by using an op-amp. Incorporating an op-amp will allow a more precise range of values to be implemented as parameters for the potentiometer output. Establishing these restraints will allow the sensitivity of the potentiometer to be adjusted to suit the needs of the goniometer. This addition will modify the linear ranges which will allow the installation angles of the potentiometers to be controlled. These revisions will ultimately allow the design to provide the user with more consistent and accurate data. The ranges that are determined through the tests outlined as well as the modifications currently in planning will fine tune the potentiometers to return higher quality data.

Development of a 3D Breast Cancer Spheroid Migration Model Targeting the Integrin α10β1 Collagen Binding Site

Jordan N. Miner[1,2,3], Zoe Vittum[1], Peter Brooks, PhD[2,4], Andre Khalil, PhD[1,2,3], Karissa Tilbury, PhD[1,2]
[1]University of Maine Chemical and Biomedical Engineering Department, [2]University of Maine Graduate School of Biomedical Science and Engineering, [3]University of Maine CompuMAINE Lab, [4]MaineHealth Institute for Research

Introduction: The growth and metastatic spread of malignant tumors is controlled by the stromal microenvironment and the extracellular matrix (ECM).[1,2] During tumor growth, matrix metalloproteinases (MMPs) secreted by various cell types remodel collagen in the ECM leading to the exposure of cryptic integrin binding sites.[1] These sites play a role in tumor cell adhesion, migration, and proliferation through their interaction with cell surface receptors such as integrins. Recently, one such binding site termed HU177 was discovered in collagen types I-V and is recognized by integrin α10β1. The HU177 murine monoclonal antibody that can target the HU177 site is unable to bind to normal intact collagen, ensuring great binding specificity to its target.[3] Preliminary phase-1 clinical trials demonstrated the possibility of anti-tumor activity while targeting this site.[4] Therefore, a 3D spheroid model is currently being developed using MDA-MB-231 triple-negative breast cancer cells to explore the HU177 site in a system that closely mimics the human body through its cell-cell and cell-ECM contacts.[5] The goal of this project is to determine how D93, the humanized version of HU177, impacts cellular migration of cells in this 3D model.

Methods: Spheroids were generated at an initial seeding density of 4,000 MDA-MB-231 cells per well using the centrifugation method. Spheroids were embedded in a 2 mg/mL collagen type 1 hydrogel in a 96 well plate (1 spheroid/well) one week after generation using the sandwich method. In addition to rat tail collagen, the hydrogel contained complete cell media (DMEM/F12, 1X pen strep, 10% FBS) 59 mM HEPES (pH 7.3), and D93 (20 µg/mL) in PBS for the D93 experimental group and only PBS for the control group (n=5 for each group). The gel was allowed to fully polymerize for 1 hour in the incubator (37°C) before the initial imaging was completed and kept in the incubator between imaging sessions. Using a Cytation 5 Multimode Reader, a 3D stack of widefield fluorescent images was captured every 24 hours for a total duration of 72 hours. A single image projection was produced using the focus stacking method for each time point. A custom ImageJ macro was created to quantify the migration distance. Each migrating cell was individually analyzed (StarDist plugin used for cell segmentation) using the distance between the boundary of the spheroid to the cell's centroid assuming a radially straight migratory pattern. Samples were fixed at the end of 72 hours with 4% paraformaldehyde and fluorescently labeled with DAPI and for D93 with Alexa Fluor 488 before imaging with the Cytation 5 using the DAPI and GFP filter cubes, respectively.

Results: Prior to embedding, spheroid generation was uniform and consistent in terms of area and diameter. During experimentation, the spheroid area remained consistent between the two groups for each time point. Furthermore, the sandwich method of embedding the spheroids has proven effective with a 95% success rate of proper embedment (n=20) and cell migration observed at all angles from the spheroid. In our validation trial, we saw early time differences (24 hours) between the groups (**Figure 1a**). Cellular migration was consistently increasing in both groups. Lastly, we evaluated the location of D93 staining in the fluorescently labeled collagen gel (**Figure 1b**). Due to the complexity of the signal, we computed the FFT power spectrum of 512x512 sub-regions in each image and calculated the Hurst exponents of each sub-region.[6] We determined that there was a trend towards a higher Hurst exponent in the D93 group compared to the control group indicating more structure present in the D93 images.

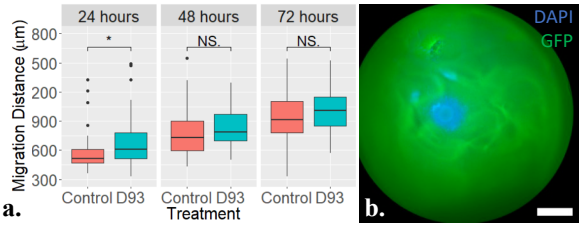

Figure 1. (a) Significant early time differences can be seen in migration distance between groups. (b) Fixed D93 collagen model with fluorescently labeled D93 (green) and DAPI (blue). Scale bar = 1000 µm.

Conclusions: A 3D spheroid model of human breast cancer has been developed and validated for use in exploring the effects of D93 on cellular migration. Significant early time differences were seen between the D93 and control groups and successful labeling of D93 has been achieved. These preliminary data demonstrate high feasibility and ongoing studies are underway for hypothesis testing. We plan to expand our imaging acquisition to include labeling the cryptic site with a fluorophore and imaging via Second Harmonic Generation (SHG) microscopy, a label-free, collagen specific imaging modality. This would allow the individual sites to be examined in more detail using a co-localization image analysis approach. Lastly, we will be purchasing a carbon dioxide regulator for the Cytation 5 which would allow the samples to remain in the instrument for the total duration of the experiment (temperature control is already present). Thus, we plan on increasing our sampling speed to gain the potential of single cell tracking in the model.

References:

1. Gehler, S., Crit Rev Eukaryot Gene Expr. 2013;23(2):139-157.
2. Boraschi-Diaz, I., Front Phys. 2017;5.
3. Freimark, B., Mol. Immunol. 2007;44(15):3741-3750.
4. Caron, J. M., J. Pathol. 2016;186(6):1649-1661.
5. Charoen, K., Biomaterials. 2014;35(7):2264-2271.
6. Marin, Z. et al., Med. Phys. 2017; 44(4):1324-1336.

Acknowledgements: The authors would like to thank Drs. Jennifer Caron and Xianghua Han for their support. Funding supplied by GSBSE and Agilent Research Gift #4624.

Engineering biomaterial-drug platforms from computational peptide design to *in vivo* efficacy

Richa Mishra, Vivek A Kumar
Departments of Biomedical Engineering, Chemical and Materials Engineering, Biology, Endodontics (RSDM)
New Jersey Institute of Technology, Newark, NJ, 07104

Introduction:

Self-assembling peptide hydrogels (SAPH) are a class of injectable scaffolds that present a paradigm in drug development and biomaterials [1,2,3]. Facile self-assembly of monomeric/ multimeric constituents result in high epitope presentation of biological signals. Persistent signaling, *in situ* bolus delivery and demonstrable modification to actuate specific biological responses allowing development of novel classes of biomaterials that behave as scaffolds and drugs. Here, we will describe a few examples of novel peptide-biomaterial drugs that are capable of site-specific delivery to tissue, potentiating numerous tissue remodeling responses:

Tissue regeneration/ revascularization
Drug delivery
IGF driven diabetic fracture healing
COVID therapeutics

We additionally will describe entrepreneurship and innovation helping bridge the gap between academia, industry and clinical medicine.

Methods:

Our work in novel peptide-drug-biomaterial developments begins with rationalized peptide design based on canonical receptor-ligand interactions. Candidate peptides are design for improved stability using macrocyclization and D-peptides. Peptides are synthesized and characterized for supramolecular self-assembly of nM-mM aqueous formulated hydrogels in 1x PBS / saline. Peptides are then tested for *in vitro* and *in vivo* safety and efficacy using a number of mammalian cell and animal models, Figure 1.

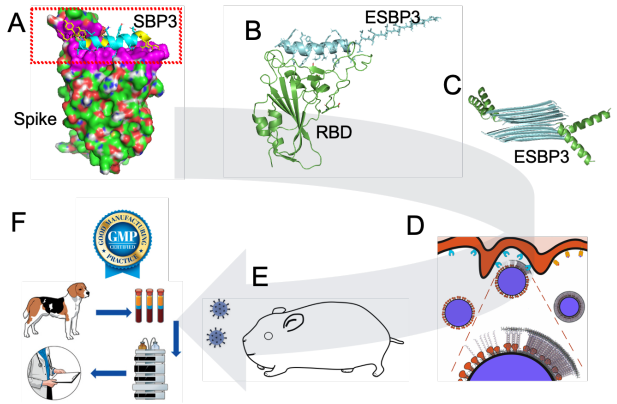

Figure 1. Training translational scientists through the lens of self-assembly. (A) We begin with in silico design using AlphaFold, Crystal, NMR or Cryo-EM receptor-ligand interactions; (B) mutate to ensure binding after conjugation of our platform self-assembling tail; (C) characterize peptides for self-assembly using CD and IR/ EM; (D) demonstrate maintenance of cytocompatibility and *in vitro* efficacy; (E) *in vivo* safety and efficacy; and (F) translation towards larger animal models.

Results:

We have designed a number of peptides biomaterial drugs and herein describe a vignette of key results:

1) SARS-CoV-2 binding peptide:
i) Computational strategy: ACE-2 mimic
ii) *In vitro* efficacy: vs pseudovirus & livevirus (IC50 nM)
iii) *In vivo* efficacy: ongoing in hamster model

2) IGF mimicry:
i) Computational strategy: IGF-1c mimic derived from IGF-IGFR interaction/ stability of binding
ii) *In vitro* efficacy: phos-AKT, looking for phos IGFR
iii) *In vivo* efficacy: ongoing muscle regeneration using these and VEGF mimetic hydrogels.

3) MCP-1 binding peptide:
i) Computational strategy: CCR-2 mimic derived from binding pocket analysis of CCR-2-MCP-1
ii) *In vitro* efficacy: ELISA blocking of MCP-1 Ab binding
iii) *In vivo* efficacy: inflammation model next

4) VEGF binding peptide:
i) Computational strategy: novel "QK" VEGF-A/VEGF-15 mimics; receptor dimerization using self-assembly
ii) *In vitro* efficacy: MST binding to VEGFR1/2
iii) *In vivo* efficacy: pulp regeneration

Discussion:

High resolution structures of protein interactions have given insight into mimicking domains that can recapitulate signaling. We have harnessed this, along with advances in supercomputing and peptide synthesis, to create a robust workflow for (peptide) biomaterial design.

These peptides self-assemble and remarkable, reliably, display their cargo – owing to the stability and self-assembly of the unit assembling domain.

In vitro and *in vivo* these rationally designed materials have shown promise in disease mitigation (SARS-CoV-2) to tissue regeneration (VEGF-mimicry).

Conclusions:

The research vignettes presented showcase a biomaterials that has a milieu of effective function based on computationally design moieties and binding. We have shown efficacy against viral targets and promotion of angiogenesis. This platform is amenable for a multitude of *in vivo* tissue engineering and drug delivery applications owing to its thixotropic (injectable), biodegradable bolus, aqueous formulation that can be exploited for a number of tissue engineering applications.

References:

1. La Manna S. et al. Int J Mol Sci. 2021;22:12662.
2. Li J. et al. Soft matter. 2019;15:1704-1715.
3. Fu K. et al. Biotechnol Adv. 2021;49:107752.

Acknowledgements:

NIDCR R01DE031812 (PI), **NIDCR R01**DE029321 (Co-I), **NEI R15**EY029504 (PI), **NIAMS R21**AR077835 (PI), **NCATS UL1**TR003017 (PI), **NSF IIP** 2041092 (PI), **NSF STTR** 2032392 (Founder/ Pres.).

Cadherin-based cell adhesion consolidates by mechanical polarization in actin cortex through Rac1

Seyedsajad Moazzeni, Kelly Kyker-Snowman, Rick I. Cohen, David I. Shreiber, Jeffrey D. Zahn, Zheng Shi and Hao Lin
Rutgers, The State University of New Jersey

Introduction: The importance of cortical tension and cell-cell adhesion is pervasive in organizing cellular aggregates and tissues and biological processes such as morphogenesis, cancer metastasis, and embryogenesis [1-2]. Their interaction determines if a confluent tissue will be in a "solid" or "fluid" regime, the former showing jamming effects for clusters, whereas the latter facilitates collective migration [3-4]. In contrast to the extensive body of work on single-cell mechanics [5-6] and in tissues and organoids [7], efforts in the multicellular contexts are relatively fewer, and the fundamental understanding of adhesion-tension coupling from single cells to tissues is missing. The current study is a direct evaluation of tension-adhesion coupling in multicellular aggregates of live cells and highlights the crucial role of N-cadherin in driving contact expansion through inducing "mechanical polarization" in F-actin cortical layer.

Methods: Stable L929 subclones were engineered co-expressing LifeAct-mRuby2 and varying N-cadherin-EGFP density per cell (High or LA1NH2, Medium or LA1NM2, and Low or LA1NL4, Fig. 1A) to examine the modulation of adhesion force strength and cortical tension changes during the N-cadherin-based adhesion. L929 fibroblast cells were chosen due to their lack of Cadherin. Tension is quantified by pipette-based aspiration and using Young-Laplace equation for all the cell lines in both suspended single cells (γ_0) and doublets (γ_{cm}) 1 hour after adhesion process started (Fig. 1B). The interfacial tension (γ_{cc}) is also calculated by measuring the contact angle (θ) for doublets (Fig. 1C). Formation of a *de novo* doublet for LA1NH21 cells is thoroughly captured by confocal microscopy in both RFP and GFP channels to find the corresponding remodeling of the cytoskeletal structure of cells during the contact expansion. The tension-adhesion interplay and their responses to Blebbistatin, Jasplakinolide, and NSC23766 treatments are also quantified to investigate the corresponding molecular mechanism.

Results: Figure 1 D-E compares cortical and interfacial tension for suspended singles and doublets of all cell lines; Cortical tension exhibited higher values in the doublets with mature adhesion when compared to single-suspended cells. This tension upregulation was a function of the N-cadherin expression level. The interfacial tensions also exhibited lower values than single cells. These findings indicated that N-cadherin-based adhesion induces "mechanical polarization" in cells, facilitating contact expansion. We further investigated this observation in multicellular aggregates by measuring cortical tension for triplets and quadruplets and found even higher tension values for these multicellular aggregates, which were correlated with the number of interfaces with adjacent cells (Fig. 1F-G). Confocal microscopy revealed an increase in the actin cortex thickness at the cell-medium contact region for fully mature doublets, which corroborates with tension increase, followed by the melting of the actin cortex at the cel-cell contact (Fig. 1H-J). Rac1 inhibition with NSC23766 treatment of cells showed mechanical polarization in adhesion process mediated through downstream signaling pathways between N-cadherin and actin. Myosi II motor protein is the critical component in driving it (Fig. 1K).

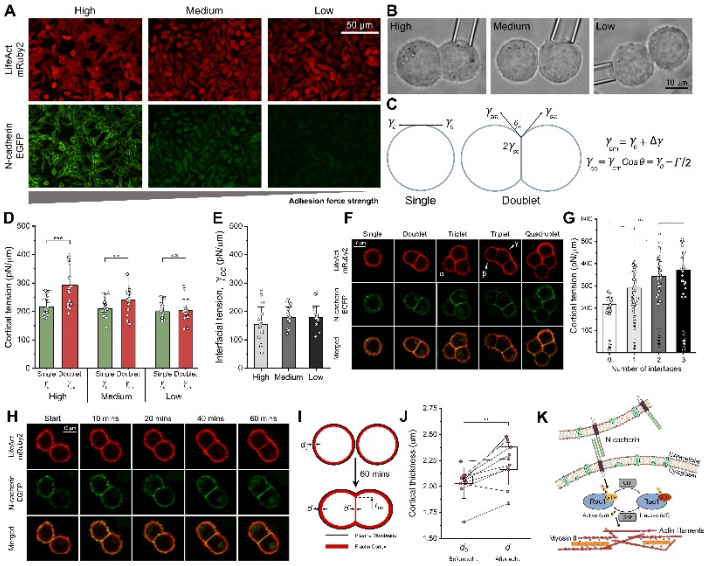

Figure 1. (A) Fluorescent images of engineered cell lines. (B) Doublets of High, Medium, and Low cell lines under aspiration at 37 ˚C. (C) Implemented a physical model to compare tension in single cells and doublets. (D) Comparison of cortical tension between single cells and doublets, and (E) Interfacial tension for all cells. (F) Single, Doublet, Triplet, and Quadruplet LA1NH21 cells. Different conformations of triplets are labeled as α, β, and γ. (G) Measured cortical tension for multicellular groups as a function of interfaces with neighbor cells. (H) A de novo doublet formation in LA1NH21 cell line was captured at 37 ˚C. (I) Schematic illustration of F-actin cortex remodeling during cell-cell adhesion. (J) Cortical thickness before (d_0) and 1 hour after (d) adhesion. (K) Schematic representation of the protein complexes and molecular pathways involved in the function and interaction of N-cadherins and actin filaments.

Conclusions: We demonstrated the critical role of N-cadherin in activating the signaling pathways that modify actin cortical tension. We show that increasing N-cadherin expression and cell-cell inter-faces leads to mechanical polarization of cells in multicellular cell aggregates. This polarization is characterized by an upregulation of tension at cell-medium contact regions and downregulation at cell-cell contact regions, both of them contributing significantly to cohesion strength. These tension regulations are accompanied by F-actin cortex remodeling, providing valuable insight into the tension-adhesion dynamics. These characterizations provide a contextual and quantitative understanding of the more complex mechanical interaction in clusters, aggregates, and tissues.

References:

1. Foty R.A. et al. Rev. Dev. Biol., 2013, 2(5): 631-645.
2. Lecuit T. et al. Nat. Rev. Mol. Cell. Biol., 2007, 8:633–644.
3. Au S. H. et al. PNAS, 2016, 113(18):4947-4952.
4. Bi D. et al. 2015, Nat. Phys., 11:1074-1079.
5. Kollmannsberger et al. Annu. Rev. Mater. Res., 2011, 41:75-97
6. Moazzeni et al., PRE, 2021, 103 (3):032409.
7. Foty R.A. et al. Dev. Biol., 2005, 278:255-263.

Acknowledgements: HL acknowledges funding support from NIH-NCI 1 R21 CA220202-01A1;

Peritoneal Dialysis Risk of Infection Detection

Ismael Montero-Rinaldi, Julia Vardiman, Rahul Panoli and Connie L. Hall, PhD
The College of New Jersey

User Needs:

1a) Use Case: Patients that are undergoing peritoneal dialysis (PD) at home are at risk for infection. Patients are in need of a reliable means of detecting potential signs of infection without the help of a medical professional. This can be difficult, particularly for the elderly patients. An early detection system that alerts patients of infection risk and the need to seek medical attention is needed.

1 b) Problem Impact: The current method patients use for detecting peritoneal infection is to attempt to read an article of text through the filled dialysate waste bag. The difficulty in this method to assess possible infection can lead to serious risk in peritoneal dialysis users. This device is a way to address the difficulty in detecting early infection in patients undergoing peritoneal dialysis treatment that alerts the user when changes in dialysate turbidity are detected.

2) Design Inputs

2.a) Constraints: The device must detect early signs of infection by detecting a change in absorbance as a result of increased turbidity. The path length from the LED to the sensor in the device must be the same length every time. The device must also operate within a budgetary constraint of being built using $375.

2 b) Requirements: The device will determine a change in turbidity when the white blood cell concentration is greater than 100 leukocytes/mm³ [1]. Physicians use this as a benchmark for infection. The device must alert the user with a visual and audible signal when signs of infection are detected.

Solution:

3 a): Design - Intended Uses: The device will be used at home by peritoneal dialysis patients. It will be lightweight and easy for the patient to attach the device to the dialysis system. A concentration higher than 100 leukocytes/mm³ [1] is an indication of peritoneal infection. Our device uses a UV LED and a sensor to measure the changes in absorbance of the waste dialysate.

3 b) Build - DEMO

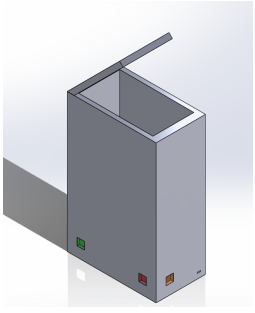

Figure 1: 3D Model of Device

A model of the design can be seen in Figure 1 above.

Verification Results:

4 a) Introduction: If the device can detect infection in peritoneal dialysis users before the eye can determine a change in clarity in the dialysis solution, it can alert users to seek medical attention prior to serious infection.

The basis of this medical device design is that turbidity increases as leukocyte concentration increases.

4b) Methods: For proof of concept, an experimental procedure was created and performed to determine the wavelength at which the peak absorbance occurs for differing concentrations of leukocytes. This test relates to the requirement that the device must determine a change in turbidity when the concentration of white blood cells is greater than 100 leukocytes/mm³ [1]. A solution with a mixture of leukocytes and PBS was created and placed in a spectrophotometer where measurements were recorded at 80, 90, 100, 110, and 120 leukocytes/mm³

4 c) Results: The wavelengths at which the presence of leukocytes resulted in a peak absorbance level were determined. The results are illustrated in Figure 2.

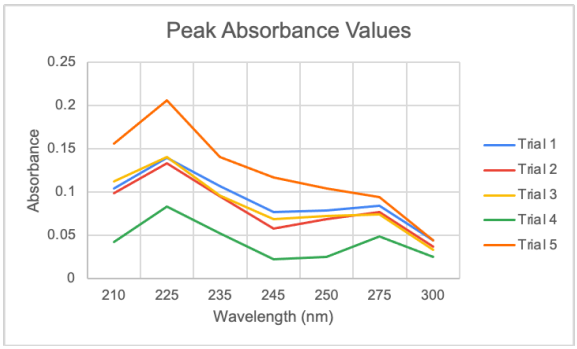

Figure 2: Spectroscopy Data

Peaks were identified at 225 nm where the absorbance then declines and suddenly begins to rise again at 275 nm. Thus, the device will measure absorbance at one of these wavelengths.

Conclusion:

5 a) Summary: The requirements of the device's design have been met without violating any previously mentioned constraints. The results allowed the group to determine which wavelength to measure at while the device is running.

5 b) Revisions: A limitation that arose was that an LED that operates at 225 nm was not realistic for the scope of this project due to the budgetary constraints that were set. After researching adequate LEDs, it was found that those that operate at 225 nm would have exceeded the team's budget alone. As a result, an LED at 275 nm was purchased.

5 c) Impact (Future Version): To increase the impact of the design, the team would acquire an LED that operates at 225 nm due to there being higher absorbance at this wavelength. The team still expects that leukocytes will be detected using the 275 nm LED. The device would be more accurate in recognizing a risk of infection if this revision was made.

References:

1. Xu R. PD Perit Dial Int. 2013;33(4):436–444.

Acknowledgements: Funding provided by The College of New Jersey's Engineering Department

Designing a Local Field Potential Apparatus (LFPA)

Arun Aryal, Fahad Mahmood, Akhil Nagulapalli, Fei Xuan Phua, Christopher Piccininni,
Joel Schesser PhD, Jonathan M. Grasman PhD
Department of Biomedical Engineering, New Jersey Institute of Technology, Newark, NJ, USA

1) User Need:

1.a) Use Case

Labs conducting cell culture and neuronal research requiring affordable tools to record 3D neuronal activity.

1.b) Problem Impact

Current methods of measuring neuronal activity have limitations in 3D space including patch clamping, which can only measure one cell at a time, making such a method impractical for high throughput experiments or for measuring activity from larger neuronal populations. One such solution is the development of an improved local field potential (LFP) apparatus, which can measure larger populations, use a Faraday cage to improve the signal-to-noise ratio (SNR), and have simpler, more affordable assembly. These features could help investigate the effects of drugs on neuronal regeneration or diseases in 3D tissues.

1.c) Scope (Objective)

Our project aims to create a cost efficient apparatus capable of analyzing LFP measurements from dorsal root ganglia (DRG) or spinal cord explants in 3D culture.

2) Design Inputs

2.a) Constraints:

To record LFPs of neuronal cells, the device requires sensitive electrodes (μV range) and amplifiers (1000X gain) to increase signal gain while reducing noise using external noise eliminators and digital signal processing methods.[1] It must fit within a laminar flow hood (LxHxD: 36x30x24 in) to maintain an aseptic field. To achieve a balance of effectiveness, ease of use, and affordability, we have decided to fabricate several components while outsourcing some more critical components to ensure functionality. The electrodes must fit within a 35 mm petri dish and utilize currents < 50 mA to prevent cell damage.

2.b) Requirements:

To fit within a laminar hood while maintaining an SNR >20dB, the Faraday cage shall be constructed using galvanized wire mesh (24x18x18 in). The stimulator shall send a safe current (< 50 mA) to the stimulating electrode to stimulate the cells. The resultant signal will be recorded, amplified (1000X gain), digitized, and digitally processed. Throughout this process, the device must allow for automatic data analysis and remote operation.

3) Solution

3.a) Design - Intended Use:

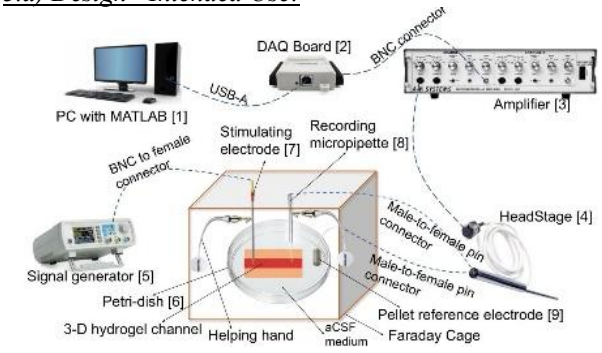

Fig 1. Schematic design of the LFPA.

Our device consists of 4 major components: a signal generator, electrodes to interface with the neuronal cultures, an amplifier, and MATLAB script to analyze and output the data. The signal generator will be used to provide an input current via a stimulating electrode. The stimulating electrode will be connected to the signal generator to provide an initial stimulus to the cells, and the recordings will be collected with a glass-pulled recording electrode, which will be placed adjacent to neurons incubating in artificial cerebrospinal fluid. Signals will be normalized to background using a reference electrode. Electrodes will be positioned using a dissecting microscope and fixed in place with helping hands to reduce physical noise. The entire system will be enclosed within a Faraday cage to eliminate environmental electrical noise to maintain good SNR and amplified through the amplifier for analysis in MATLAB outside the Faraday cage.

4) Verification Results

4.a) Introduction (i = 1)

The device must output an LFP signal resembling those in Fig 2, obtain an SNR > 20dB, record peak-peak distance and amplitude for the voltage-time graph, and record the frequency interval from the Fast Fourier Transform (FFT).

4.b) Methods (i = 1)

The signal and noise will be determined from the FFT. The noise is distinguished from the signal (1-300Hz) as peaks at certain frequency intervals (50/60 Hz).[2] SNR will be calculated using the formula: SNR = 10log(S/N), where S = power of the signal bins, N = power of the noise bins.[3] The FFT can be applied to the measured and expected signals to determine similarity of the frequency ranges.

4.c) Expected Results (i = 1)

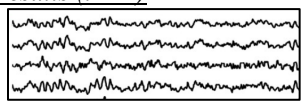

Fig 2. Representative LFP trace (sampled from ref).[4]

The voltage vs. time graph of the measured signal should be similar to the data displayed in Fig 2.

5) Conclusion

5.a) Summary:

The device is under development and requires further testing to assess if it meets the user requirements.

5.b) Revisions:

The accuracy of our anticipated results could be enhanced with improved SNR through the addition of a Biopac amplifier, a HumBug noise eliminator, and/or the use of an anti-vibration table with micromanipulators.

5.c) Impact (Future Version):

The product could potentially aid in minimally invasive testing of PNS drugs for treating neuronal conditions, improving treatment for patients, and offering alternatives to invasive procedures like peripheral nerve stimulation.

References:

1. S. Reed, S. Jego, and A. Adamantidis, "Electroencephalography and Local Field Potentials in Animals," in Basic Electrophysiological Methods, E. Covey and M. Carter, Eds. Oxford University Press, 2015, p. 0. doi: 10.1093/med/9780199939800.003.0007.
3. A. Fernández-Ruiz et al., *J. Neurosci.*, vol. 32, no. 15, pp. 5165–5176, Apr. 2012.
2. M. Welvaert et al., *PLOS ONE*, vol. 8, no. 11, p. e77089, 2013
4. Destexhe, A. & Bedard, C. Local field potential. *Scholarpedia* **8**, 10713 (2013).

Acknowledgements:

We acknowledge funding from the NJIT Student Seed Grant Program and startup funds provided by NJIT.

Functional imaging of the brainstem during stretch-evoked responses under different task instructions

Rebecca C. Nikonowicz, BS, Fabrizio Sergi, PhD
University of Delaware.

Introduction: The reticulospinal tract (RST), while secondary to the corticospinal tract (CST), may assume considerable importance for recovery from corticospinal lesions. Methodological constraints have limited our capability to directly measure in-vivo function of the RST. The reticular formation (RF), a set of brainstem nuclei originating the RST, may modulate the amplitude of a long-latency response (LLR), a stereotypical response evoked in stretched muscles, with response times comprised between 50 and 100 ms. Because LLRs are "semi-reflexive" responses, they have smaller between-subject variability compared to voluntary motor tasks. As such, precisely evoked LLRs may be a means to reliably stimulate the RST to measure motor-related activity via functional magnetic resonance imaging (fMRI). Our group has recently developed StretchfMRI, a non-invasive imaging method that has enabled us to map motor function in the RF in-vivo for the first time.[1] StretchfMRI is enabled by the unique integration of robotics, surface electromyography (sEMG), and fMRI. Because the RST is thought to contribute to the increase in LLR amplitude (LLRa) associated when participants are asked to "resist" a perturbation, fMRI during LLRs under different task goals may be a highly specific method to decouple the contribution of the CST and RST to LLRs.[2] In this work we have extended the capabilities of StretchfMRI to measure LLR-related fMRI signal under different task instructions, designed to differentially engage the CST and RST, by building a new MR-compatible robotic perturbator, the Dual Motor StretchWrist (DMSW) and using the device in experiments with sEMG and fMRI.

Methods: *A. Dual Motor StretchWrist*

We have developed an MRI-compatible 1 degree of freedom wrist robot, the DMSW, capable of imposing controlled perturbations to the hand about the wrist flexion/extension axis in the range of θ_{FE} = [-45, 45]° with up to 6 Nm of peak torque (Fig 1B). It is actuated by two ultrasonic piezoelectric motors connected in parallel (EN60 motor, Shinsei Motor Inc., Japan) via a capstan transmission. A controller ensures proper parallel function of the motors, including matching motor displacements and velocities.

B. Protocol Validation with sEMG

To confirm the DMSW's ability to reliably elicit LLRs during both "Yield" and "Resist" conditions, a preliminary study was conducted outside the MRI scanner on 5 participants using sEMG to measure muscle activity. Participants completed a series of ramp-and-hold perturbations at 150 deg/s, in extension. Electrodes (Delsys Trigno Avanti, Natrik, MA) were placed on the flexor carpi radialis (FCR) and the extensor carpi ulnaris. Participants were given a "Yield" or "Resist" instruction prior to each trial and performance feedback based on average torque measured during the 75-125 ms post perturbation onset was provided after every "Resist" trial to standardize the amplitude of evoked LLRs.

C. fMRI Pilot Experiment

fMRI images were collected using a whole-brain sequence (Multi-Band Accelerated EPI with 2x2x2 mm^3 voxel resolution, TR=1225 ms), together with a T1-weighted structural scan (0.7x.0.7x0.7 mm^3, TR=2300 ms) used for registration and normalization.

10 healthy, right-handed participants were recruited for a pilot study. Participants were screened for MRI safety and then completed a series of familiarization tasks with the robot to determine personalized torque target values and ensure they were comfortable with the device and the task instructions. Participants were then placed in the scanner bore with the robot (Fig 1A-B) and completed two task sessions of blocked perturbations during fMRI sequencing lasting approximately 15 min each. Conditions included were 1) Yield, 2) Resist, 3) Yield 2. The secondary Yield condition involved a slow perturbation (35 deg/s) as a control for background torque and hand movement activity.

Results: Statistical analysis of sEMG data collected during the protocol validation experiment show significantly greater LLRa in "Resist" relative to "Yield" (Resist: 4.483±0.966 n.u., Yield: 1.205±0.964 n.u., p=0.0010). Preliminary analysis of functional images shows increased activation in the brainstem primarily localized in the ipsilateral and contralateral medulla and midbrain, contralateral pons, and primary motor cortex in the resist condition (Fig 1D).

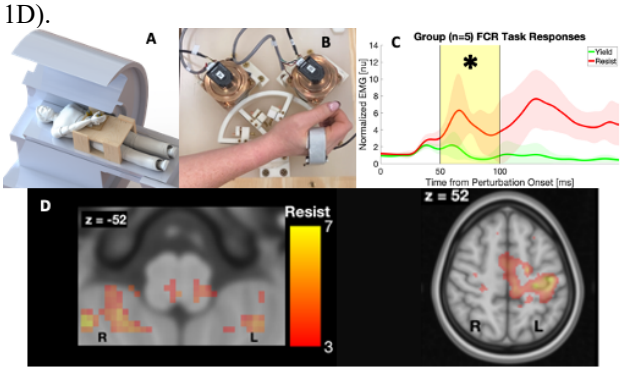

Figure 1. (A) MRI experimental setup. (B) DMSW. (C) sEMG of the FCR during Yield and Resist conditions. (D) Statistical parametric maps of activation in the resist condition (t_{min}=3).

Conclusions: We developed a new MRI-compatible robot, the DMSW, and validated a new experimental protocol based on the DMSW to evoke motor responses under different task instructions. Moreover, we found stretch response activity associated with the "resist" task instructions in the medulla. Future work will aim to establish the effect of different data processing strategies to improve the signal-to-noise ratio of fMRI of the brainstem, and to isolate the contributions of the brainstem to voluntary responses and LLRs.

References: 1. Zonnino, A. Sci. Rep., 2021;11(1):1-21.

2. Kurtzer, I. Front. Int. Neur., 2014;8:99.

Acknowledgements: Work funded by NINDS NIH R21NS111310 and DE-INBRE NIGMS P20GM103446.

Silk Wrinkled Surface Patterns in 3D Environments

Kerrin O'Grady, Elizabeth Oguntade, James Henderson.
Biomedical and Chemical Engineering, BioInspired Institute, Syracuse University.

Introduction: Mechano-structural cues, such as surface topography, regulate cell behavior. A common topography used and studied in tissue engineering is surface wrinkling, as it creates topographical patterns that share features with some naturally occurring systems. In material bilayer platforms consisting of a thin film attached to a compliant substrate, there is a modulus mismatch between the film and substrate, so the presence of a compressive load will induce the thin film to buckle to a wrinkled state. Most wrinkling research to date has been performed using thin-film buckling on two-dimensional (2D) substrates, and there has been limited work on surface wrinkling on three-dimensional (3D) environments that may better support cell-to-cell interactions and tissue remodeling. In prior work, shape-memory polymers (SMPs) have been used to induce wrinkle formation *in vitro*.[2] Separately, silk fibroin (SF) has been studied as a surface modification to optimize biocompatibility and cytocompatibility. As a step toward facile surface wrinkling on 3D surfaces, here our goal was to study the use of a silk as the thin film in SMP-actuated surface wrinkling. To achieve this goal, we modified the surface topography and functionality of 3D scaffolds for cell culture by dip coating 3D printed SMP scaffolds that can autonomously actuate silk wrinkles upon heat-induced contraction of the SMP.

Methods: Using an extruder (3Devo composer 450), semicrystalline thermoplastic polyurethane pellets (MM-4520, SMP Technologies, Inc.) with a glass transition temperature (Tg) of 45 °C were extruded to acquire a spool of SMP filament for 3D printing. The filament was loaded into a 3D printer (Creality Ender 3) to fabricate and program the 3D scaffolds. To enable the fabrication of SMPs that are pre-programmed and can undergo shape transformation following printing, we used our recently developed technique known as programming via printing (PvP).[3] To control and vary the printing parameters, 3D scaffolds were created in computer aided design software and sliced using Ultimaker Cura. Samples were printed with a speed of 30 mm/s, nozzle temperatures from 200-220 °C, and print flow rate of 125 %. Following fabrication, the programmed 3D scaffolds were dip-coated with varying concentrations of silk fibroin (SF; 1 %, 2 %, and 3 %) for later comparison. The SF-SMP scaffold was then treated in methanol to induce secondary structural changes in the silk network and prevent dissolution of SF in media. To form silk wrinkles on the surface of the SMP-based 3D scaffold, the SMP was heated above its Tg in an isothermal oven. Optical microscopy was used to image the surface of the 3D scaffold before and after wrinkle formation. Cytocompatibility of the silk wrinkled structures was evaluated by seeding and culturing mouse embryonic fibroblasts for varying time points on wrinkled or non-wrinkled scaffolds and then staining with LIVE/DEAD to qualitatively assess cell viability.

Results: Optical microscopy confirmed the presence of wrinkle topography produced by buckling of the silk thin film on the surface of the SMP-scaffolds **(Fig 1A)**. With a higher silk concentration, we observed wrinkling formations that had larger wavelengths and amplitudes. We also observed an increase in trapped strain when dip-coated in a lower concentration of SF-solution **(Fig 1B)**. Preliminary experiments indicate high cytocompatibility of cells on the SF-coated 3D scaffolds (data not shown).

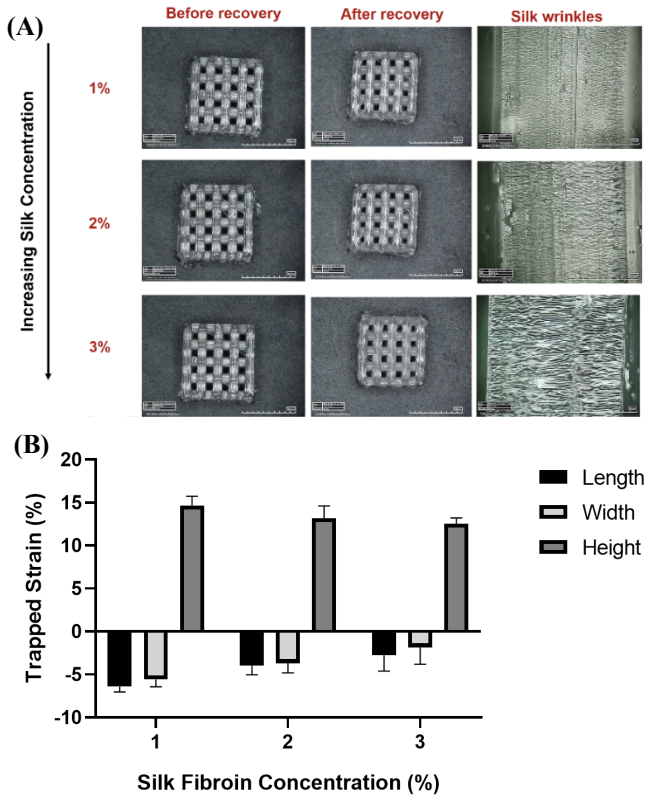

Figure 1. (A) Optical images of silk-wrinkled topography induced thermally by contraction of SMP scaffold. **(B)** Analysis of trapped strain with respect to varying SF concentrations.

Conclusions: We have demonstrated and characterized the fabrication of 3D silk wrinkle topographies on dynamic 3D scaffolds. These silk wrinkles may be useful to serve as a cell culture platform functionalization for biomaterial applications. We will need to further investigate the influence of mechanical properties on the 3D surface wrinkling. This work should enable the development of biomimetic cellular microenvironments, which is crucial to understanding the effect on cell behavior and fabricating functional tissue constructs.

References: [1] T.P. Nguyen et.al., Polymers, 2019, 11, 1933. [2] P. Yang et.al., Soft Matter, 2013, 9, 4705. [3] K. Pieri., Dissertations-ALL, 2020, 1256. https://surface.syr.edu/etd/1256

Optical Finger Phantoms for Use in Pulse Oximetry

Peace E. Okiye, BS[1], Mohammed Shahriar Arefin[1], MS, Chetan A. Patil[1], PhD
[1]College of Engineering, Temple University, Philadelphia, PA,

Introduction: Tissue mimicking optical phantoms are an important tool for providing a standard for the evaluation, characterization, and calibration of optical systems that also does not require the use of living subjects. This is an added benefit that aids in the development of medical devices such as Pulse oximeters which are widely used medical devices that provide information on blood oxygen saturation (SpO_2). Recent clinical studies have showed troubling results stating that pulse oximeters overestimate SpO_2 in subjects with darker skin, which can cause a delay in treatment for these subjects [1,3]. An improved understanding of the underlying sources of measurement bias and accuracy reported in clinical studies[1] warrants the study of tissue mimicking optical phantoms for pulse oximetry. Tissue mimicking phantoms typically require fabrication of a three-dimensional matrix which contains different inks, dyes, and scattering particles to realize a target set of optical properties characteristic to a specified tissue [4,5]. In the skin, pigmentation arises primarily from melanocytes in the epidermis. Reproduction of a thin superficial layer with a range of colors similar to human skin tones in tissue mimicking optical phantoms remains a challenge. The application of cosmetic makeup products to the superficial surface of tissue phantoms offers one possible approach employing a substance with consistent properties across the visible spectrum [2]. In this abstract, we report the development of an optical finger phantom for evaluation of pulse oximetry that employs the use of cosmetic products to simulate the epidermal layer. We evaluate the optical properties of the materials used in phantom construction to characterize their suitability for a pulsatile pulse oximetry finger phantom.

Methods: Optical phantoms were created using the SYLGARD^{TM} PDMS silicone elastomer. Silicone was cured using a 10:1 ratio of curing agent to elastomer, 1.25" x1.25" phantom squares were created. This is then mixed, debubbled, and baked in a pressure oven at 30 psi. The chromophores used in these phantoms included 0.2g of dark powder foundation (Island Beauty Compact Press Powder in Rich Brown) and 0.2 g of light powder (Maybelline Fit Me Loose Finishing Powder in medium deep) suspended in 5mL of 200 proof ethanol to create a stock solution. A portion of this stock was aliquoted into the PDMS matrix, this value changes depending on the amount of matrix being created. For about 4 g of PDMS, 43 µL was used. A TiO_2 stock was created using 8 g of TiO_2 and 45 mL of 200 proof ethanol. For this same finger, an aliquot of 171 µL was used A mixture of 8.14 g of red acrylic paint and 2.02 g of blue acrylic paint was mixed with 40 g of ethanol and an aliquot of 214 µL was used.

Results: The optical properties from the powder foundation suspension were analyzed using Inverse Adding Doubling (IAD) software. The suspension was aliquoted into an 11.5 mm cuvette and then analyzed on a spectrum of 400 nm – 1000nm, but due to a large amount of noise after 940 nm, analysis ended at 940 nm.

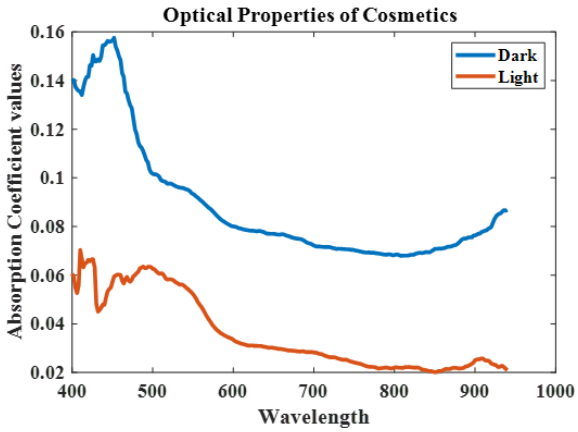

Figure 1: Absorption coefficients values of both light and dark pressed powders.

(**Figure 1**) shows the μ_a or the absorption coefficient of a light and a dark pressed powder. The μ_a of the darker powder indicates more absorption compared to the lighter powder.

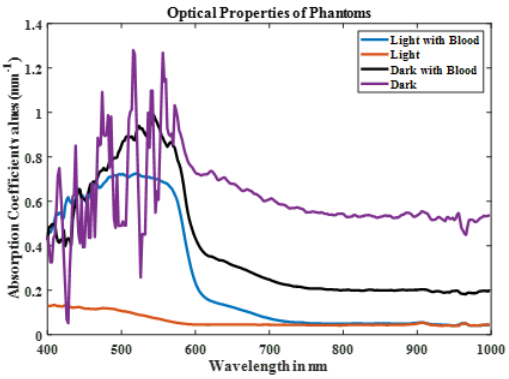

Figure 2: Scattering coefficient values of phantoms created with light and dark pigment.

(Figure 2) shows the absorption coefficients of phantoms created with the red/blue paint mixture meant to create at 660 nm and the cosmetic makeup. These results show much noise in 400-600 region due to very low intensity transmittance measurements.

Conclusions: The use of tissue mimicking optical phantoms has a promising future in clinical studies. This study aims to eventually create microfluidic phantoms using the methods described to create the phantom matrix. Further analysis will be performed on the phantoms to ensure they represent the optical properties needed for pulse oximeter phantoms.

References:

1. Fawzy A, JAMA Int. Med. 2022;182(7):730-738.
2. Durkee M.S. NLM. (2018);10.3791/57031.
3. Sjoding M.W. NEJM. (2020); 383:2477-2478.
4. Sieryi O, SPIE. (2020);10.1117/12.2560174.
5. Hacker, L, NBE, (2022);6;541-558

Instrumenting Nordic Walking Poles for Quantitative Gait Assessment

Dominic R. Oliveri, Julia F. Kilroy, Conor D. Landry, John P. Minogue, John F. Drazan, Ph.D.
School of Engineering, Fairfield University, Fairfield, Connecticut.

Introduction: Assistive walking devices, such as canes, crutches, or Nordic walking poles (NWP) are commonly used by post-surgical patients, the elderly, and individuals with ambulatory difficulties [1]. Fundamentally, these devices redistribute load from the lower body to shield healing tissues during recovery or to compensate for reduced function. These devices have potential to provide individualized data for user mobility and health by monitoring loading patterns through the device. Unfortunately, there are few commercially available instrumented devices, and those that are available are cost prohibitive. To address this issue, we have developed an instrumented NWP. Our design requirements include that it: 1) Requires minimal alterations to an existing device, 2) serves as research tool in both the laboratory and real-world settings, and 3) be low-cost and easy to manufacture.

Methods: Our final design was instrumented with a load cell to measure applied axial forces along with a low-profile, 3-D printed electronics housing that used an Arduino with a Bluetooth module that connects via serial to either a smart phone or computer. We cut a NWP underneath the handle and instrumented with a 100-kg load cell (Calt, DYMH-103) attached within the shaft by a plug interface custom machined out of 6061 aluminum. Each plug was tapped with M6 x 1.0 threading to secure the load cell (Fig. 1) The data acquisition module consisted of an ESP32 and an HX711 amplifier for Bluetooth transmission mounted onto a custom 3-D printed sensor unit housing along with a 9V battery (Fig. 2). The sensor unit (Fig. 1) consisted of two separate 3-D printed pieces fastened together by a system of bolts. The NWP force measurement system was calibrated using a loadsol device. Varying amounts of force were manually applied to the NWP that sat on top of the loadsol, which read out force data via Bluetooth to a smart device. The peaks in the force vs. time data from the load cell and loadsol were analyzed and averaged to produce a best fit line that was used to determine the calibration coefficient for the NWP while also establishing device accuracy.

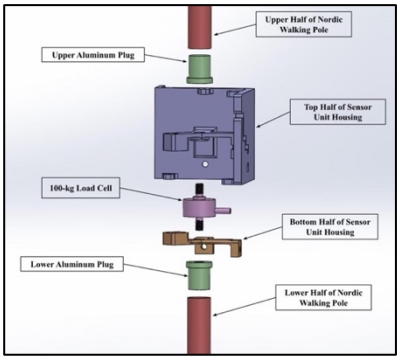

Figure 1. Exploded view of the NWP assembly in SOLIDWORKS.

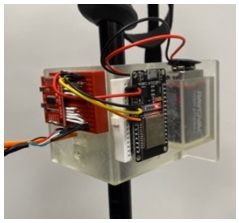

Figure 2. Electronics within the sensor unit housing.

Results:

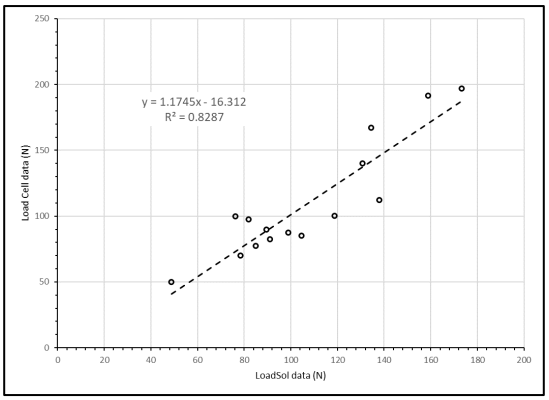

Figure 3. A graph of the peak forces applied to the load cell compared to the peak forces read from the loadsol. The equation and R-squared value for the linear regression line are shown.

The linear regression from the loadsol calibration test is shown in Figure 3. The R-squared value was 0.8287 and the slope was 1.1745. The total cost of the NWP was approximately $154.

Conclusions: The results from the linear regression give an R-squared value and slope that are close to 1, suggesting that the NWP reads out force data that is close to the measurement from the loadsol. However, the agreement between the NWP and the reference force may have been impacted by force sharing between the device housing and the load cell. We expect agreement to increase in future designs. We used the NWP as a proof-of-concept; however, this approach can be extended to other devices such as crutches and canes. Other instrumented devices in literature, such as the NWP in Szrek et al. [2], propose a wired system using strain gauges. The instrumented cane in Mekki et al. [3] has a wireless system, but the device housing is bulky and is located at the foot of the cane, which could potentially increase the moment of inertia during use. However, both proposed designs cost more than $500 to produce. Based on the total cost and calibration procedure, our NWP provides a low-cost, accurate force measurement system that may be used as a clinical gait assessment tool in the future, where the quantitative feedback given by the NWP can assist in monitoring patients' limb load and gait patterns while also providing users with ambulatory difficulties proper support and increased mobility.

References:

1. Liggins A.B. et al. Proc IEEE Annu Northeast Bioeng Conf. 2002;28:15-16.
2. Szrek J. et al. Proc Int Scientific Conf: Computer Aided Eng. 2019;1:790-794.
3. Mekki F. et al. IEEE Int Symp MeMeA. 2017;414-419.

Acknowledgements: This work was supported by the School of Engineering at Fairfield University and an anonymous donor through the Sapere Aude Fund.

Physical Characterization of Spin-Coated Polydimethylsiloxane (PDMS) for Applications in Lab-on-a-Chip Technology

Melissa Orlick, Madison Stiefbold, Leo Q.Wan.
Department of Biomedical Engineering, Rensselaer Polytechnic Institute.

Introduction: Polydimethylsiloxane (PDMS) is a commonly used polymer for tissue engineering purposes due to its non-cytotoxic characteristic and ability to be manipulated as a liquid and cured into solid structures. Spin-coated PDMS has been used for substrates for cell-culture in lab-on-a-chip technology [1]. PDMS can be selectively spin-coated over specific areas of the underlying substrate to spatially control cell attachment and growth, often by using tape or another thin, impermeable layer on the substrate [1, 2]. Using these methodologies, variability in polymer thickness has been observed, specifically a "snowdrift" effect of polymer buildup along the edge of the tape boundary. This variability may be due to capillary action rather than driven by the directional force of spin-coating, but nonetheless can be detrimental to the accuracy of calculations of cell force propagation as done in previous work [2]. Further characterizations and analysis of this phenomena can improve control of variability in PDMS thickness and modeling of spin-coated PDMS on lab-on-a-chips.

Methods: Glass microscope slides were cleaned with 70% ethanol and dried with nitrogen gas. The slides were divided into approximately five equal horizontal rectangles with tape covering the second and fourth of these regions. Sylgard 184 PDMS was made in two base to curing agent ratios, 19:1 and 10:1. The PDMS was spin-coated on the glass slides using an SCS G3P-8 Spin Coater for five minutes at either 3000 rpm or 5000 rpm. Four experimental groups of n=2 samples were made with 19:1 PDMS at 3000 rpm, 19:1 PDMS at 5000 rpm, 10:1 PDMS at 3000 rpm, and 10:1 PDMS at 5000 rpm. Once spin-coated, the tape was removed and the PDMS slides were cured for two hours at 100˚C. Once prepared, a Dektak 8 stylus profilometer (Veeco, Plainview, NY) was used to obtain six to twelve sets of height measurement with a resolution of 0.167 µm per data point and a stylus force of 5 mg. Custom MATLAB code was used to analyze the thickness of the PDMS and statistics on the variability of the polymer height. A Two-Sided T-Test was used to compare each experimental group's PDMS thickness, height variation, and "snowdrift" phenomena normalized peak value using MiniTab. The normalized peak value is the ratio of the height of the peak and the average polymer height. This measures how high the peak is, or how much "snowdrift" occurs given the experimental conditions.

Results: An example of the data produced from the profilometer can be seen in Fig. 1A. The "snowdrift" effect, polymer region, and exposed glass region (formerly tape) are labeled. The PDMS thickness of the 19:1 5000 rpm experimental group was different from the other treatment groups ($p<0.05$) (**Fig. 1B**). The 10:1 3000 rpm group also had a statistically significant difference in polymer thickness from the 19:1 3000 rpm and 10:1 5000 rpm groups ($p<0.05$). In regard to variation of the spin-coated polymer, there was statistically significant difference found between the 19:1 3000 rpm and 10:1 5000 rpm groups, and between the 10:1 3000 rpm and 10:1 5000 rpm groups ($p<0.05$). Statistically significant differences for the normalized peak value was found between the 19:1 5000 rpm and 19:1 3000 rpm groups, the 19:1 5000 rpm and 10:1 5000 rpm groups, and the 19:1 5000 rpm and 10:1 3000 rpm groups (**Fig. 1C**) ($p<0.05$).

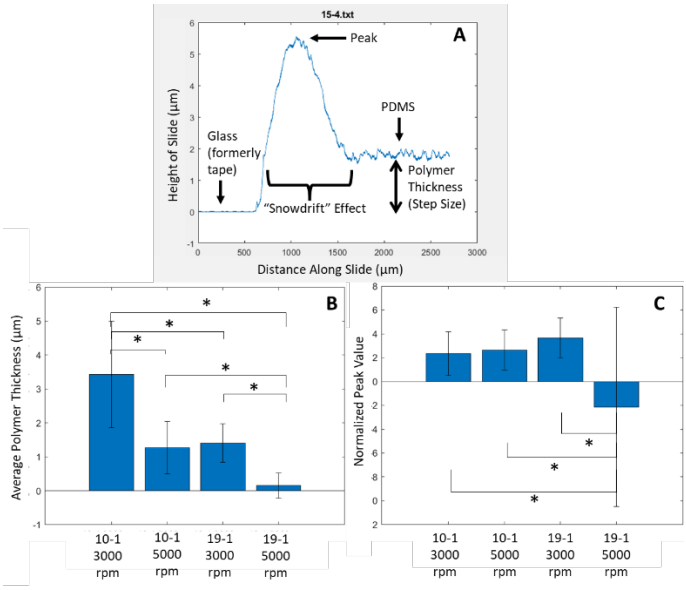

Figure 1. A) Labeled profilometer reading from sample with 10:1 PDMS concentration spin-coated at 3000 rpm. B) Average thickness of spin coated PDMS and standard deviation as categorized by experimental group. C) Average normalized peak value and standard deviation as categorized by experimental group.

Conclusions: Spin-coating PDMS produces a thin yet variable polymer onto an underlying substrate. The thickness of the PDMS depends on the base: curing agent ratio and the speed of spin-coating, as supported by significant differences in PDMS thickness in each experimental group. Further analysis must be conducted to determine if PDMS concentration and spin-coat speed affects the amount of variation in height of the polymer. Additionally, further analysis is necessary to conclude if the severity of the "snowdrift" effect, as measured by normalized peak value, depends on spin-coating conditions, or if this observed phenomena can be categorized as capillary action. The relationship between PDMS concentration, spin-coat speed, and polymer thickness can guide the optimization of lab-on-a-chip technology, creating a more uniform substrate which will improve the accuracy of mathematical analyses of cellular force propagation.

References:

1. Grosberg, A. Lab on a Chip. 2001;11(24):4165-4173.
2. Knight, M.B. Biophysical J. 2016;110(7):1615-1624

Emotional Facial Expression Analysis of Children with and without Autism Spectrum Disorder

Zuhal Ormanoglu[1], Candida Barreto[1], Yigit Topoglu[1], Adrian Curtin[1], Jessica Day-Watkins[2], Brigid Garvin[3], James Connell Jr.[4], Elisabeth Sheridan[2], Karen Heffler[5], David Bennett[5], Hasan Ayaz[1,6-9]

1 School of Biomedical Engineering, Science, and Health Systems, Drexel University, **2** AJ Drexel Autism Institute, **3** St. Christopher's Hospital for Children, **4** School of Education, Drexel University, **5** Department of Psychiatry, Drexel University, **6** Department of Psychological and Brain Sciences, Drexel University, **7** Drexel Solutions Institute, Drexel University, **8** Department of Family and Community Health, University of Pennsylvania **9** Center for Injury Research and Prevention, Children's Hospital of Philadelphia.

Introduction: Autism Spectrum Disorder (ASD) is a developmental disorder characterized by deficits in social communication, as well as the presence of restricted and repetitive patterns of behaviors with a global prevalence rate of 1%. Children with ASD have deficits and neural differences in recognizing social contingencies, specifically those involved in facial processing [1], human sound recognition [2], and attention to biological motion [3]. Although children with ASD have difficulties perceiving faces, voices, or biological motion as socially relevant [1,2], in general, they show higher sensitivity to sound and sight [4, 5]. These atypical sensory findings correlate to a host of ASD symptoms [6, 7] and lead to a wide variation in ASD presentation and severity.

In this study, we aim to compare facial emotional expressions of typically developing (TD) children and children with ASD during video viewing of social and non-social content. Our main hypothesis is that children with ASD will exhibit fewer facial expressions compared to TD children.

Methods: In this preliminary analysis, three participants (mean age=3.48 years old ± 0.14, two TD children) were used. Participants' face recordings were captured using a high-resolution camera (Logitech HDPro Webcam C920) and during recording, children did not wear face masks and made minimal head movements. Each child watched a total of four videos and each video was approximately 2 minutes long. Two of the videos had social content, and the other two had nonsocial content. For the social condition, clips were focused on human interaction, i.e.., an actor engaged with the camera or other people communicating, singing, and dancing. In contrast, the nonsocial condition featured inanimate objects without any humans or human characteristics (i.e., a Rube Goldberg chain reaction machine).

For facial expression analysis, we used Py-Feat, an open-source facial expression emotion recognition toolbox [9], to automatically detect the faces and label the facial expression based emotion of children for each video. The algorithm classifies facial expressions into seven units based on the FACS system [4]: neutral, happiness, surprise, sadness, anger, disgust, and fear. We used models *retinaface* for face localization, *mobilefacenet* for facial landmark detection, *img2pose* for face pose estimation, *SVM Classifier* for Action Unit detection, and *resmasknet* for emotion detection. We obtained one prediction for every 30 frames and binned them in 10-second intervals to get probabilistic estimates of each emotion and neutral distribution. We removed the parts of the videos where the child's face could not be detected by the algorithm. For this analysis, we calculated an emotion expression index (i.e., 1-neutral) that ranges from 0 to 1, and represents emotion (happiness, surprise, sadness, anger, disgust, and fear) expressions. A mixed model analysis with repeated measures with group (ASD vs. TD) and condition (social vs. non-social) as a fixed factor was applied in NCSS (NCSS, LLC. Kaysville, Utah, USA).

Results: Emotion expression index extracted from frame-by-frame face image processing was subjected to statistical analysis. Results show a significant *Group* main effect ($F_{1,135}$= 16.43, p<0.0001) and a significant *Condition* main effect ($F_{1,135}$= 14.85, p<0.001) as indicated in the figure below. All children displayed more emotional facial expressions for social videos compared to non-social. And, as expected, ASD displayed significantly less facial expressions compared to TD.

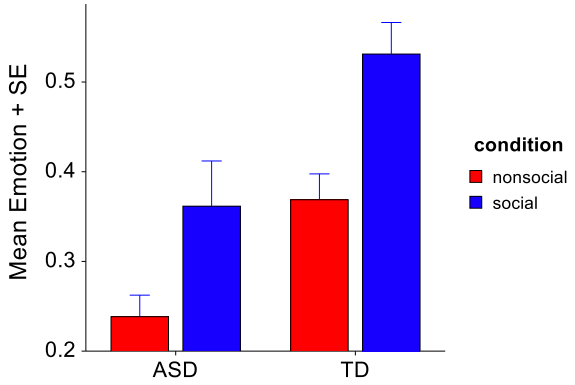

Figure 1: Emotion expression index for ASD vs. TD and Social vs. Non-social video conditions.

Conclusions: This exploratory analysis suggests emotional expression deficits in ASD and specifically related to social context. This could be a contributing factor or causal link in the overall social interaction deficits observed as a hallmark of this condition. For future steps, we will expand our participant pool and employ additional models for face image processing, and emotion classification.

References:

1. Schultz, R.T., et al., Archives of general Psychiatry, 2000. 57(4): p. 331-340.
2. Lepistö, T., et al., Brain research, 2005. 1066(1-2): p. 147-157.
3. Klin, A., et al., Nature, 2009. 459(7244): p. 257.
4. O'riordan, M.A., Autism, 2004. 8(3): p. 229-248.
5. Bonnel, A., et al., Journal of cognitive neuroscience, 2003. 15(2): p. 226-235.
6. Gliga, T., et al. Curr. Biol., 2015. 25(13): p. 1727-1730.
7. Gomot, M., et al., Brain, 2008. 131(9): p. 2479-2488.
8. Mazzoni, A., et al., Social neuroscience, 2018: p. 1-14.
9. Jolly, E., Cheong, J. H., Xie, T., Byrne, S., Kenny, M., & Chang, L. J. (2021). arXiv preprint arXiv:2104.03509.
10. Ekman, P., & Friesen, W. V. (1978). *Environmental Psychology & Nonverbal Behavior*.

Acknowledgements: Funding from PA Dept. of Health CURE.

Extent of Impaired Axons at Varying Degrees of Stretch of Neonatal Brachial Plexus

Virginia Orozco, MS[1], Sanjna Srinivasan[1], Rachel Magee, MS[1], Joy Iaconianni, MS[1], Megan Gorleski[2], Mitali Sahni, MD[3], Sriram Balasubramanian, PhD[1], Anita Singh, PhD[4]

[1]Drexel University, Philadelphia, PA; [2]Widener University, Chester, PA; [3]Sunrise Children's Hospital, Las Vegas, NV; [4]Temple University, Philadelphia, PA

Introduction: Brachial plexus (BP) is an intricate network of nerves responsible for providing motor and sensory innervation to the upper extremities [1]. Neonatal brachial plexus palsy (NBPP) is a common BP injury in infants, described as overstretching of BP during complicated birthing scenarios [2,3]. Despite obstetric care improvements, NBPP has a worldwide incidence of 1-4 per 1000 live births [3, 4]. Surgical intervention remains controversial since timing and type of surgery rely on understanding extent of axon impairment observed after injury [3]. The objective of this study was to characterize structural changes and extent of impairment in axons at varying degrees of stretch of neonatal BP using a neonatal porcine model.

Methods: Seventeen neonatal piglets (3-5 days old) were anesthetized and BP was exposed using an axillary approach per approved procedures by Institutional Animal Care and Use Committee. *Biomechanical Studies*: A custom-built mechanical testing device was used to stretch BP nerves at a rate of 500 mm/min to predetermined low (<10%) and high (>10%) strains. To measure actual strain, black acrylic paint markers were placed along nerve length and a stereo-camera (ZED Mini) was positioned above. Load and displacement data were acquired at a sampling rate of 1000 Hz. Images were captured at 100 frames/s. *Histology*: Three hours post-stretch, BP nerves were harvested and OCT-embedded. Ten-µm-thick serial longitudinal sections were stained with Hematoxylin-Eosin (H&E), neurofilament (NF) and beta amyloid precursor protein (βAPP) immunofluorescence. Using Leica DMI 4000B microscope, stained slides were imaged at 10X along the nerve length. Each image was scored by an independent-blinded observer for vascular and fiber damage using an adaptive scoring system for each. Vascular damage was scored on scale of 0-2 (0-no damage, 1-torn vessel, 2-scattered blood cells). Fiber damage was scored on a scale of 0-4 (0-no to minimal damage, 1-straightening, 2-increased spacing, and 3 and 4-torn to scattered fiber disruption, respectively). Extent of fiber damage was measured at thickest fascicle by binarizing image and measuring 100x100 pixel^2 region of interest. βAPP accumulation was measured as percent area of positive βAPP staining over background.

Results: Using the modified scoring systems, vascular damage (**Fig. 1A**) and fiber damage (**Fig. 1B**) increased with increasing stretch.

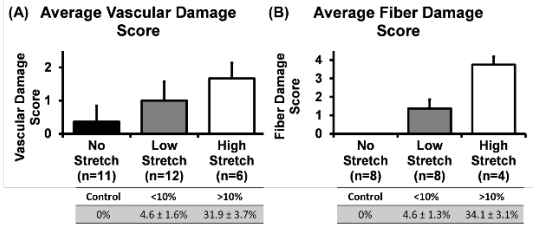

Fig. 1 Bar graphs of average (A) increasing vascular damage, (B) increasing fiber damage, with increasing stretch.

Extent of fiber damage decreased with increasing stretch (**Fig. 2**).

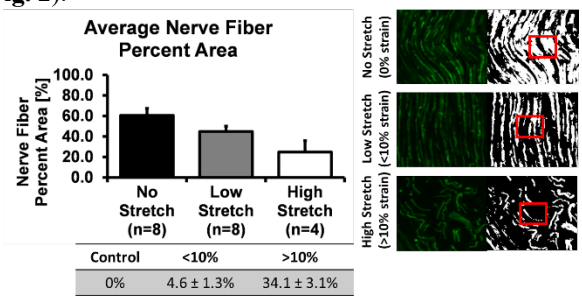

Fig. 2 Bar graphs of average decreasing extent of fiber disruption with increasing stretch with representative images.

βAPP accumulation increased with increasing stretch (**Fig. 3**)

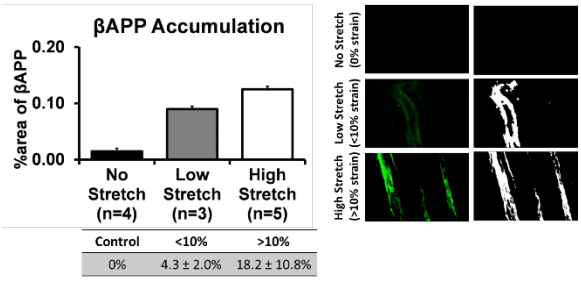

Fig. 3 Bar graphs of average increasing βAPP accumulation with increasing stretch with representative images.

Conclusions: This study is the first to characterize structural changes of neonatal BP with respect to varying degrees of stretch. Understanding extent of structural impairment after stretch may aid the understanding of injury thresholds of NBPP because neonatal piglet and neonatal human BP share anatomical similarities [5]. Future functional studies may further contribute to the understanding of NBPP injury mechanism.

References:

1. Abid A. OTSR. 2016;102:S125-S13.
2. Mehlman CT. J Pediatr Orthop. 2015;589-605.
3. Abzug JM. Orthop. 2010;33:430-435.
4. Johnson EO. Injury. 2013;44:293-298.
5. Hanna AS. J Anat. 2022;240:172-181.

Acknowledgements: This project was supported by the Eunice Kennedy Shriver National Institute of Child Health and Human Development of the National Institutes of Health R15HD093024; R01HD104910-01A1 and NSF CAREER grant Award #1752513.

Computational and *In Vitro* Experimental Analysis of Blood Pump Flow Paths for Pediatric Ventricular Assist Device

Thomas Palazzolo, MS, PhD Candidate[1]; Giselle Matlis, PhD Student[1]; Jordon McGowan[1]; Randy Stevens, MD[2,3]; Amy L. Throckmorton, PhD[1]

Biomedical Engineering[1], College of Medicine[2], St. Christopher's Hospital for Children[3], Drexel University

Introduction: Pediatric heart failure (HF) is a life-threatening disease which leads to over 10,000 hospitalizations and a mortality rate of 7-15% annually.[1] As donor hearts remain scarce, clinicians are increasingly relying on mechanical circulatory support (MCS) devices to sustain patients; however, pediatric MCS devices face hurdles related to children's smaller size and physiological heterogeneity.[1] A limited number of MCS devices are specifically designed for pediatric use, however these have limited operating ranges that make long-term single-device support impractical.[2] Alternatively, adult devices used in children often operate off-design, and this off-design usage correlates to a marked reduction in patient outcomes.[2]

The Drexel BioCirc Research Lab has developed a novel, double-blood pump, magnetically levitated ventricular assist device (VAD), aiming to provide a single-device solution for MCS across the pediatric age range. Previous work has focused on the initial development of axial and centrifugal pump designs intended to provide full support across the pediatric age range; however, the integration of these pumps into a single, compact device housing remains an unresolved challenge. Given the unique geometric constraints of pediatric VAD technologies, thorough analysis of both the pumps and the blood flow paths is necessary to ensure that the device meets design requirements across the pediatric age range. To accomplish this, a two-staged approach was used, combining computational fluid dynamics (CFD) modeling in tandem with experimental testing. By investigating two turbulence models and comparing results to experimental test data, we sought to evaluate device performance and verify a computational model of the device.

Methods: The axial component of the double-blood pump VAD was investigated using both CFD analysis and *in vitro* benchtop testing. Designs were first evaluated in simulation using ANSYS CFX; preliminary analysis indicated the presence of turbulent flow in the pump and flow path. Thus, we employed two turbulence models, K-ε and SST, in accordance with industry standards. The first, the K-ε model, is known to estimate bulk fluid flow patterns, and the SST model leverages K-ε while incorporating additional features to model boundary layer separation. The axial pump was modeled at speeds of 10,000-13,000 RPM for 1-3 L/min, in line with pediatric requirements. During the *in vitro* experiment, pump performance was evaluated using a custom-built test rig, utilizing a drive shaft to turn the axial impeller.

Results: Both K-ε and SST models were constructed to meet standard mesh quality metrics and achieved successful convergence per criteria. Pressure rise was higher in the K-ε simulation results, except at the lowest flow rate of 1 L/min, where SST generates a slightly higher pressure rise. The pump curve slope was steeper with SST, resulting in a more significant reduction in pump performance, as compared to K-ε, over the range of flow rates. This trend was consistent across all modeled pump rotational speeds. A section of the collected data is illustrated in **Figure 1.**

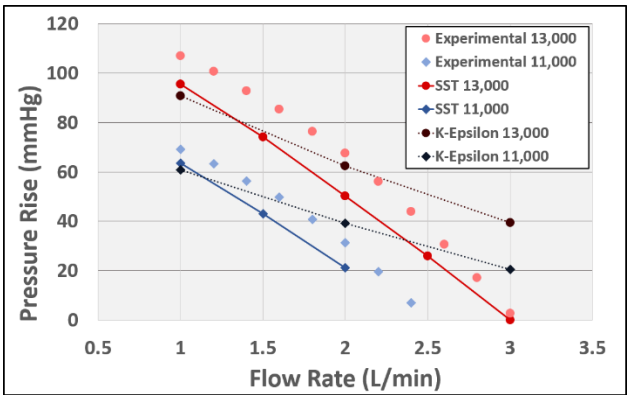

***Figure 1**. Comparison of experimental and CFD data (K-ε and SST turbulence models) at 11,000 and 13,000 RPM.*

The experimental measurements mimicked the trend of the SST predictions. The experimental performance findings for the prototype outperformed SST simulation results by a small margin (5-15 mmHg); this trend was consistent across RPMs and flow rates. However, a much wider deviation was found between the experimental data and the K-ε model predictions for the pressure-flow performance. Thus the experimental results indicate the importance of boundary layer separation and edge effects in the experiment, as the SST simulation incorporates additional features over K- ε to model boundary layer separation.

Conclusions: There was a significant deviation between the K-ε and SST turbulence model predictions, despite identical geometries and operating conditions; this discrepancy was especially large at higher flow rates. Such results imply that boundary layer separation and edge effects have a prominent impact on the performance of the axial pump through the device flow path. Experimental data mimicked the magnitude and trend of the SST model predictions well, and thus this turbulence model will be used in future design iterations.

References:

1. Fox CS. Front. Cardio. 2022; 9:886874
2. Palazzolo TC. Artif. Organs. 2022; 46(8):1475-1490

Acknowledgements: Funding has been provided by the NIH NHLBI R01HL153536 award and Drexel University's "Research and Engineering for Pediatrics by Interdisciplinary Collaboration Leveraging Education and Partnerships for Pediatric Healthcare" (*R-EPIC LEAP for Pediatric*

Healthcare) from the U.S. Department of Education's GAANN Program (Fellow: TP).

Simultaneous Motor and Cognitive Training to Improve Ambulation in Individuals with TBI

Sai Pamula, Oluwaseun Ibironke, BS, Karen J. Nolan, PhD, and Kiran K. Karunakaran, PhD
Kessler Foundation, Center for Mobility and Rehabilitation Engineering, 1199 Pleasant Valley Way, West Orange 07052

Introduction: Traumatic Brain Injury (TBI) is a leading cause of motor disability, resulting in significant gait & balance deficits, and leading to reduced ambulation function[1,2]. Conventional training focuses on cognitive-only or motor-only gait training which results in variable recovery with residual gait & balance deficits as cognitive-only tasks might not activate all brain regions associated with motor tasks, reducing its efficiency[2,3]. As cognitive functions (such as attention, executive & memory) are essential for motor learning and motor function, these domains are tightly interconnected[3,4]. Therefore, therapy that simultaneously targets the motor and cognitive domains by increasing cognitive and motor effort to perform the motor task may lead to improved ambulation recovery. The objective of this study is to show preliminary evidence for the efficacy of 4 weeks of simultaneous motor and cognitive training (MCT), using virtual reality to improve biomechanical, functional, and cognitive outcomes in young adults with TBI.

Methods: Data is presented from two participants with TBI (20.5 ± 0.5 years old, > 6 months post-injury). One 22-year-old healthy control (HC) was used as a reference and participated in one data collection session. Both participants with TBI completed 10 60-minute sessions of MCT using a virtual reality integrated treadmill (C-MILL, Motekforce Link, The Netherlands). C-MILL includes customizable motor & cognitive VR tasks. The tasks target the motor (static & dynamic limb loading and load shifting, reactive balance, gait trajectory, dynamic balance, coordination for speed changes, and lateral balance) and the cognitive (attention & executive function) domain simultaneously. The tasks and therapy progression were customized for each participant based on their deficits and recovery. Data was collected at baseline and at follow-up (after training). Data collection included: 1) Biomechanical Outcomes: Temporal [Total double support time (TDS), single support time (SS), and swing time] and spatial [step length] characteristics measured using the Zeno™ walkway (ProtoKinetics, USA). 2) Cognitive outcomes: trail-making test (TCT) performed by seeing the time taken to connect numbered or lettered circles sequentially. 3) Functional Outcomes: Timed Up and Go (TUG), 10-meter walk speed (10MWT), and 6-minute walk test (6MWT). TUG measures the time taken to stand up from a chair, walk three meters, turn around, and sit back down; 10MWT measures the time taken to walk 10 meters to calculate gait speed. 6MWT measures the distance walked in 6 minutes.

Results: The results from two TBI and 1 HC participants are shown in Figure 1 and 2. At baseline both TBI participants spent longer time in TDS, SS and swing than HC. After 10 sessions of MCT, TDS time reduced with no change in SS, swing, and step length. At baseline (Fig. 1c), TBI 1 couldn't perform TCT (cognitive task) and TBI 2 showed reduced TCT performance compared to HC. After training, both TBIs improved their cognitive performance (reduced time to complete the TCT). They also increased their

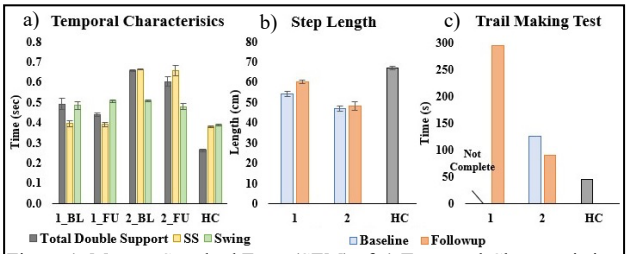

Figure 1: Mean ± Standard Error (SEM) of a) Temporal Characteristics b) Step Length c) Trail Making Test (BL: Baseline, FU: Follow-up)

walking speed (10MWT; Fig.2b), endurance (6MWT; Fig.2c), and gait & balance (TUG; Fig.2a) from baseline to follow-up. The observed change was above the minimal

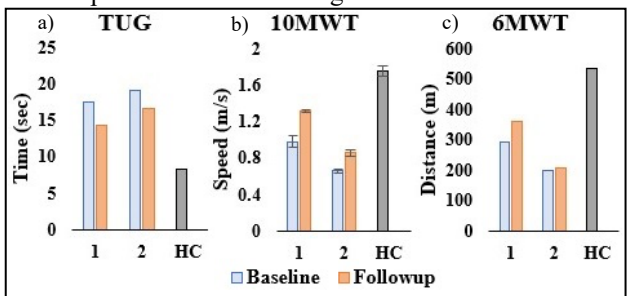

Figure 2: Mean ± SEM of a) TUG b) 10 MWT c) 6 MWT

clinically important differences for all functional metrics.

Discussion and Conclusion: In this study, we evaluated the feasibility of MCT to improve gait & balance in adults with TBI. Training included cognitive integrated motor tasks personalized to each participant based on their deficit and recovery progression. Preliminary results showed a decrease in TDS, indicating reduced time spent in the stance phase, and improved transition between steps, indicating improved gait. The results showed an improvement in cognitive (TCT) outcomes. The observed biomechanical changes could be due to more efficient mapping between cognitive and motor networks. Evidence suggests that cognitive function is positively correlated to physical function, and that cognitive effort contributes to motor recovery, ability of motor control, and performance of activities of daily living (ADLs)[3,4]. The improvement of cognitive and motor function could have contributed to the observed significant functional improvement (improved speed, endurance, and gait & balance function) in gait & balance. These preliminary results show that MCT has the potential to induce recovery of function even during the chronic stages of recovery. The functional impact of an increase in gait, balance, speed, and endurance could improve community ambulation & participation. Though promising, these results require further validation with a larger sample size.

References:

1. NJ Department of Health.
2. Williams, G. et al. Arch. Phys. Med. Rehabil. 2009; 90:587–593
3. Pichierri, G. et al. BMC Geriatrics. 2011; 11
4. Cantin, JF et al. Brain Inj. 2007; 21:327–334

Acknowledgements: Research supported by New Jersey Health Foundation (PC29-21).

Point of Care Detection Device

Rachel Panetta, Rachel Holden, Allison Burton, Jessica Longstreth
Advisors: Dr. Christopher Wagner, Dr. Maulik Shah
The College of New Jersey

1) User Need

In low-resource areas, there is currently no device that provides polymerase chain reaction (PCR) level accuracy testing within point-of-care times. This can be attributed to PCR's need for thermocycling, which requires expensive, bulky equipment and lengthens test time. This Point of Care Detection Device strives to provide field workers with a handheld portable device that supports QUASR-LAMP technology. This proprietary isothermal reaction can amplify and detect genetic material faster than PCR methods[1]. Thus, the device will provide field workers with a method for accurate same-day genetic-based disease testing in low-resource areas.

2) Design Inputs

Critical-to-quality design inputs were identified and justified using customer input and peer-reviewed studies. The requirements and specifications below are critical to the functionality of the device.

- The analyzer shall be capable of controlling the temperature of a reaction chamber. The device must successfully heat the reaction chamber to peak temperature at 55°C-70°C ± 3°C. The device must maintain a ramp rate between 0.5 and 1.0°C/s.
- The analyzer shall detect the presence of specified genetic material through a colorimetric detector. The detector must determine the sample's color intensity.
- The analyzer shall have a maximum test time less than 45 minutes, which aligns with point-of-care devices.
- The device must be at most 28 x 24 x 19 cm, which is within standard dimensions for a handheld device.
- The analyzer will provide users with the ability to enter and run specific metrics.

3) Solution

Decision matrices were used to compare options during the part selection process. The selected parts that fulfill the above requirements are listed below. Figure 1 depicts how they will be implemented into the final device.

- Peltier Heater (Laird Thermal Systems, 4.5 W, 3.7 V)
- Adafruit AS7262 6-Channel Visible Light / Color Sensor Breakout
- Waveshare Barcode Scanner Module
- OBJET VEROBLUE RGD840

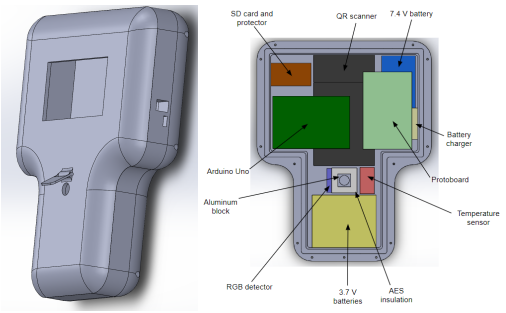

Figure 1: Schematic of final device design.

4) Testing and Verification Results

In order to select heating components, preliminary testing was completed using ANSYS transient thermal analysis. This simulation demonstrated that the design with the specified thermoelectric heater operating at 4.5 W for 70 seconds met the target heating rate and temperature.

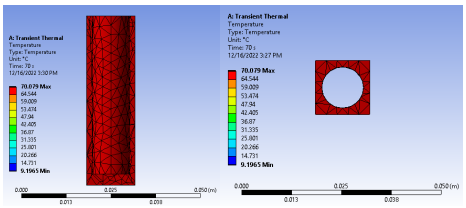

Figure 2: ANSYS Thermal Analysis Simulation

After doing initial testing using the peltier to heat aluminum block, a ramp rate of 1.6 °C/s was determined. However, the block is currently 3.9 x 3.7 x 1.8 cm, which is much larger than what it will be for the final prototype. Further testing will determine final ramp rates once the reaction chamber has been milled to its appropriate size.

Other testing includes:

- The ability of the outer enclosure to withstand biohazard cleaning agents has been verified using the OBJET VEROBLUE RGD840 3D printing material specification sheet.
- The size of the device has been pre-measured using the SOLIDWORKS model to be 28 x 24 x 19 cm.

5) Conclusion

Subassemblies have been constructed for initial verification testing. Final testing, including positive control validation, will run following final assembly. A successful prototype of the device can offer healthcare workers in low-resource settings the ability to conduct quick, accurate point-of-care testing. Reliable diagnostics in these areas may lead to better care than syndromic management alternatives[2].

References:

(1) Bektaş A. et al. Viruses. 2021;12(5):742.
(2)Peeling RW & Mabey D. Clin. Microbiol. Infect. 2010;16(8):1062-1069.

Acknowledgments: We would like to thank The College of New Jersey for funding this project.

Drag-reducing polymers mitigate flow separation of whole blood in a 3D-printed bifurcation

Louis S. Paone[1], Matthew Szkolnicki[1], Brandon J DeOre[1], Kiet A. Tran[1], Allison Andrews[2], Servio Ramirez[2], Peter A. Galie[1]
[1]Department of Biomedical Engineering, Rowan University, Glassboro, NJ, USA
[2]Lewis Katz School of Medicine, Temple University, Philadelphia, PA, USA

Introduction: Hemodynamics have been studied *in vitro* since the 1930s, when Fahraeus used glass capillaries to determine the effect of diameter on hematocrit [1]. In the time since, studies with whole blood have provided insight into a diverse array of physiological processes including coagulation and the development of a cell free layer. Yet, the modalities used in these studies have not progressed much further beyond glass capillaries in mimicking *in vivo* vasculature. Digital light processing (DLP) provides a new avenue to study hemodynamics in topologies that better represent the geometry and the mechanical properties of the vascular bed. Moreover, a recent advance in bioinks compatible with DLP allows the incorporation of spatially controlled covalently bound peptides that mediate cell-ECM interactions[2-4]. One flow phenomenon that has frequently been interrogated *in vitro* includes the effect of drag reducing polymers (DRPs) to mitigate disturbed blood flow. However, these studies have yet to interrogate how the endothelial lining alters the effect DRPs have on dampening secondary flow patterns. Implementation of whole blood flow in complex vascular topologies lined with endothelial cells provides insight into how DRPs mitigate damage in ischemia-reperfusion injuries.

Methods: 3D printed vasculature was fabricated using a LumenX+ digital light processing printer (CellInk). A bifurcation topology was modeled using computer aided design (SolidWorks) iterated with computational fluid dynamics (COMSOL) to fabricate a geometry capable of inducing disturbed flow in one of the daughter branches at flow rates between 1 and 3 mLmin^{-1}. Empirical methods to validate the proposed model included perfusion of human and bovine whole blood spiked with fluorescent bead tracers through the printed bifurcated vessel. Paired with laser micro-particle image velocimetry (μPIV), the trajectory of beads was tracked over three different flow rates; 1, 2, and 3 mLmin^{-1}. To facilitate the perfusion of human whole blood, the bifurcation was decorated with the endothelial cell binding motif, HAVDI (N-Cadherin) using photochemical induced immobilization. 12.5M/mL hCMEC/d3 cells were seeded into the vessel and the gel was rotated 90° every 30 minutes for 3D culture. Vessels were incubated in EGM-2 for 3 days and hooked up to human whole blood and imaged using μPIV.

Results: Velocimetry measurements validate the accuracy of the computational model by indicating that separation occurs above a flow rate of 2 mLmin^{-1} (Fig. 1B). At the lowest PEO concentration tested (10 ppm), both measured and predicted velocity values show considerable overlap, as shown along a radially oriented line at the bifurcation (red dotted line in Fig. 1C). However, at the highest PEO concentration (1000 ppm), the data show less agreement, even when considering the altered shear-thinning properties of the blood at this concentration of the drag-reducing polymer. The discrepancy is most apparent on the near wall of the bifurcation where the model predicts flow separation and a large recirculation zone that is not observed in the experimental measurements (Fig. 1D). Similar to the results in acellular channels with bovine blood, the human blood controlled condition showed strong agreement between the predicted and measured velocity profiles. At 3 mLmin^{-1}, there is a clearly defined recirculation zone due to flow separation at the near wall of the bifurcation (Fig. 1E). However, addition of 1000 ppm PEO results in another discrepancy between the predicted flow profile and the measured velocities, despite accounting for the difference in shear-thinning properties of whole blood containing PEO.

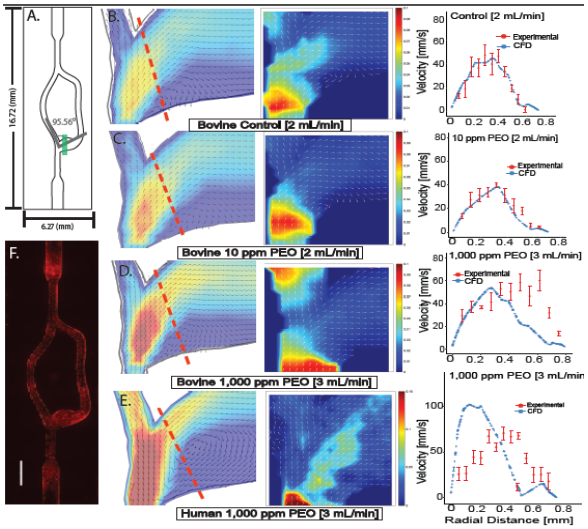

Figure 1: (A) Schematic of modeled bifurcated geometry. CFD velocity profiles, experimental contour maps, and subsequent graphical representation of velocity as a function of radial distance respectively (B-E). Transfected LifeAct P23 hCMEC/d3 cells seeded on HAVDI peptide (F). *Scale Bar 1 mm.

Conclusion: These results establish the utility of mitigating induced turbulent flow of whole blood within 3D printed branched vasculature using DRPs. DLP yields superior scalability for rapid and precise localized topologies that mimic the complexity of *in vivo* vasculature in a controlled environment. The bifurcation geometry presented here, validated by the CFD model, successfully induced flow separation for both bovine and human whole blood beginning at 2 mLmin^{-1}, which is mitigated by the presence of higher concentrations of DRP. Further work is required to delineate the mechanisms by which DRPs attenuate flow separation, since the model was unable to predict this effect.

References:

1. Namgung, B. Clin Hem Microcirc 2015. **61**(3):p.445-57.
2. Barcelona-Estaje, E. Adv Health Mat, 2021.**10**(6)
3. Cruz-Acuna, R. Matrix Biol, 2017. **57-58**: p. 324-333.
4. Vega, S.L. Nat Commun, 2018. **9**(1): p. 614.

Regulation of Fibroblast Mechanosensing under Inflammatory Stimulation by Type V Collagen

N. Patel*[,1], K. L. Spiller[1], L. Han[1]
[1]Drexel University

Introduction: Fibroblasts are highly sensitive to the biomechanical and biochemical cues of residing niche [1]. During wound healing, inflammatory stimuli leads to aberrant collagen remodeling [2], and pro-regenerative stimuli leads to myofibroblast activation, resulting in excessive deposition of collagen I [1, 3]. The fibrotic matrix, in turn, impacts the phenotypic shift of fibroblasts, contributing to a vicious cycle of scar formation [1, 3].Type V collagen, a minor regulatory collagen, plays a key role in regulating collagen I fibril assembly in vivo [4], and thus, could be a central player in this process. Indeed, atrophic scar formation is a prevalent symptom observed in patients with classic Ehlers-Danlos syndrome (cEDS), a connective tissue disorder caused by the mutation of *COL5A1* gene [3]. Understanding the role of collagen V in fibroblast mechanosensing can provide new insights into the cell-matrix cross-talk of fibrosis. This study aims to determine how deficiency of collagen V alters fibroblast response to external inflammatory and mechanical stimuli.

Methods: Adult human Dermal fibroblasts from normal human donors (HDFa) and cEDS patients (JaySen) were obtained from ATCC. Polyacrylamide (PAAm) gels with 2kPa (soft) and 64kPa (stiff) moduli were prepared, following established procedure [5]. After pre-culture in DMEM, cells were seeded on collagen I-coated PAAm gels in a 6-well plate at 50,000 cells/well for 2 days. Cells were then treated with tumor necrosis factor (TNF)-α (20ng/ml) to simulate M1-macrophage-induced proinflammatory response for 7 days, or left untreated as the control. After the culture, we performed immunofluorescence staining for collagen V (AB7046, Abcam), phalloidin for F-actin cytoskeleton (A12379, Thermo Fisher) and DAPI for nuclei (62248, Thermo Fisher).

Results: The reduced collagen V expression in cEDS cells was confirmed by decreased collagen V staining relative to the normal control (Fig. 1a). Also, cEDS cells showed higher cell density and DAPI staining, indicating loss of collagen V may lead to accelerated cell proliferation. On the soft substrate, both groups expressed low amount of F-actin, and we did not notice substantial morphological differences between the normal and cEDS cells (Fig. 1b). However, when seeded on the stiff substrate, cEDS cells adapted a more elongated morphology. In alignment with this morphological change, the F-actin cytoskeleton also became more aligned along the long axis of cEDS cells. The contrast was further aggravated when cells were stimulated with the inflammatory cytokine, TNF-α (Fig. 1b).

Conclusions: This study highlights the important role of collagen V in the inflammatory phase of wound healing. Studies have shown that collagen V regulates the expression of integrins in human cell lines [5]. While we have not elucidated the role of collagen V in integrin expression patterns yet, this study provides direct evidence on the impact of collagen V loss on altered fibroblast mechanotransduction, as shown by changes in F-actin expression (Fig. 1). It is widely known that integrins often serve as direct mechanotransducers and are crucial in regulating downstream biomechanical signals [6]. Our data suggest that despite the low concentration of collagen V in vivo, changes in F-actin dynamics due to the collagen V deficiency may result in the change of types and expression of integrins. This, in turn, would disrupt mechanosensitive pathways that are crucial to tissue homeostasis or pathogenesis, such as YAP/TAZ, Rho/Rock, Notch and Wnt signaling [7, 8]. For example, stimulation with inflammatory cytokines such as TNF-α would further perturb these mechanosensitive pathways, and collagen V could play an important role in mediating the mechano-inflammatory response of fibroblasts, as supported by the altered F-actin dynamics.

Integrating these results with the roles of collagen V in regulating integrin activities, our findings provide a basis to elucidate a new mechanobiological role of collagen V at the cell-fibrous matrix interface under inflammation. This would provide a basis for developing collagen V-based biomaterials to modulate fibroblast immunoresponses and injury-induced fibrosis.

References:

[1] Hannan, R.T., et al., *ACS Biomater Sci Eng*. 4:1223-1232, 2018.
[2] Chou, D.H., et al., *J Immunol*. 156:4354-4362, 1996.
[3] Witherel, C.E., et al., *Biomaterials*. 269:120667, 2021.
[4] Wenstrup, R.J., et al., *J Biol Chem*. 279:53331-7, 2004.
[5] Zoppi, N., et al., *J Biol Chem*. 279:18157-68, 2004.
[6] Ross, T.D., et al., *Curr Opin Cell Biol*. 25:613-8, 2013.
[7] Martino, F., et al., *Front Physiol* 9:2018.
[8] Noguchi, S., et al., *Int J Mol Sci*. 19:3674, 2018.

Acknowledgements: This work was supported by NSF CAREER CMMI-1751898 and the U.S. Department of Education's Graduate Assistance in Areas of National Need (GAANN) program.

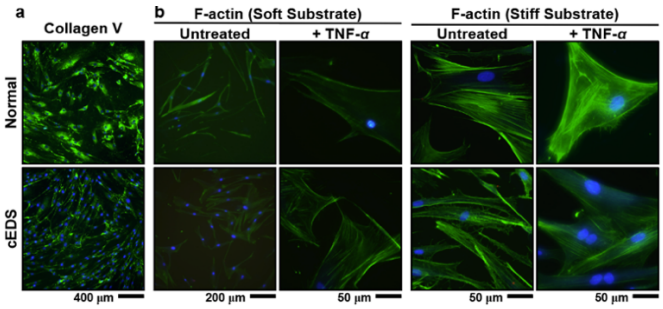

Figure 1. a) Representative collagen V (green) and DAPI (blue) IF staining of normal and cEDS fibroblasts. B) F-actin (green) and DAPI (blue) staining of normal and cEDS fibroblasts seeded on soft, and stiff substrates with or without the treatment of TNF-α for 14 days.

StablEyes: System for Quantifying and Improving Handheld Optical Coherence Tomography

Savan Patel, Ella Atsavapranee, Jake Becker, Ruoming Fan.
University of Pennsylvania, Penn Medicine, Children's Hospital of Philadelphia.

Introduction: Optical coherence tomography (OCT) enables physicians to capture cross-sectional images of the retina to diagnose and track both ocular and nonocular diseases.[1] The market for OCT imaging is significant and projected to expand 15.41% by 2030. Ophthalmologists typically use tabletop OCT, but handheld OCT (H-OCT) is required for infants, children, and patients undergoing surgery, who cannot use the chin mount on the tabletop version. However, physicians raise several concerns that the H-OCT is heavy (~5 lbs.) and difficult to stabilize in the sub-millimeter optimal imaging zone. In current practice, physicians use their fingers to position the H-OCT lens over the patient's eye, reducing reproducibility and accuracy in image acquisition.[2] Ultimately, this requires physicians to keep patients under anesthesia for longer during surgery or skip imaging altogether. As a result, patients can be misdiagnosed, preventing them from getting appropriate treatment. Our objective is to develop a system that makes retinal imaging easier and more reliable.

Methods: The StablEyes system consists of an electronically-controlled stabilizing mount for the H-OCT that enables physicians to collect images in a repeatable and reproducible manner, and a Python-based software program that uses random forest machine learning (ML) ensembles to identify diseased retinas from healthy ones after imaging. Physicians can place the H-OCT in the holder compartment, adjust the vertical position through motorized control

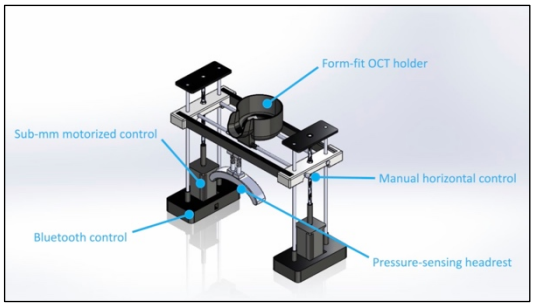

Figure 1. StablEyes stabilizing mount

with sub-millimeter precision, and align the horizontal position manually relative to the patient's eyes. Other features of our device include a pressure sensing headrest to detect and prevent patient discomfort, Bluetooth control to improve ease of use, and automatic adjustment of device settings from the patient's previous visit. We plan to conduct an IRB-approved clinical study in March to validate our device. ML identification models were validated based on reported confusion matrices and R^2 using publicly available training data sets.

Results: Our solution improves upon existing technologies regarding ease of use and software capabilities. The stabilizing mount has successfully achieved the need specifications of *supporting up to 10 lbs., wirelessly controlling motors, implementing pressure sensors to detect patient discomfort and reverse direction of the mount, and measuring the height of the mount*. Furthermore, the imaging mount system's design usability was validated by demonstration to clinician mentors who use the H-OCT in practice. The IRB study to quantitatively show improved imaging quality has been approved and will begin in the coming weeks. The image processing algorithm is a retinal nerve fiber layer identification via Optimized Random Forest Machine Learning. The model achieved an R^2 training dataset value of 0.999 and an R^2 testing dataset value of 0.992, suggesting high accuracy and minimal overfitting. The false positive rate was 0.04%. The false negative rate was 0.75%.

Figure 2. System clinical testing

Conclusions: Providers using our solution are able to conduct H-OCT imaging seamlessly to make important clinical diagnoses, track disease progression, and ultimately improve the patient's vision. StablEyes simplifies the H-OCT imaging process to reduce the amount of time that a patient is under anesthesia for imaging, the number of physicians required for imaging, and misdiagnoses from poor images. To increase our impact, the current working prototype will be iteratively refined for clinical use, including the implementation of printed circuit boards, wireless mechanical control by the image analysis software and UI/UX, and clinically-ready housing for the device. The image analysis algorithm has achieved a high accuracy for identifying features of primary importance in retinal OCT images, and we will train our software with datasets of diseased retina OCT images to improve the robustness and versatility of our platform. We have gained IRB approval with Penn Medicine to conduct a clinical study to validate both the StablEyes system with patients and healthy volunteers. Validation will consist of multiple imaging trials as well as analysis of resulting OCT images using our image analysis software. These data will be rigorously compared to data collected with the current standard practices to inform future steps. We envision that our solution will increase the widespread use of H-OCT imaging to accelerate the research on diagnostic retinal imaging in both ocular and nonocular contexts, which has immense potential to fundamentally change how physicians diagnose diseases.

References:

1. Schlick et al. Int J Mol Sci. 23(22):13683 (2022).
2. Lee et al. Invest Ophth. Vis Sci. 54(13):8152-9 (2013).

Acknowledgements: The authors would like to acknowledge the mentorship of Erin Berlew, PhD; Sevile Mannickarottu; David Meaney, PhD; Tomas Aleman, MD; Drew Scoles, MD; and Sangeeta Vohra, PhD.

Mechanoregulatory Role of Extra Domain A Fibronectin Matrix During Wound Repair

Jennifer Patten, Patrick Halligan, Michael Kegel, Jacob Bonadio, Fatima Ahmed, Shiv Patel, Ghazal Bashiri, Karin Wang
Temple University, Department of Bioengineering

Introduction: Fibronectin (Fn) is a ~500kDa extracellular matrix dimeric glycoprotein with variable structure and signaling sensitive to cell traction and microenvironmental forces. Alternatively spliced Extra Domain A (EDA) Fn is synthesized in response to microenvironmental forces to regulate cell adhesion and fibrillogenesis.[1] EDA Fn is synthesized in the adult in wounds[2] and pathologies, including fibrosis and scleroderma.[3] Yes-associated protein (YAP) is essential for wound healing, [4] is activated by Fn,[5] and contributes to the fibrotic response.[6] However, the mechanoregulatory role and signaling of Fn's EDA region during wound closure remains unclear. Therefore, we seek to characterize wound EDA Fn microarchitecture and investigate if EDA Fn activates YAP.

Methods: The wound assay comprises human dermal fibroblasts cultured on plasma fibronectin-coated polydimethysiloxane substrates with stiffnesses mimicking wounded (18kPa), normal (55kPa), and fibrotic (146kPa) tissue. Test conditions include Irigenin (inhibits binding to EDA-Fn, [7] Millipore Sigma, Darmstadt, Germany), CA3 (YAP inhibitor, [8] CIL56, SelleckChem, Houston, TX), and a dimethylsiloxane (DMSO, FisherScientific, Hanover Park, IL) control. Paraformaldehyde fixed samples were immunostained for EDA-Fn (IST-9, Abcam, Cambridge, UK), f-actin (AlexaFluor 568 Phalloidin, Thermofisher, Waltham, MA), and nuclei (DAPI, ThermoFisher, Waltham, MA); wound sites were imaged with an Olympus Fluoview FV1200 confocal microscope (Olympus Life Sciences, Waltham, MA). Matrix microarchitecture was characterized in ImageJ TWOMBLI.[9] GraphPad-Prism9 calculated one-way ANOVAs and Tukey's multiple comparisons post-hoc analyses.

Results: Initial EDA Fn assembled in the baseline wound assay shows stiffness-dependent alignment (Fig1C) and density (Fig1E) trends, and significant branching to stiffness correlation (Fig1D). Blocking binding to the EDA region of Fn (Irigenin) reverses the initial stiffness driven matrix alignment profile (Fig1H) and increases overall branching (Fig1I). Inhibiting binding to the EDA region of Fn (Irigenin) generates EDA Fn matrices with non-significantly variable density within the first 24 hours. Cells treated with Irigenin assembled EDA Fn matrices in wound sites with thicker fibrils, smaller pores, and increases in branching and density (Fig1F). YAP inhibitor CA3 generates similar EDA Fn matrix effects and trends as blocking of the EDA Fn-cell binding region (Irigenin): smaller porosity, increased branching and density, and similar 24h alignment values (Fig1G-J).

Conclusions: Substrate stiffness alters matrix branching, alignment, and density. Initial substrate driven matrix properties can be altered by inhibition of the EDA Fn-cell binding region (Irigenin) or YAP signaling (CA3). This data suggests tissue stiffness regulates EDA Fn remodeling at the wound site through the EDA Fn specific cell-binding region with a potential downstream effector YAP to modulate cell-matrix remodeling. Currently we are quantifying the YAP nuclear to cytoplasmic ratio in these conditions, indicative of YAP activation, to determine if stiffness (wound, normal, or fibrotic conditions) or inhibition of EDA Fn cell binding activates YAP differentially in our wound model. Our work investigates how tissue stiffness modulates fibronectin mechanotransduction with the end goal to tune fibronectin matrices to alter wound healing from fibrotic repair to tissue regeneration.

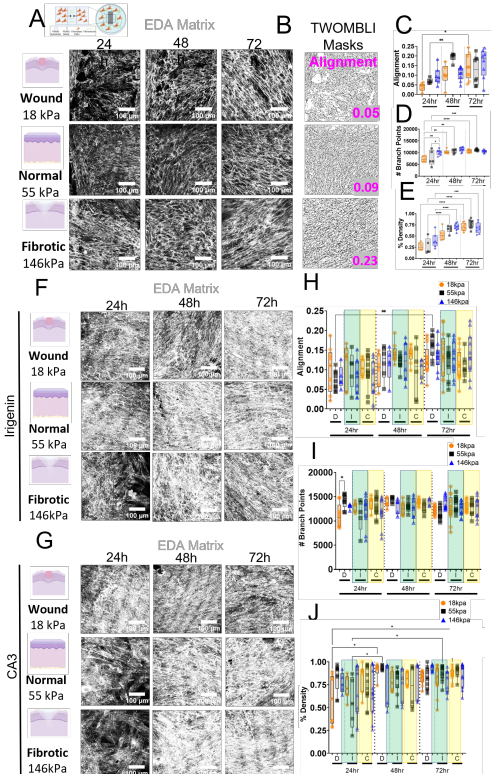

Figure 1. Experimental wound schematic and representative images of baseline (A), Irigenin (F), and CA3 (G) wound assays. TWOMBLI masks (B). Alignment (C,H), branch points (D,I), and density (E,J).

References:

1. Patten, J. Adv Drug Deliv Rev, 2021:170:353-368.
2. Ffrench-Constant, C. J Cell Biol, 1989:109:903-914.
3. Bhattacharyya, S. Scie Transl Med, 2014:232.
4. Lee, M. J Inv Derm, 2014:134:518-525.
5. Dupont, S. Nature, 2011:474:179-184.
6. Elbidwy, A. Devel. 2016:1674.
7. Amin, A. Scie Reports, 2016:6:1-13.
8. Song, S. Mol Cancer Therapeutics, 2018:17:443-454.
9. Wershof, E. Life Scie Alliance, 2021:4:1-11.

Acknowledgements: Temple University Bioengineering Department Startup funds. Shared Temple University departmental resources for equipment usage. Figure schematics created in BioRender.

Identifying Optimal Strut Angle of 3D Printed Scaffolds to Improve Scaffold Efficiency

Evan Peneiras, Rana Ibrahim, Dr. Haoyu Wang, Dr. Hongjun Wang
Center for Healthcare Innovation, Stevens Institute of Technology.

Introduction: Scaffolds play an essential role in tissue engineering, providing the structural support for cells to attach and grow. Scaffold efficiency is defined as the structural support that results in the maximum cell attachment and subsequent tissue growth [1]. By increasing the scaffold efficiency, the time of cell colony formation for tissue regeneration will be reduced. Traditionally, 3D printed scaffolds are designed at 90-degree angles [2]. However, there is little information to support 90-degrees as the most efficient design. This study aims to determine how the overlay angle of filament struts affects the scaffold efficiency.

Methods: Scaffolds with five overlaying angles (30, 45, 60, 75, and 90 degrees) of filament struts were designed and fabricated from 10% (w/v) polycaprolactone (PCL) in hexafluoro-2-propanol (HFIP) solution using the near-field electrostatic prototyping at an optimized volumetric flow rate (0.03 mL/h), voltage potential (1 kV), and tip to collector distance (1mm). The strut diameter and inter-strut spacing were verified by the Nikon SMZ1500 light microscope (4× and 8×) and analyzed using the NIS-Elements BR software. Before cell seeding, each scaffold was sterilized via UV exposure and soaking in IPA for 30 min. HFF-1 fibroblasts (derived from human foreskin) were seeded onto each scaffold at a density of 20,000 cells/scaffold and then cultured in DMEM medium containing 15% FBS and 1% penicillin/streptomycin. After 3-day culture, the structures were fixed in 4% paraformaldehyde and permeabilized with 0.1% Triton X-100 solution. Cell nuclei and F-actin were fluorescently stained using DAPI and FITC-phalloidin. Nikon Eclipse 80i was used to image three selected areas of each scaffold at a magnification of 20×. Finally, ImageJ was used to quantify the cell nuclei count and cell colony area for each image. ANOVA with Tukey post hoc was used to determine statistical significance.

Results: Each printed scaffold was confirmed to be 16mm × 16mm with an inter-filament distance of 300μm and an approximate fiber diameter of 68μm. The 45-degree angled scaffold had an average colony area of $4.01\pm1.05\times10^5$ μm^2 and 25.3±8.1 cell nuclei within that area, significantly greater than other scaffolds ($p<0.05$). The 60-degree angle had an average area of $2.44\pm0.72\times10^5$ μm^2 and 11.7±4.0 cell nuclei, exhibiting the second highest average area and cell nuclei count. The 75-degree angled scaffold had an average area of $1.32\pm0.68\times10^5$ μm^2 and 8.7±5.5 cell nuclei. Furthermore, the 30-degree angled scaffold had an average area of $1.86\pm0.25\times10^5$ μm^2 and 7.3±0.6 nuclei. Interestingly, the standard 90-degree scaffold was the least efficient, with an average $1.02\pm0.54\times10^5$ μm^2 area and 6.0±2.7 nuclei within that area. Clearly, the 45-degree angled scaffold was more efficient than the 90-degree scaffold ($p<0.01$). The other scaffolds are not statistically significant between each other, and there is not enough statistical significance for the cell nuclei count between 90-degree and 60-degree scaffolds.

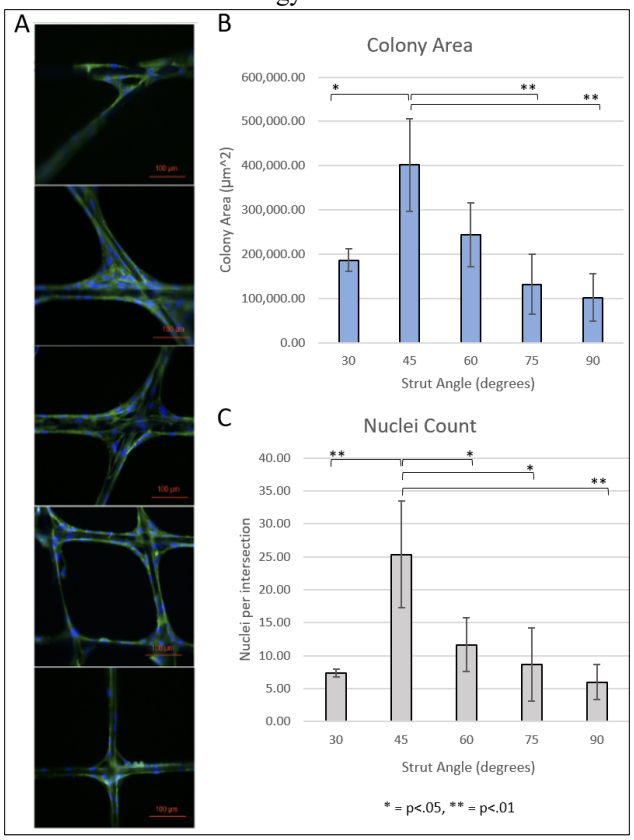

Figure 1. A) Fluorescent microscopic images of scaffold intersection angles; B) The 45-degree scaffold had the largest average colony area; C) 45-degree scaffolds had the highest average nuclei count

Conclusions and Discussion: The angle of tissue-engineered scaffold has an influence on the efficiency of the scaffold. More specifically, 45 degrees is the most efficient scaffold angle to increase both cell attachment and growth, as illustrated by an increase in the colony area and cell nuclei count. Although the scaffolds were composed of two layers of filaments struts via near-field electrostatic prototyping, further testing is required for those 3D printed scaffolds made via conventional 3D printing to ensure the consistency of such an ideal angle. In addition, three locations were photographed of each angle, but increasing the number of locations and number of scaffolds could provide more data sets to improve statistical significance. Instead of opting for the default 90-degree scaffolds, the scaffolds at 45-degree angles showed the highest efficiency. Such findings could provide the guideline to design 3D printed scaffolds for better cell colony formation while simultaneously decreasing the necessary preparation time for tissue-engineering laboratory experiments.

References:

1. Chang B. & Leong K. Eur. Spine J. 2008;17:467-79.
2. Tourlomousis F. et al. Microsyst. Nanoeng. 2019;5:15.

Title of abstract: Characterization of the effect of tPA-to-fibrin interactions on network pore expansion during fibrinolysis

Victoria Percoco[1], Rebecca Risman[1], Valerie Tutwiler[1]
1) Rutgers University, Department of Biomedical Engineering, Piscataway, NJ, USA

Introduction: When a blood vessel is injured, a clot forms to stop bleeding. Once the clot has finished serving its physiological purpose, it must break down through the process of fibrinolysis, the degradation of the structural fibrin network. Fibrin is an insoluble protein which forms when its precursor fibrinogen is cleaved in the coagulation cascade. Tissue plasminogen activator (tPA) initiates the fibrinolytic process when it binds to fibrin, leading to the generation of the plasmin enzyme which cleaves the peptide bonds of fibrin. Impaired fibrinolysis can lead to disproportionate clotting and ultimately heart attack and ischemic stroke (thrombosis) while excessive fibrinolysis can cause bleeding. Though the physiology of fibrinolysis has been studied, the influence of biochemical factors such as fibrinogen concentration on the degradation of the fibrin network is poorly understood.

Methods: Here, confocal microscopy is used to assess the impact of different fibrinogen concentrations on the kinetics and structural dynamics of lysis. A Zeiss 780 confocal microscopy was used to capture human-pooled platelet-poor plasma with varying fibrinogen concentration (starting concentration of 2.9 mg/mL, labeled with Alexa Fluorophore 647) and a fixed concentration of tPA. Images were captured at three regions of the clot. Timelapse images provide information about the pore sizes and appearance of the fibers as they form and break down. FIJI (ImageJ) was used to measure the pore size of every five images to see the growth of pores over time. These images were divided into four regions with a grid, and four pores were measured from each region. The mean and standard deviation of the pore measurements from each image capture were calculated using Prism 9.0.

Results: The time lapses reveal that pores expand in size differently in clots with different fibrinogen concentrations, as observed in figure 1. The clot with 0.23 mg/mL fibrinogen has pores that grow at the same rate, showing that the fibrin fibers of the clot degrade in a homogeneous manner. Figure 1A shows the similarly sized pores that are labeled with arrows. The clot with 0.70 mg/mL fibrinogen has both regions with large pores and regions with small pores as seen in figure 1B. The large pores are labeled with arrows and are surrounded by sections of fibrin network with small pores. The pores grow in a heterogeneous manner as the fibrin fibers degrade throughout the clot. The rate at which the pores grow differs between the regions of the clot as seen in figure 2, which shows the measurements of the pore sizes over time. The pores in regions 3 and 4 grow larger and at faster rates than those in the other two regions.

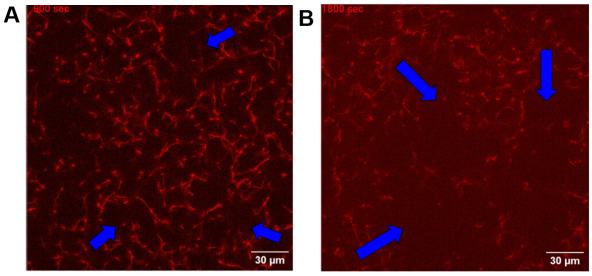

Figure 1. A) Homogenous pores in fibrin clot with 0.23 mg/mL fibrinogen, B) Heterogeneous pores in clot with 0.70 mg/mL fibrinogen.

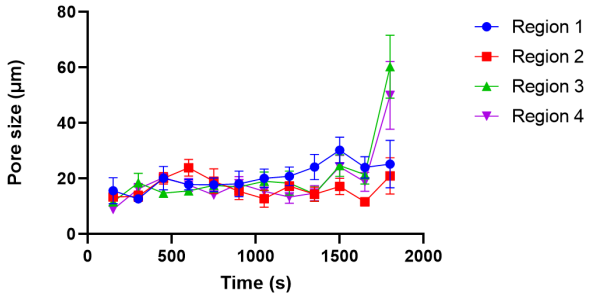

Figure 2. Pore size measurements at four regions of a plasma clot with 0.70 mg/mL of fibrinogen.

Conclusions: Our findings indicate that the pore size of the clot determines the degradation rate and drives fibrinolysis. For the smaller pore sizes that are seen with higher fibrinogen concentrations, a localized tPA lysis front develops and creates a ripple effect as the pore begins to expand in that region. Contrastingly, with larger pore sizes, as seen with lower fibrinogen concentrations, the tPA molecules are able to more readily diffuse through the clot to bind/unbind to new fibers. This behavior creates a more coordinated and homogeneous breakdown of the clot. We propose that smaller pore sizes restrict tPA diffusion as they clump together and only lyse the nearby fibers. Future work includes using labeled tPA to visualize this clumping behavior. This research can help with the development of improved tPA variants for therapeutic purposes including stroke treatment.

References:

1. Bannish BE et al. Sci Rep. 2017;7(1):6914
2. Risman RA et al. Biophys J. 2022; 121(17):3771-3285

Acknowledgements:

NIH R00HL148646-01 (V.T.); New Jersey Commission for Cancer Research COCR22PRF010 (R.R.); NIH T32 GM135141 (R.R.); New Jersey Commission for Spinal Cord Research CSCR23IRG005 (V.T.)

A novel integrative bioinformatics pipeline for high-accuracy structural variant calling

Jonathan Elliot Perdomo [1,2], Mian Umair Ahsan [2], Qian Liu [2], Li Fang [2], and Kai Wang [2].
[1] Drexel University School of Biomedical Engineering, Science and Health Systems [2] Raymond G. Perelman Center for Cellular and Molecular Therapeutics, Children's Hospital of Philadelphia

Introduction: Whole genome sequencing studies have provided us insights into the wide global diversity of human genetic variation and allows us to identify the genetic basis for disease phenotypes. Discovering clinically relevant variants is important for clinical diagnosis, identifying treatment targets, and even predicting treatment response. Structural variants (SVs) (>50bp) are the primary source of human genome variation. Short read sequencers are well-established but lack the read lengths necessary for discovering large, complex SVs. Emerging long read technologies such as the Pacific Biosciences (PacBio) and Oxford Nanopore (ONT) platforms are more effective but are limited by variable base-calling error rates. Optical mapping technologies (e.g. Bionano Genomics) provide a low-resolution genomic map which can be used in conjunction with sequencing reads to improve genome assemblies. These emerging technologies also require novel quality control (QC) tools which can handle large datasets and can provide platform-specific metrics for the raw data prior to analysis. Currently available QC tools typically support only one sequencing platform, or a subset of filetype formats. Finally, in order to resolve the full complexity of SVs, it is clear that future studies will benefit from an integrative approach leveraging information from multiple platforms [1]. Initiatives such as the Pangenome Graph Consortium also aim to extend the current linear reference genome (GRCh38) into a pangenome graph reference structure which would be more representative of global human genomic diversity [2]. Thus, future SV calling tools must provide support for these emerging reference formats. Here I propose a novel bioinformatics pipeline which includes LongReadSum, a high-performance quality control tool providing important metrics for emerging technologies across platforms, as well as initial work on the development of ContextSV, an SV caller which leverages advantages from each technology to identify SVs with high accuracy.

Methods: LongReadSum is a hybrid Python/C++ command line tool which generates an interactive report summarizing read, base, and mapping quality metrics in dynamic HTML. It leverages multi-threading to improve performance for BAM and sequencing summary .txt files. We also provide support for raw signal data from ONT FAST5 files (Fig. 1). The SV calling pipeline will involve *de novo* assembly of long and short reads using the optical map as a scaffolding, followed by alignment to the linear/graph reference genome. Breakpoint sites will be extracted from short read alignments. I will apply a Hidden Markov model (HMM) to identify copy number variant (CNV) SVs from sequencing data, as described in a previous lab paper [3]. I will be using a high-performance approach leveraging split reads and gaps from long read alignments to detect copy-neutral variants such as inversions and translocations. Current available long read SV callers suffer from a high false positive rate due to variable error rates. To improve accuracy, I will train a binary classification model to score candidate SVs and automatically filter false positives. Finally, I will include support for graph reference formats to leverage future developments with the human pangenome.

Results: LongReadSum produces fast and comprehensive QC metrics, producing a full report for a single PromethION flow cell BAM file in ~10 minutes. This tool will be used for QC checks prior to SV calling. CNV calling via the HMM model is currently under development, and initial results will be presented at the conference.

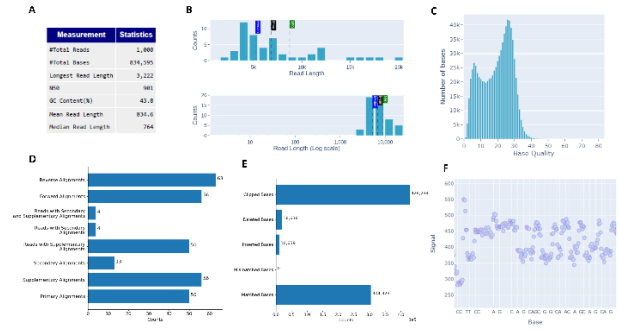

Figure 1. LongReadSum QC report examples. (A) Basic statistics; (B) Read length histogram; (C) Base quality histogram; (D) Read mapping statistics; (E) Base mapping statistics; (F) FAST5 read signal data.

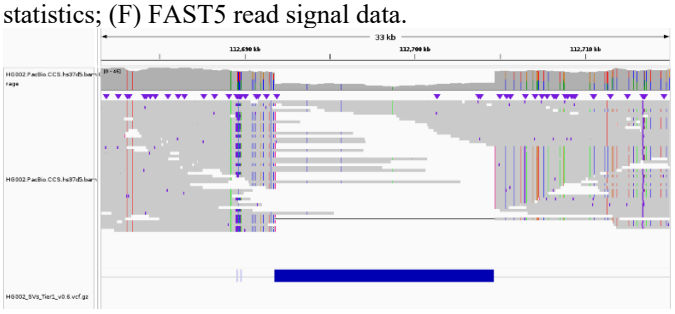

Figure 2. Coverage-based CNV calling. Shown is a large ~13kb deletion (bottom, blue) from the human HG002 sample dataset with a clear decrease in read alignments (middle) and coverage (top).

Conclusions: Here I introduce a novel pipeline for high-accuracy SV calling. LongReadSum provides fast and comprehensive QC metrics across sequencing platforms (available at https://github.com/WGLab/LongReadSum). ContextSV leverages information across platforms and applies a novel scoring model to achieve high-accuracy SV calling.

References:

1. Ho, S.S., A.E. Urban, and R.E. Mills, *Structural variation in the sequencing era.* Nature Reviews Genetics, 2020. **21**(3): p. 171-189.
2. Wang, T., et al., *The Human Pangenome Project: a global resource to map genomic diversity.* Nature, 2022. **604**(7906): p. 437-446.

3. de Araújo Lima, L. and K. Wang, *PennCNV in whole-genome sequencing data.* BMC Bioinformatics, 2017. **18**(11): p. 383.

Plantar Region Foot Ulcer Analysis Device

Anthony Acierto, Zeynep Cakmak, Dominic Patille, Megan Perlman,
Department of Biomedical and Chemical Engineering, Syracuse University

1) User Need:

1.a) Use Case

The Foot Ulcer Analysis Device is made for diabetic patients and their healthcare providers. The task of the device is to detect, document, and monitor any possible diabetic foot ulcers (DFUs) in the plantar region of the foot, as many diabetic patients additionally suffer from neuropathy and may be unable to feel such wounds.

1.b) Problem Impact

In clinical settings, foot ulcer images are captured via smartphone cameras and dimensions are determined with a ruler, often resulting in inconsistent measurements. Furthermore, on average 50% of patients diagnoses for DFUs were delayed over a month due to improper examination and monitoring of the feet.[4] 15% to 25% of diabetic patients will suffer from DFUs and if not realized soon enough and treated, DFUs can lead to amputations.[1,2]

1.c) Scope (Objective)

This device should take accurate ulcer measurements, reproducible photos of the plantar region of the foot, and allow for the storage of photos for ulcer tracking.

2) Design Inputs

2.a) Constraints:

Photos must encompass the entire plantar region of foot beyond the 99th percentile of size (11.90 inches)[3]. The photos must be reproducible; lighting, angles, and distance must remain consistent.

2.b) Requirements:

To capture the full plantar region, the camera is measured at 30 inches from the foot. Thus the photo-light box must be 12”x30”x8”. Additionally there must be a photo-quality, low glare material for the foot to rest on at a 45-degree angle flush to a 8”x8”x6” ankle support. This support is designed to encompass beyond the 99th percentile of ankle diameter (3.2 inches)[3] and direct the foot to the center of the device for reproducible photos.

3) Solution

3.a/b) Design & DEMO

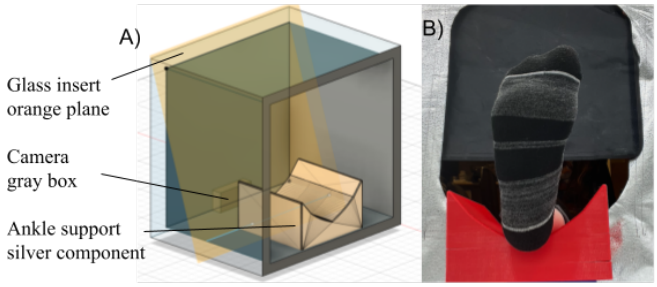

Figure 1: (A) CAD model of the Foot Ulcer Analysis Device. (B) Demonstrated use of the alpha prototype utilizing light box and 3D printed ankle support.

4) Verification Results

4.a) Introduction

In preliminary testing, an alternate light box was used to test design and ease of use of the ankle support qualitatively. Python code to segment the images and perform measurements on ulcers is in development and is being tested with open-source DFU images and compared against true measurements.

4.b) Methods

The plantar region of the patient’s feet will be analyzed through Python code. The images will initially be segmented then thresholded to assist in determining the area of the ulcer as well as the change over time.

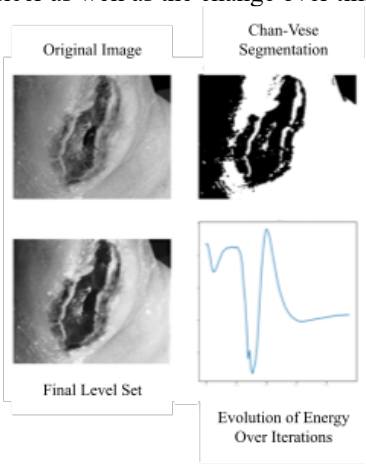

Figure 3: Ulcer image segmentation and thresholding.

4.c) Results

More testing needs to be done to consistently provide accurate DFU measurements, including area and depth. Ease of leg/ankle support has been demonstrated qualitatively by the design team.

5) Conclusion

5.a) Summary:

Images obtained utilizing an alternate light box were consistent and image segmentation in Python was offering correct detection results. Once all materials have been received, further imaging and testing in a clinical setting will provide feedback to finalize our product.

5.b) Revisions:

The Python code is being improved to extract more detailed and accurate measurement information from the images.

5.c) Impact (Future Version):

Our device improves treatment for those suffering from DFUs by both notifying the patient and tracking their wound data reliably and effectively.

References:

[1] Diabetes Care 2014;37(3):651–658
[2] Am Fam Physician. 2002;66(9):1655-1663
[3] Gordon, C. et al. U.S. Army Natick Soldier RD&E. 2012 (51 & 115)
[4] Manu C. et al. 2018;27(3):186-192.

Acknowledgements: We would like to thank Syracuse University for the funding to pursue this project. We would also like to acknowledge our supervisors, Dr. Douglas Yung and Johnson Agyapong, as well as our clients at Upstate University Hospital, Dr. Daniel Tso and Ronald Miller.

Evaluation of spatial resolution and accuracy with various time filters of the time-domain diffuse optical tomography (TD-DOT)

Lara Pinar[1], Andreas H. Hielscher[1], Stephen Hynkeol Kim[1].
[1]Department of Biomedical Engineering, New York University, New York, NY 10010, USA.

1. Introduction:

Due to the advancements of a time-domain system [1-3], time-domain diffuse optical tomography (TD-DOT) has witnessed a revival in recent years. To improve reconstruction quality, various time data types have been explored, which include the full time of flight (ToF) data, gated time data, various moments from the Mellin transform and its combination with the Laplace transform. In theory, the full temporal data gives the highest accuracy to reconstruction but in practical applications, it suffers from being sensitive to noise.

For this reason, parameterized temporal data also called temporal filters is often used as an alternative to the ToF data as demonstrated to be more robust to noise while providing reasonable accuracy with computational efficiency [4-5]. Recently, our group reported the l0-norm-based SENSOR algorithm [6] that achieves 1mm spatial resolution at depth of 6mm within 20 milliseconds by using three parameterized temporal data types – the zero moment E, 1st moment M^1 and exponential feature $L(s)$. In this work, we focus on evaluating the performance of meantime $< t >= M^1/E$ concerning their spatial resolution as applied to absorption targets located at various depths beyond 10 mm within the tissue by using the l_0-norm minimization.

2. Methods:

2.1 Time-domain diffusion equation (TD-DE)

Transient light propagation in a highly scattering medium such as biological tissue can be described by the time-domain diffusion equation. This approach along with appropriate boundary conditions is presented below,

$$\frac{1}{c}\frac{\partial\phi(t,r)}{\partial t} = \nabla\cdot D(r)\nabla\phi(t,r) - (\mu_a+\mu_s)\phi(t,r) + q(t,r) \tag{1}$$

where $\phi(r,t)$ denotes the time-dependent fluence in units of Wcm^{-2}, and $D = (3(\mu_a+\mu_s'))^{-1}$ is the diffusion coefficient where μ_a is the absorption coefficient and μ_s' is the reduced scattering coefficient, c is the speed of light in the medium, and q denotes an internal source of light. Time filter equations can be obtained directly from the Laplace, Mellin or Laplace-Mellin transforms of Eq. (1).

2.2 Image reconstruction depending on asymptotic l_0 regularization

With measurements M and predictions P of parameterized temporal data available at multiple locations on the surface, we reconstruct an optimal map of absorption coefficients as part of the optical properties of the medium by solving the following l_0-norm minimization as:

$$\mu_a^t = arg\min_{\mu_a^t}(\|M-P\|_2^2 + \beta\|\mu_a\|_0) \tag{2}$$

where $\|\mu_a\|_0$ is the l_0-norm that represents the number of non-zero elements in μ_a and β is the regularization parameter that balances the efforts of minimizing the data fit error $\|M-P\|_2^2$ and the l_0-term $\|\mu_a\|_0$ at once. To overcome difficulties with non-convex non-differentiability of (2), we use here the same asymptotic l_0 norm as reported in [6], which achieves a l_0 norm asymptotically from a smooth l_2 norm, as given in the following form:

$$\|x\|_0 \approx \sum_i \frac{x_i^2}{x_i^2+\sigma_s} \tag{3}$$

where x_i is the i-th element of the sparse vector μ_a and σ is the tuning parameter that adjusts a level of sparsity in the solution. By definition, therefore, as the value of σ goes close to zero, $\frac{x_i^2}{x_i^2+\sigma_s} \approx 1$ when $x_i^2 \gg \sigma$ and $\frac{x_i^2}{x_i^2+\sigma_s} \approx 0$ when $x_i^2 \ll \sigma$, whereas as σ increases $\frac{x_i^2}{x_i^2+\sigma_s}$ resembles a smooth l_2-norm function. Given the asymptotic differentiable l_0-norm given by Eq.(3), the sparest solution to Eq. (2) is obtained at a point that minimizes the mismatch $\|M-P\|_2^2$ and the l_0 norm simultaneously.

3. Results:

For the setup, a 10cm x 10cm x 5cm phantom with two 1mm^3 absorption targets was considered. In this experiment, 50 sources and 50 detectors were located on the 10cm x 10cm top surface area.

Fig. 1 shows a comparison between l_0- and l_2-norm results obtained with mean time $< t >$ alone concerning the spatial resolution: Fig. 1a indicates the prediction of spatial resolution made based on the resolution matrix while Fig. 1b presents the actual reconstruction results as a function of the target depth and separation. The results show that spatial resolution of 1mm, 2mm, and 4mm can be achieved at depths of 10mm, 20mm, and 30mm, respectively.

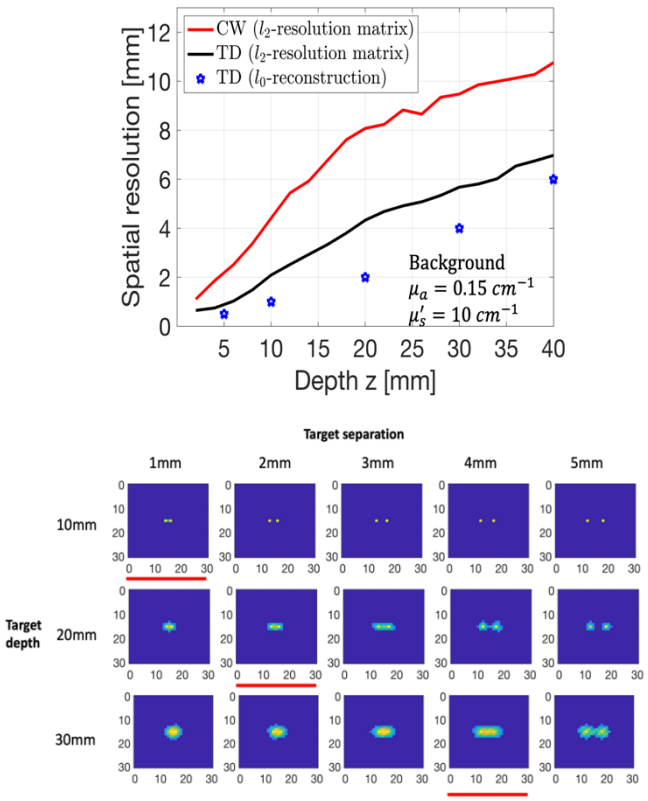

Figure 1. Comparison between l_2 and l_0 norm for continuous wave (CW) and time domain (TD) data in (a) predicted and (b) actual spatial resolution with varying target depth and separation.

4. Conclusions:

The results presented above demonstrate that the image reconstruction generated with l_0-norm-based time filters can achieve a spatial resolution of 1mm – 4mm with varying depths from 10mm to 30mm. Future work involves a thorough assessment of the performance of other time filters available from Laplace transform such as $L(s_1)/L(s_2)$, and $L(s)/E$.

References:

1. Dalla Mora, A.; Contini, D.; Arridge, S.; Martelli, F.; Tosi, A.; Boso, G.; Farina, A.; Durduran, T.; Martinenghi, E.; Torricelli, A.; et al. Towards next-generation time-domain diffuse optics for extreme depth penetration and sensitivity. *Biomed. Opt. Express* 2015, *6*, 1749–1760.
2. Di Sieno, L.; Wabnitz, H.; Pifferi, A.; Mazurenka, M.; Hoshi, Y.; Dalla Mora, A.; Contini, D.; Boso, G.; Becker, W.; Martelli, F.; et al. Characterization of a time-resolved non-contact scanning diffuse optical imaging system exploiting fast-gated single-photon avalanche diode detection. *Rev. Sci. Instrum.* 2016, *87*, 035118.
3. Yoshimoto, K.; Ohmae, E.; Yamashita, D.; Suzuki, H.; Homma, S.; Mimura, T.; Wada, H.; Suzuki, T.; Yoshizawa, N.; Nasu, H.; et al. Development of time-resolved reflectance diffuse optical tomography for breast cancer monitoring. *Proc. Spie* **2017**, *10059*, 100590M.
4. S.R. Arridge and J.C. Schotland, "Optical tomography: forward and inverse problems," Inverse Problems, vol. 25, no. 12, p. 123010 (2009).
5. M. Schweiger, S.R. Arridge, "Direct calculation with a finite-element method of the Laplace transform of the distribution of photon time of flight in tissue," Applied Optics 36, 9042-9049 (1997).
6. H. K. Kim, Y. Zhao, A. Raghuram, A. Veeraraghavan, J. Robinson, & A. H. Hielscher, "Ultrafast and Ultrahigh-Resolution Diffuse Optical Tomography for Brain Imaging with Sensitivity Equation based Noniterative Sparse Optical Reconstruction (SENSOR)," Journal of Quantitative Spectroscopy and Radiative Transfer, 276, [107939]. https://doi.org/10.1016/j.jqsrt.2021.107939 (2021).

Design and Development of a Spatial Eye-Hand Training Coordination Device

Daniella Pino, Nathan Green, Takafumi Asaki, Ph.D., Mary Arico. Ph.D.
Biomedical Engineering, CETA, University of Hartford, CT 06117, U.S.A.

1) User Need:

1.a) Use Case: The end user for this design project is any individual who wishes to improve their spatial eye-hand coordination. It can be applied to patients affected by neuromuscular diseases, such as Cerebral Palsy or Parkinson's disease, which impairs the person's precision of eye-hand coordination in space. However, the design is not limited to clinical use, as it can readily be applied for pro-athletes or student drivers. The user would be instructed to press a target button. If they miss, the device will vibrate.

1.b) Problem Impact: Existing solutions for coordination improvement can be costly and cannot be conducted on the user's own time. Medical costs for parents of children with cerebral palsy can exceed $50,000 per year [1]. In addition, Gentle et al [2] found that individuals with developmental coordination disorder were more likely to fail in driving simulations, which could amplify the vehicular death toll.

1.c) Scope: The goal of this project is to develop a coordination training system to improve the test subject's precision. The design requires basic computer skills, is cost effective, and can be done on the user's own time.

2) Design Inputs

2.a) Constraints: Real-time negative feedback to the test subject is a crucial constraint in this project. Once the user's eye-hand coordination has been quantified, the feedback loop has to act as quickly as possible to ensure the user's score matches the feedback received. If a time lag is present, the feedback could become useless. This limited the software and hardware chosen to implement the design.

2.b) Requirements: Economical accessibility was one of the highest priorities for the design. A major issue with current solutions for eye-hand coordination improvement is that people opt out due to the financial burden [2].

3) Solution

3.a) Design - Intended Use: This device provides a vibrational signal to the test subject to help improve coordination accuracy. Three centered buttons (large red, medium orange, target green) in a LabVIEW program will appear on a touch screen. If the red button is pressed, it signifies that the test subject is significantly far from the target, resulting in a high frequency of vibration whereas the orange button results in intermediate feedback, and the target results in no feedback. Depending on the quadrant pressed, one of four motors would activate. Figure 1 demonstrates this setup.

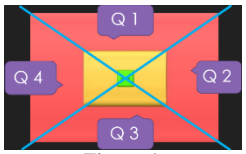

Figure 1

3.b) Build: The system consists of a LabVIEW VI to quantify eye-hand coordination, which is then transmitted wirelessly to a microcontroller that administers feedback via DC haptic motors tethered to the test subject. It was necessary to have LabVIEW communicate which button and quadrant was pressed for the motors to output a vibrational frequency. This was initially done via a data acquisition device (DAQ) connection to Arduino and LoRa wireless communication. This led to issues involving time lag. Because of this, the system block diagram in Figure 2 is currently in development. The system includes a Raspberry Pi, which has Wi-Fi capabilities and can run code in parallel. Both features will solve the issues in the previous design.

4) Verification Results

4.a) Introduction: To implement an eye-hand coordination training system, the architecture within the negative feedback loop needs testing. Continuity testing was performed on the custom designed hardware to ensure proper routing. In addition, a webcam is being implemented for an operator to inform the test subject which direction to move in order to reach the target.

Figure 2

4.b) Methods: To ensure the feedback did not have any broken connections, the continuity test [3] was used on traces within the custom circuit board, shown in figure 3. Next, the connection between the webcam and LabVIEW was established, followed by testing its ability to recognize the subject in 3-dimensional space.


Figure 3

4.c) Results: All 67 connections were designed in accordance with the project's needs. Utilizing IMAQ imaging functionalities within LabVIEW, it was possible to portray the image snapshots on a screen. The color red was successfully extracted shown in figure 4. This will be used to determine the test subject's location.

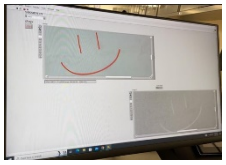
Figure 4

5) Conclusion

5.a) Summary: When a quadrant was pressed on the 2-dimensional screen, the area was identified by pixel coordinates. A motor activated with a frequency depending on the button pressed, to deliver feedback to the test subject. Currently in the works include shifting to 3-dimensional aspects including a webcam as an additional negative feedback mechanism. With various feedback loops and repetition, the subject can improve their coordination.

5.b) Revisions: By including a webcam, an additional feedback mechanism can help improve hand-arm coordination results. In addition, due to issues associated with Arduino and LoRa wireless communication, Python and Raspberry Pi are in the works of being implemented.

5.c) Impact (Future Version): Upon completion of the revisions, the subject would have vision and sensation feedback mechanisms to improve spatial coordination. Providing a less expensive way will help individuals become more independent and reduce human error. This device can provide a more affordable way for individuals with muscle impairments to improve 3-dimensional coordination.

References:

1. Cerebral Palsy Guide, "Cerebral palsy care…" 2023.
2. Gentle J. "Driving skills of individuals…" 2021.
3. McDonald. "Using electrical continuity…" 2016.

Cerebral Hemodynamics Measured by Diffuse Correlation and Near-Infrared Spectroscopy for Monitoring Depth of Anesthesia

Mert Deniz Polat[1], Kurtulus Izzetoglu[1], Patricia A. Shewokis[1,2], Meltem Izzetoglu[3], Shadi Malaeb[4]
[1]School of Biomedical Engineering, Science and Health Systems, Drexel University
[2]College of Nursing and Health Professions, Drexel University, Philadelphia, PA 19102, USA
[3]Department of Electrical and Computer Engineering, Villanova University
[4]Department of Pediatrics, St. Christopher's Hospital for Children, Drexel University College of Medicine

Introduction: Monitoring depth of anesthesia during surgery is critical. Near Infrared Spectroscopy (NIRS) measures of cerebral blood volume (CBV) and cerebral oxygenation (OXY) have been used for monitoring anesthesia [1]. In addition to cerebral hemodynamics, cerebral blood flow (CBF) measures can provide reliable assessment of different anesthetic states and enhance depth of anesthesia monitoring. CBF can be measured noninvasively via Diffuse Correlation Spectroscopy (DCS). This preliminary animal study aims to investigate whether CBF changes correlate with different phases of anesthesia, i.e., maintenance (deep) versus emergence (light) states of general anesthesia.

Methods: The animal experiment protocol followed applicable guidelines for care and use of animals and was approved by the Institutional Animal Care and Use Committee at Drexel University. Newborn Yorkshire piglets (3-6, days old; 2-3 kg) were ventilated at normal oxygen and administered inhalational anesthetics Isoflurane and/or Nitrous Oxide, and intravenous Ketamine. Maintenance state is defined as the period corresponding to the peak-effect of the drug based on pharmacokinetics, with the animal being immobile and nonresponsive to pain, and emergence state as the period after washout of the drug based on pharmacokinetics, with the animal either responsive to pain or mobile. Monitoring included: Continuous recording of vital signs; amplitude-integrated surface electroencephalography (aEEG, Natus CFM 6000); NIRS; and DCS systems. The DCS probe was placed on the preorbital to temporal regions of the piglet head, connected to a continuous 785nm wavelength laser, and a single photon counting module collecting backscattered photons at 2.25 cm distance. Temporal autocorrelation functions of measured light intensity fluctuations are fit over a correlation diffusion model to calculate Blood Flow Index (BFI; cm2/s) [2].

Results: This pilot study reports four epochs of both anesthesia states from two piglets. Fig. 1 shows a representative measure of CBF, CBV, OXY and aEEG during maintenance and emergence states of anesthesia in a piglet after Ketamine (IV). Fig. 2 displays the changes in heart rate, CBF, CBV and aEEG from maintenance to emergence states of anesthesia for the 4 epochs, separately. The results show an increase in CBF, CBV, and HR during the emergence from deep to light anesthesia. The response in surface aEEG was delayed compared to the other modalities.

Conclusions: Increase in CBF and CBV measures from deep anesthesia to light in piglets were consistent across all anesthetic drugs administered. The changes in CBF and CBV preceded those observed by surface aEEG. This observation is in agreement with the neurovascular coupling between CBF and neuronal activity in the reticular activating system and other deep regions of the brain, where increased neuronal activity in subcortical areas, which has been shown to precede cortical emergence, during transitioning from deep to light anesthesia leads to rise in CBF and CBV [3]. These preliminary results posit that the use of DCS along with NIRS for monitoring depth of anesthesia can help predict and prevent unintended emergence into a lighter state of anesthesia during a maintenance phase.

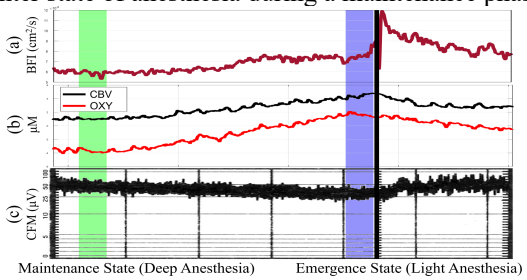

Figure 1. (a) CBF (BFI) collected with DCS, (b) CBV and OXY collected with NIRS, (c) CFM collected with surface aEEG measures vs time. Deep and light anesthesia windows are shaded with green and blue respectively. Marker following blue window annotates animal responding to pain , necessitating another dose of anesthetic agent.

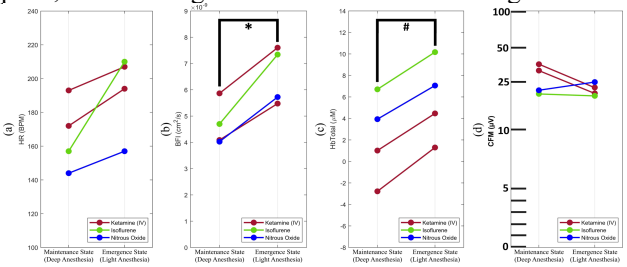

Figure 2. Changes in (a) HR, (b) CBF measured with DCS (BFI), (c) CBV measured with NIRS and (d) CFM measured with aEEG from deep to light anesthesia. (*: $p<0.01$, $t(3)=-6.91$, #: $p<0.01$, $t(3)=-17.81$, Paired t-test)

References:

1. Hernandez-Meza G. J Clin Monit Comput. 2018;32(1):147–163.
2. Diaz D. J Biomed Opt. 2017;22(2):25003
3. Nir T. J Br. J. Anaesth. 2022;128(1):65-76

Acknowledgements: The project was funded, in part, under a Commonwealth Universal Research Enhancement (CURE) grant from the Pennsylvania Department of Health. This work was supported, in part, by The Office of the Assistant Secretary of Defense for Health Affairs through the Combat Readiness – Medical Research Program, under award number W81XWH-20-1-0899. Opinions, interpretations, conclusions, and recommendations are those of the authors and are not necessarily endorsed by the Department of Defense or the U.S. Government. The authors would like to thank to Randolph Sinahon, Danielle Shoshany, Juan Du and Dr.

Sinan Tuzer for their invaluable support in data collection and experimental assistance.

A conductive ink for high-throughput biochemical analysis in microfluidic devices

Ayda Pourmostafa[1], Anant Bhusal[2], Niranjan H. Menon[3], Sagnik Basuray[3], Amir K. Miri[1]
[1] Biofabrication Lab, Department of Biomedical Engineering, New Jersey Institute of Technology, Newark, NJ
[2] Department of Mechanical Engineering, Rowan University, Glassboro, NJ
[3] Department of Chemical and Materials Engineering, New Jersey Institute of Technology, Newark, NJ

Introduction: Recent research efforts have incorporated electrodes into microfluidic platforms to monitor biochemical properties and cells' activities. The electrodes can be used for DNA analysis, cell sorting, material processing, and separation-based detection protocols. The current electrodes require manual processing and multi-step preparation; thus, we need integrated electrodes to continuously monitor biochemical processes. 3D printing can be used to integrate conductive materials into microfluidic platforms. Among different materials, PEDOT:PSS was selected for our light-assisted 3D-printed microfluidic design here due to its stability and biocompatibility for electric stimulations [1].

Methods: We used a multi-material bioprinter that can create high-resolution hydrogel constructs and optimized the parameters for the ink formulation (for example, an intensity of 0.5 W/cm^2) [2]. To make a conductive ink, we used particles of poly (3,4-ethylenedioxythiophene)-polystyrene sulfonate (PEDOT:PSS, 3.0-4.0% in H2O, high-conductivity grade, Sigma-Aldrich, MO) doped into polyethylene glycol diacrylate (PEGDA). The printability and mechanical properties of the ink formulation have been tested for a selected range of PEDOT:PSS mass concentrations: 0, 0.5, 1, 3, and 5% w/v in PEGDA (30% v/v). We characterized the ink using standard compression testing and other physical methods. The conductivity of the ink was measured using the four-probe method in different concentrations of conductive particles from 0.5 to 5% (w/v) in the hydrogel ink. Hydrogel matrix with and without human tumor cells (HT-1080, ATCC) underwent impedance analysis using a 4294A precision impedance analyzer over a frequency range of 1kHz to 1MHz at an applied voltage of 100mV with 8-point averaging.

Results: Our observations showed that in low PEDOT:PSS concentrations, the crosslinking occurs outside of the projected area, and in higher concentrations, it is similar to the circular morphology. The brightfield imaging demonstrated that PEDOT:PSS particle is distributed homogeneously throughout the sample (see **Figure 1**). This is a key requirement for optical absorbance during our manufacturing process. The standard mechanical testing showed an increase in the concentration of PEDOT:PSS led to a decrease in the stiffness of the hydrogel construct. The minimum and maximum elastic moduli recorded were 1700 ± 300 kPa and 5530 ± 250 kPa, respectively. The swelling ratio remained unchanged until 3% w/v PEDOT:PSS concentration but increased at 5% w/v, while a stronger crosslinking resulted in a lower swelling ratio due to lower porosity and solvent absorption. Our conductivity data (not shown here) indicated the lowest value at 0.5% w/v PEDOT:PSS and the highest at 5% PEDOT:PSS, with no predictable change in conductivity when varying the number of layers in the light-assisted 3D printing process. Electrochemical impedance spectroscopy was finally performed to measure charges transfer resistance (R2) in the GelMA system bioreactor. The results showed that R2 increased linearly with an increased cell density (data not shown).

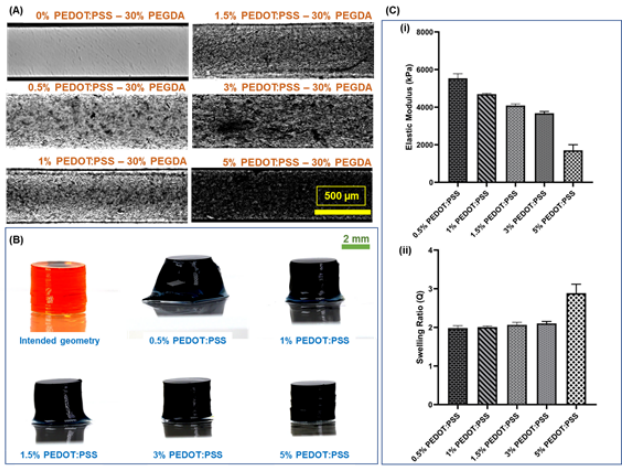

Figure 1. Physical characterization of the proposed conductive ink: A) Brightfield microscopy imaging showing microstructural homogeneity in different groups; B) Pictures of different concentrations of PEDOT:PSS in a lab setting; C) Elastic modulus and swelling ratio of the selected groups.

Conclusions: We tested a novel electro-conductive ink to 3D print electrodes within a hydrogel-based microfluidic device to expand the device's potential by integrating the biochemical analyses within the 3D printed microfluidic devices [3]. It enables the fabrication of cell-laden multi-material microfluidic devices that can be used for screening various chemical agents and drugs. We optimized the printability of conductive hydrogel at various PEDOT:PSS concentrations. The concentration of conductive particles affects UV penetration depth and cross-linking. Increasing the particle concentration affects the mechanical properties of the 3D printed structure, decreasing the elastic modulus in a higher than 5% w/v concentration. This can be related to the light blocking at higher particle concentrations, limiting the formation of stronger bonds within PEGDA chains. This is a study to address the current challenges of 3D printable conductive systems, enabling printing of electrodes and bioreactors in a single continuous process. Future studies will be indicated to apply electrochemical base microfluidics for drug screening applications [3].

References:

1. H.Yuk, B. et al. Nat commun. 2020;1-8.
2. Bhusal, A. et al Biofabrication. (2021); *14*(1).
3. Bhusal, A. et al ACS Applied Biomat. (2021); *5*: 4480-4492.

Impact of Positive Ventilation on Chest Compression Rhythm during Neonatal Resuscitation

Prashant Purohit, John LaCourse
University of New Hampshire, Durham, NH

Introduction

Neonatal Resuscitation (NR) is a method to establish a cardiac rhythm in neonates under asphyxia. In this study, data was collected in real-time from experienced practitioners in NR performing chest compression (CC) without and with positive ventilation on a manikin according to guidelines provided by American Heart Association which is three compressions to one ventilation. Real-time feedback (1) and simulation training (2-4) are achieving motivation as methods to improve NR.

Methods

To record the CC rhythm, accelerometers were mounted on a neonate SimNewB manikin from Laerdal, one accelerometer was mounted on the chest, and the second accelerometer was mounted on the back. An Ambu Bag was used for positive ventilation with force sensing resistors (FSR) mounted for maximum thumb-finger contact. The accelerometers and FSR data were recorded and analyzed using MATLAB and Visual Studio in real-time. Practitioners performed CC on the manikin with and without positive ventilation for approximately 4 minutes each to collect 800 sample values. The Institutional Review Board for the Protection of Human Subjects in Research approved this research (FY2022-410).

Results

The CC rhythm of five practitioners is shown in Figure 1: the four positive peaks and a flat line after the fourth positive peak. The four positive peaks (upward) are when the chest recoils, and the flat line is when the chest is not in recoil or compression. The information of interest is the lack of uniformity in the application of force resulting in different peak values (downward traces) of CC.

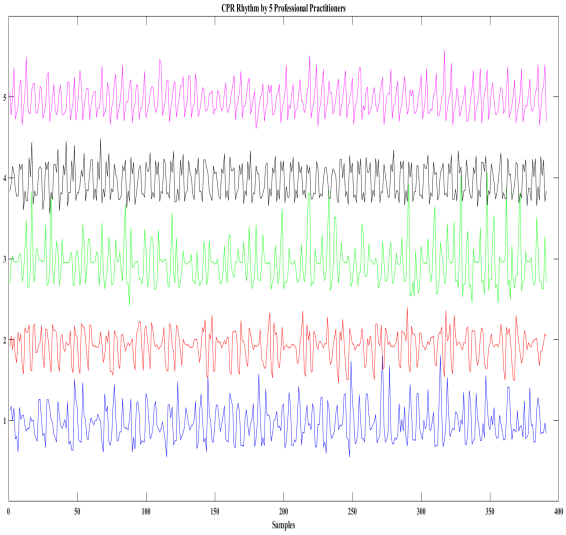

Figure 1. Real-time plots of chest compression and recoil (without positive ventilation).

Figure 2 compares one of the experts CC rhythms without and with positive ventilation. Notice the inclusion of positive ventilation improved the CC rhythm becoming more uniform. When CC was performed without ventilation (red plot), the flat line representing no compression duration is not understandable and not uniform. However, when positive ventilation was introduced (blue plot), the no-compression duration became uniform. The FSR (black plot) shows a flat line during three compressions and a negative peak during positive ventilation.. The positive ventilation works as feedback for experienced practitioners.

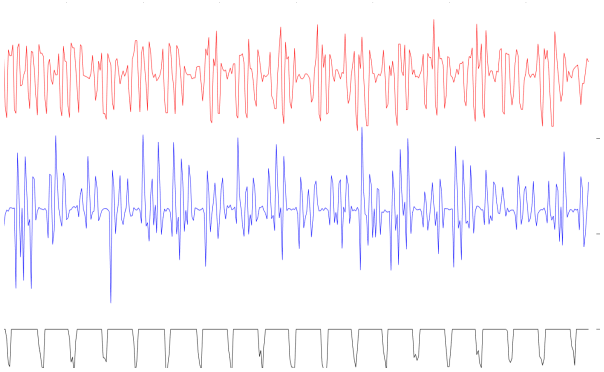

Figure 2. CC rhythm comparison without and with ventilation with FSR data

Conclusions

Chest compression rhythm of experienced practitioners without positive ventilation demonstrated the lack of uniformity in the CC rhythm. The chest compression rhythm improved when professional domain experts did CC with positive ventilation. Chest compression rhythm is vital in delivering NR with compression depth, force, and recoil. It is recommended that real-time visual feedback with positive ventilation be used as a training tool to optimize the delivery of NR.

References

1. P. Martin , P. Theobald , A. Kemp, S. Maguire, I. Maconochie and M. Jones, "Real-time feedback can improve infant manikin cardiopulmonary resuscitation by up to 79%—A randomised controlled trial," Resuscitation , pp. 1125-1130, 2013.
2. A. A. Garvey and E. M. Dempsey , "Simulation in Neonatal Resuscitation," Frontiers in Pediatrics, vol. 8, 2020.
3. N. Alalhareth and M. Howarth, "The Effectiveness of Simulation Training on Nursing Students' Neonatal Resuscitation Skills: A Systematic Review," International Journal of Nursing and Health Care Research, vol. 3, 2020.
4. f. E. S. Abusaad and G. G. Soliman, "The changes on knowledge, confidence and skills accuracy of nursing students at a simulated based setting versus traditional during

neonatal resuscitation," International journal of Nursing Didactics, vol. 5, 2015.

Biomechanics, Energetics and Structural Basis of Rupture of Fibrin Networks

Ranjini K. Ramanujam[1], Farkhad Maksudov[2], Rustem I. Litvinov[3], Chandrasekaran Nagaswami[3], John W. Weisel[3], Valeri Barsegov[2], Valerie Tutwiler[1]

[1]Department of Biomedical Engineering, Rutgers, The State University of New Jersey; [2]Department of Chemistry, University of Massachusetts – Lowell; [3]Department of Cell and Developmental Biology, University of Pennsylvania

Introduction: Fibrin is a self-assembling, viscoelastic polymeric biomaterial that provides mechanical and structural stability to blood clots (thrombi). Fibrin is formed by the thrombin-catalyzed proteolysis of fibrinogen, a soluble protein precursor, which circulates in the blood plasma at a normal concentration of 2-4 g/l1. Fibrinogen levels that are <1 g/l decreases mechanical stability of weak blood clots, resulting in compromised hemostasis. On the other hand, >5 g/l fibrinogen levels in blood are associated with inflammatory diseases and thrombotic complications, such as ischemic stroke and venous thromboembolisms1. A fatal complication of thrombosis is embolization, which occurs when a portion of the thrombus ruptures and becomes lodged in the blood vessels downstream, obstructing blood supply. While most of mechanical studies are focused on fibrin's viscoelastic properties, the factors and conditions affecting the rupture resistance of fibrin has not been explored2,3. Here, we investigate the influence of fibrin(ogen) concentration on the microstructural and mechanical resistance to rupture.

Methods: To make plasma clots with different fibrinogen concentrations plasma pooled from 25 human donors was utilized. The baseline fibrinogen concentration was 2.7 g/l. 1 g/l clots were prepared by diluting the plasma with fibrinogen depleted plasma and a 44 g/l purified fibrinogen solution was used to spike the concentration of clots to 5 g/l. Single edge notch fracture tests were performed to examine fibrin rupture under a constant strain rate (Fig.1A) to determine the mechanical properties. Confocal and scanning electron microscopy was used to quantify the fibrin network structure. A theoretical fluctuating spring (FS) model was used to probe the relationship between fibrin(ogen) concentration and rupture resistance of fibrin clots.

Results: Our results revealed that increasing fibrin(ogen) concentrations resulted in increase in rupture resistance (127 to 365 J/m3) measured as area under the stress-strain curve (Fig.1B). The network structure became denser (0.98 to 12.2 fiber pixels/total voxel (%) ($p<0.0001$)) with thicker fibers (0.14 to 0.3 µm ($p<0.0001$)) with increasing fibrin(ogen) concentrations (Fig. 1C-D). The presence of a crack resulted in a reduction in maximum force that can be withstood, regardless of fibrin(ogen) concentrations. At low (1 g/l) and normal (2.7 g/l) fibrinogen concentrations, we observed that fibrin fibers straighten first (regime I) and then stretch (regime II) shown by the constant slope of stress-strain curve. In contrast, at higher fibrinogen concentration (5 g/l), the fiber straightening and stretching occur simultaneously shown by increase in slope of stress-strain curve (Fig.1B). The results obtained demonstrate that changes in fibrin structure due to varying fibrinogen concentration drastically alter clot mechanical stability. While in the uncracked network, fibrin fibers are stretched evenly (which results in equal mechanical load sharing), in the cracked network fibers around the crack tip deform to a greater extent (unequal load sharing). This further points to the importance of studying the structure and mechanics of fibrin networks formed at different fibrin(ogen) concentrations to better understand the risk factors and biomechanical mechanisms of bleeding or thrombotic embolization.

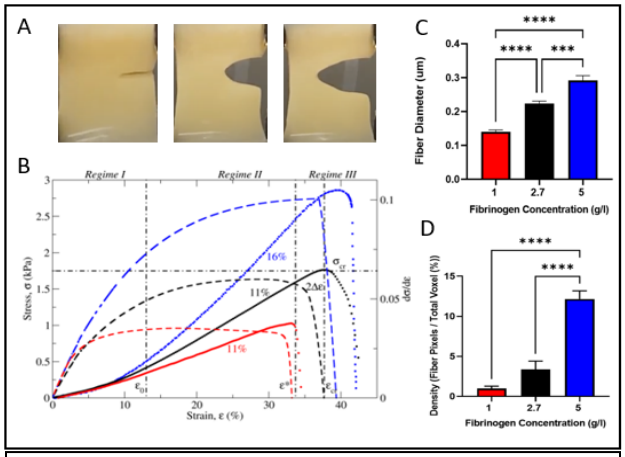

Figure 1: (A) Crack propagation in fibrin clots subject to uniaxial tension at constant strain rate; (B) Stress-strain curves and their corresponding slopes of 1, 2.7 and 5 g/l clots; Fiber diameter (C) and Fiber density (D) as a function of fibrinogen concentration.

Conclusions: Fibrin is a naturally occurring biomaterial that holds significant promise for wound healing in addition to its pathophysiological significance. Surgery and trauma treatments use fibrin sealants, which have fibrinogen concentrations up to 100 g/L. In this work, we coupled experimental and theoretical approaches to address the question of how changes in fibrin(ogen) concentration in the (patho)physiological 1-5 g/l range affects rupture resistance of fibrin networks. The results obtained demonstrate that changes in fibrin structure due to varying fibrin(ogen) concentration drastically alter clot mechanical stability and that the mechanisms of rupture of uncracked and cracked fibrin networks are different. Our theoretical framework can be applied to other protein networks to understand rupture of biological materials. In addition, further fibrin-based studies can help to reveal how the fibrin(ogen) concentration as well as structural architecture of the fibrin network influences the resistance to rupture.

References:1. Rui Vilar, Haematologica 2020;105(2):284-296; 2. Litvinov RI, Matrix Biol. 2017 Jul;60-61:110-123.3. Tutwiler V, Acta Biomater. 2021 Sep 1;131:355-369.

Acknowledgements: This work was supported by the NIH grant R01HL148227 (V.B. and J.W.W), R01-HL135254 (J.W.W.), R00HL148646 (V.T.)

Optimizing Cellular Metabolism to Improve Chronic Skin Wound Healing

Luis Ramirez Agudelo, Gabriel Yarmush, Ph.D., Suneel Kumar, Ph.D., Francois Berthiaume, Ph.D.
Department of Biomedical Engineering, Rutgers University

Introduction: Despite many advances, chronic skin wound healing remains a large problem in terms of costs and morbidity, with over 6.5 million patients afflicted by these conditions yearly. A large amount of information has previously been accumulated about the metabolism of cells in the human body, and this project seeks to use computational modeling to probe that knowledge to uncover which metabolites might be the most promising for improving the metabolism of wound cells, and therefore the natural wound healing process. In particular, this project targets keratinocytes, the cells of the epidermis, and makes use of the Recon database, a public database that seeks to aggregate all of the reactions in the human body.

Methods: For the computational portion of the project a 2014 paper by Quek et al. that outlined a process for reducing the totality of the reactions in the Recon database to one that more adequately models wound cells was used[1]. Metabolic Flux Analysis (MFA) was subsequently used to assess the effects of changes in any of 25 measured metabolites that were provided to the model. The 25 measured metabolites were exchange reactions for every amino acid except cysteine, the exchange reactions for glucose, lactate, and ammonia, and the oxygen uptake reaction. To carry out the process of identifying which metabolites could lead to improvements in chronic skin wound healing, the criteria of improvements in ATP production and biomass production were used. ATP production and biomass were used as markers of cell migration (an energy intensive process) and cellular proliferation, respectively. Monte Carlo simulations were then performed in which inputs were randomly varied around Quek's average values assuming a normal distribution with standard deviation equal to 10%, were carried out. First, a value at which the model achieved reproducible results was established. Sensitivity analysis was then performed, and the same simulation was used to assess which metabolites were associated with the highest ATP production and biomass production. In particular, the 20 simulations associated with the highest production of ATP and biomass were explored to determine which metabolites saw the largest percent and absolute changes under conditions in which oxygen was either varied, held constant at normal levels, or held constant at low levels.

Once the computational work was finished, and the most promising metabolites identified, in-vitro work was undertaken to test the predictions. For this work, HaCaT cells were used. First, a proliferation assay using alamarBlue reagent was carried out in which cells were seeded at 5 thousand per well in a 96-well plate. For the first 24 hour the cells were grown in base medium, at 24 hours the conditions of either valine, glycine, glutamine, and the combination of both glycine and glutamine were added, and at either 48 or 72 hours 10% alamarBlue reagent was added. A scratch assay was also used as a cellular model of a wound. For this, a monolayer of cells was grown to confluency over 2 days, and subsequently scratched with a 200-microliter pipette tip. After the scratch, the same conditions as in the proliferation assay were added. The results were then imaged at hour 0 and every six hours afterward.

Results: First, 1098 simulation was determined to be a sufficient number to achieve reproducible results and was subsequently used in all computational work. Second, by analyzing the results for the uptake of metabolites under those conditions in which ATP production and biomass production was the highest, it was significantly seen that glycine was the largest percent increase under both normoxic and hypoxic simulation conditions. Under all conditions the percent difference in glycine uptake in the 20 simulations with the highest ATP/biomass production compared with the average for all 1098 simulations was over 100%. Meanwhile, although the percent difference was smaller for glutamine, it was the only other extracellular metabolite to exhibit positive percent change in those simulations that had the highest ATP/biomass production in constant oxygen and low oxygen conditions (those that resemble chronic skin wounds the most). The amino acids glycine and glutamine were therefore the ones chosen for further exploration in in-vitro work.

The proliferation assay showed a significantly higher normalized cell number for glycine compared to both basal media and valine (an amino acid not expected to have any effect) at 24 hours, and compared to basal media at 72 hours. The scratch assay also showed a significantly higher percentage of wound closure normalized for initial wound size compared to all other conditions at 6 and 12 hours as depicted in figure 1.

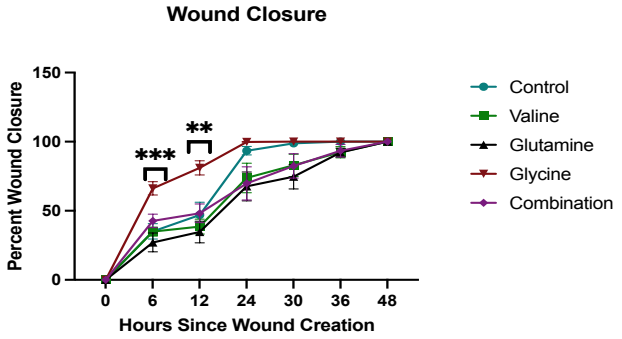

Figure 1. Results for scratch assay over 48 hours, *** indicates significance at the p<.005, while ** indicates significance at the p<.01

Conclusions: Computational probing of a metabolic model of skin wound cells pinpointed glycine and glutamine as the most promising interventions to lead to improvements in the wound healing process. Further in-vitro work validated the predictions in a proliferation assay and scratch assay for glycine, which was predicted as the most likely to have an effect. These findings have identified an intervention that could lead to improvements in wound healing and would therefore merit further exploration in-vivo.

References:

1. Quek L. J. Biotechnol. 2014;184:172-178.

Ultramobile multimodal wearable sensors for investigating the impact of nature indoors and outdoors

Kevin L. Ramirez Chavez[1], Adrian Curtin[1], Yigit Topoglu[1], Saqer Alshehri[1], Michael Woodburn[1], Lynelle Martin[1], Rajneesh Suri[2,3] and Hasan Ayaz[1,3,4,5,6]

[1] School of Biomedical Engineering, Science and Health Systems, Drexel University, Philadelphia, PA, USA
[2] Lebow College of Business, Drexel University, Philadelphia, PA, 19104, USA
[3] Drexel Solutions Institute, Drexel University, Philadelphia, PA, USA
[4] Department of Psychological and Brain Sciences, College of Arts and Sciences, Drexel University, Philadelphia, PA, USA
[5] Department of Family and Community Health, University of Pennsylvania, Philadelphia, PA, USA
[6] Center for Injury Research and Prevention, Children's Hospital of Philadelphia, Philadelphia, PA, USA

Introduction: Psycho-physiological stress has been advocated as the primary means by which urban environments impact individual physiology and well-being [1]. Presently, 55% of the world's population lives in urban areas and this number is expected to increase to 68% by the year 2050 [2]. Accordingly, spending time in visually pleasant environments can help reduce stress and improve mood by promoting parasympathetic activity. Attention Restoration Theory (ART) proposes that directed attention can be modeled as a muscle, wherein the sustained attentional demands of urban environments or prolonged focus on work-related tasks result in significant mental fatigue which requires rest to recover from [3]. Studies have shown that mental fatigue from prolonged directed attention is also accompanied by an accumulation of physiological and mental stressors that negatively affect the individual [1]. The field of neuroergonomics promotes the idea that the environment profoundly shapes the nature of cognition and accordingly, cognitive processes should be studied "in the wild", under realistic contexts which closely match the systems being studied [4-5]. Thus, the ability to study the brain and physiological activity in context is especially important in studies of environmental reception where environmental context is the defining feature. In addition, neuroergonomics highlights the need for the integration of wearable neuroimaging with non-invasive physiological monitoring to provide multi-modal neural and peripheral physiological activity [4]. Early neuroimaging works often have taken the view that peripheral physiological responses to stimulation represent purely nuisance signals which should be filtered to better understand the specific cortical response without assessing the relationships between physiology and the brain. However, physiological response offers unique insights into the underlying brain states and greatly assists in state-related classification [6-7]. In this work, we outline a comparative protocol for studying the environmental effects of nature using mobile neuroimaging and non-invasive physiological monitoring.

Methods: To study the role of different environments on brain and body measures, participants were asked to perform an environmentally mindful presence task in several locations located throughout a local botanical garden (Longwood Gardens, Kennett Square, PA). These multiple environmental locations represent different forms of natural beauty and built-environment settings (Office, Italian Water Garden, Indoor Gardens, Outdoor Meadow Garden, Outdoor Forest Walk). Participants were guided through the different environments in counter-balanced order. In each environment, the participant was asked to freely observe the environment during which the participant's prefrontal cortex will be monitored using a mobile fNIRS system (fNIR Devices 1100). In addition, participant heart-rate variability (HRV) was assessed via wrist-based integrated optical heart-rate monitoring (OHRM) and electrodermal activity (EDA) responses will be monitored using a mobile actigraph (Empatica E4). Following the 5-minute exposure tasks, participants were surveyed on their perceptual responses to the environment including the Perceived Restorative Scale (PRS) [8] as well as scales related to the experience of the environment and aesthetic qualities.

Results: In this preliminary analysis, changes in heart rate and HRV will be assessed in addition to prefrontal measures from fNIRS and autonomic activity via EDA to tie together the relationships between mental state and physiological responses. Responses to environmental stimuli are expected to be sensitive to participants' self-reported measures of restorativeness via the PRS.

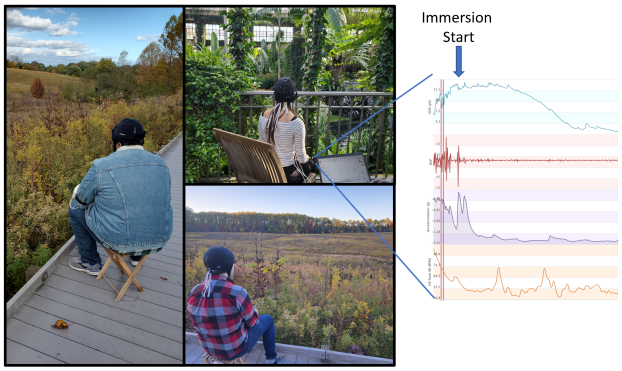

Figure 1. Nature Immersion Task under different environments and example peripheral physiological response

Conclusions: This protocol offers a real-world insight on the neural and peripheral physiological effects of nature immersion as well as a window into the mechanisms behind its asserted restorative potential. It proposes one means of investigating the inter-relationship of psychological, neural, and peripheral responses to nature immersion with an eye towards understanding how these may be beneficial to society at large.

References:

1. Ulrich R. et al. J. Environ. Psychol. 1991;11:201-230.
2. World Urbanization Prospects: The 2018 Revis. 2019.
3. Kaplan, S. J. Environ. Psychol. 1995;15:169–182.
4. Curtin and Ayaz. Jpn. Psychol. Res. 2018;60:374–386.
5. Dehais F. et al. Front. Neuroergonomics 1. 2020.
6. Liu Y. et al. Front. Hum. Neurosci. 11. 2017.
7. Mark J.et al.Adv.Intell.Syst.Comput.2018;586:83–94.
8. Pasini et al. Soc. Behav. Sci. 2014;159:293–297.

Acknowledgements: The authors would like to acknowledge Longwood Gardens and Drexel Solutions Institute for facilitating the study.

Piezoelectric Plate Sensor For SARS-CoV-2 Detection In 30 Minutes Without Gene Isolation and Amplification

Pawan Rao [a], Donald Hall [b], Garth Ehrlich [b], Wei-Heng Shih [c], Wan Y. Shih [a]
[a] School of Biomedical Engineering, Science and health Systems, Drexel University, Philadelphia, PA-19104, USA
[b] Department of Microbiology and Immunology, Drexel University College of Medicine, Philadelphia, PA-19104, USA.
[c] Department of Materials Science and Engineering, Drexel University, Philadelphia, PA-19104, USA

Introduction: Severe acute respiratory syndrome coronavirus-2 (SARS-CoV-2) is responsible for the current Covid-19 pandemic. As of February 2023, so far it has caused more than 679 million cases and 6.7 million deaths worldwide. Although several effective vaccines were developed by the end of 2020 new variants of the virus continue to emerge and each new variant proves more transmittable than the one it has replaced due to several key mutations in the S-protein. Even people who are fully vaccinated or were infected with Covid-19 before could still get infected. The only way to contain the spread of the virus is by rapid and accurate testing on the onset of infection as antiviral medication are effective only if the disease is treated early. Current diagnostic tests to detect the presence of the virus with high sensitivity is PCR. However, PCR is a laboratory test as it requires gene isolation and amplification, expensive equipment, and highly trained personnel. It typically takes 1 day or longer to get the results back. Although at home rapid antigen tests can detect SARS-coV-2 and provide result in 15 min they cannot detect the virus in samples with a viral load 10^4 viruses/ml or lower, thus could miss the early stage of an infection. Several studies have investigated using innovative techniques such as CRISPR, Raman spectroscopy and electrochemical impedance spectroscopy to develop potential rapid, low-cost, and relatively sensitive covid-19 tests. The major limitation of these techniques is that they are not as sensitive and specific as PCR. Moreover, they require complex RNA purification steps and expensive equipment which cannot be miniaturized or field deployable.

Piezoelectric plate sensor (PEPS) as shown in figure 1a is a highly sensitive biosensor developed in our lab. It has remarkable sensitivity in that it can detect DNA in-situ with PCR-like sensitivity and specificity without the need for DNA isolation or amplification. What is unique about PEPS is that its detection Δf is inherently enhanced more than 1000 times by the unique property of the patented piezoelectric layer due to the stress induced upon binding. Previously PEPS exhibited an unprecedented 150 CFU/ml sensitivity for *in situ* DNA detection of bacteria directly from patient stool.

Methods: The goal of this study is to develop a SARS-CoV-2 genetic test assay directly from patient samples in 30 min without gene isolation and amplification. To detect the viral RNA a 28-nt amine-functionalized probe DNA 5'-GTTCCATCTCTAATTGAGGTTGAACCTC-3' to target a highly conserved *orf1ab* gene such that it can specifically detect all variants. Furthermore, this probe was blasted against several respiratory pathogens and human genes using NCBI BLAST to ensure the probe only perfectly match the targeted SARS-CoV-2 gene. The detection temperature was set at 58˚C to ensure only SARS-CoV-2 RNA can bond to the probe on the PEPS. Specific detect of the viral RNA directly from samples was carried out in a temperature controlled flow system where samples with 15 vol% sodium dodecyl sulfate and 3 vol% bovine serum albumin were loaded in a reservoir kept at 95°C to lyse the virus and denature the viral RNA for 10 min, and flow to the detection cell kept at 58 ˚C where a PEPS with probes immobilized on its surface is situated at the center of the flow to catch and detect the viral RNA in the flow.

Results: Figure 1a shows the comparison of the total frequency shift after 30 min detection between synthetic RNA and viral particles at different concentration. There was a downshift of around 700Hz & 1.8kHz for 10^2 and 10^4 cp/ml concentration. Figure 1b shows relative frequency downshift vs time during detection for patient sample with a concentration ranging from 10^2-10^6 cp/ml. There was no frequency downshift when the sample concentration was 0 cp/ml.

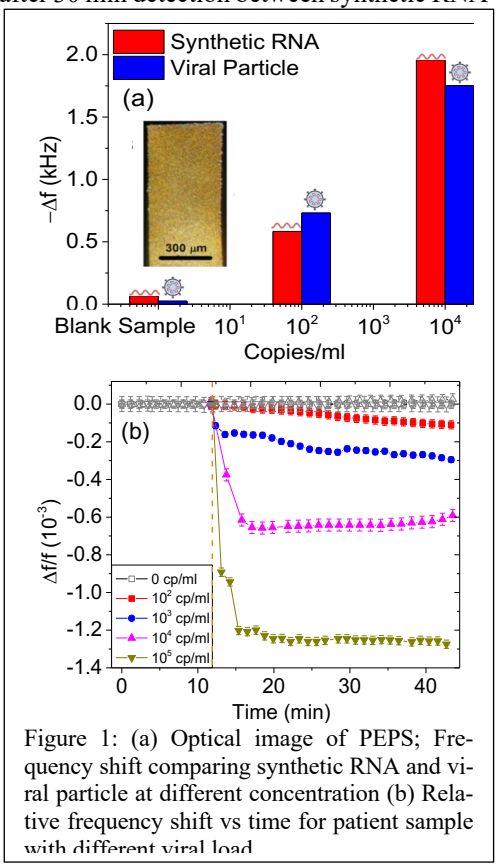

Figure 1: (a) Optical image of PEPS; Frequency shift comparing synthetic RNA and viral particle at different concentration (b) Relative frequency shift vs time for patient sample with different viral load

Conclusions: In this study, PEPS was used to detect SARS-CoV-2 viral RNA directly from patient sample with gene isolation, amplification, and RNA reverse transcription. Effective viral particle lysing was confirmed by comparable detection Δf values of the same concentrations. Testing of 15 covid-19 patient samples and comparison with PCR indicates PEPS had a 100 cp/ml sensitivity in direct detection of viral RNA from patient swaps in 30 min.

Acknowledgements: This work was supported in part by the NIH Grant #. 1R43AI152716-01.

References: 1. https://www.cdc.gov/. 2. Alafeef, M ACS nano, 2020. **14**(12): p. 17028-17045. 3. Han, S. Biosensors and Bioelectronics, 130, 73-80.

Head Tracking Performance of the HoloLens2 During Rehabilitative Games: a Pilot Study

Neethan Ratnakumar, Lorenzo Zurzolo, Rachel F. Jones, Sergei Adamovich, Xianlian Zhou.
New Jersey Institute of Technology.

Introduction: The incorporation of augmented reality (AR) into physical therapy has the potential to transform mundane therapeutic rehabilitation exercises into immersive motivational experiences. Several studies have demonstrated the effectiveness of AR rehabilitation in balance, gait and upper limb strength building [1]. The HoloLens2 is a state-of-the-art AR head mounted display (HMD) developed and marketed by Microsoft. It is equipped with an inertial measurement unit (IMU) and four tracking cameras that enable head tracking. Head tracking can provide valuable information regarding a patient's ability to maintain balance post-stroke or after a traumatic brain injury and can be used in rehabilitative games to provide balance feedback during gait or in other activities. However, the position tracking ability of HoloLens has not been widely tested and its accuracy in tracking specific types of motion is largely unknown. Several studies attempted to quantify HoloLens1's tracking errors. For examples, Yang et al. reported the highest deviation from ground truth at 13.38 cm, observed during rotating the head quickly [2]; Guinet et al. reported maximal errors as high as 25 cm during walking [3]. In this study, we investigate the suitability of the HoloLens2 as a balance assessment tool through head tracking during rehabilitative AR games post neurological injury, by comparing HMD exported tracking data with optical motion capture and state-of-the-art (IMU) system based head tracking results.

Methods: The accuracy of the HMD in head tracking was tested at two different movement ranges: 1) continuously walking in a loop (approx. dimensions 4.85 m X 3.5 m) three times and 2) playing a shelf stacking game that was specifically designed for the purpose of post neurological injury balance and upper limb rehabilitation. Two young healthy male subjects (with a height of 169 cm and 178 cm, respectively) with prior experience of AR usage were affixed with four infrared reflective markers on the HMD and 17 IMUs (Xsens Technologies, Netherlands) on the whole body and participated in the two different data collection sessions. Figure 1(a) illustrates the sensor placements for both sessions. The HMD was simultaneously triggered for data recording with the Xsens and a marker-based optical motion capture system (OptiTrack/Motive). The shelf stacking game involves a subject picking up virtual bricks one-by-one from various locations nearby with both arms and placing them into highlighted areas of a virtual shelf while standing on the same spot. The game necessitates a specific level of extension/stretching and hand-eye coordination, thereby providing balance training. The optical motion capture system tracks the HMD as a rigid body and records its centroid position. The Xsens system tracks the position of the head segment based on a subject-specific whole body biomechanical model and data from all 17 sensors. The HMD tracks the head based on data from its onboard IMU and camera sensors. Due to differences in default coordinate systems of these three systems, we first aligned the data with an Iterative Closest Point (ICP) algorithm. For the vertical position movement, which is much smaller than the horizontal movement, we treated it separately and eliminated its absolute difference with a de-meaning method. The root mean squared errors (RMSE) of the HMD tracked head position was calculated against both marker based and Xsens based results, which were also compared with each other.

Results: The interquartile range for vertical head movement during the game and walking were respectively 0.0212 and 0.0239 m. The averaged vertical position RMSE values obtained for the walking and shelf game trials are presented in Figure 1(b). The horizontal (X, Y) RMSEs observed for the walking trials after ICP for 'HMD vs Motive', 'HMD vs Xsens' and 'Xsens vs Motive' were respectively (0.085 m, 0.081 m), (0.117 m, 0.107 m) and (0.073 m, 0.095 m).

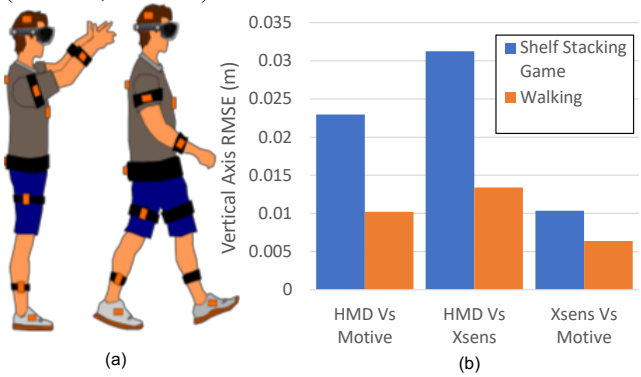

Figure 1. (a) Illustration of the sensor configuration (orange: Xsens sensor; white dot: marker). (b) Vertical head tracking RMSEs between three approaches.

Conclusions: The HoloLens2 HMD head tracking accuracy was observed to be higher in walking compared to the short-range shelf stacking game movements. Even though, the overall HMD head trajectory pattern was in good agreement with the optical and inertial motion capture systems, the results suggest that the change in position is overestimated by the device for activities involving short horizontal range. It is unclear whether the high error of the HMD is related to particular movement types or the speed of movement. These findings indicate that the HoloLens2 HMD could be used as a potential tool for immersive AR rehabilitation with head tracking based balance feedback. In addition, the Xsens measurements were in remarkably good agreement with optical motion capture, suggesting that inertial measurement systems could be a promising alternative for tracking head position in field conditions. Further studies at different speeds and a wider range of activities are required to reach a decisive conclusion on the accuracy of the HoloLens2 for head tracking applications in rehabilitative games.

References:

1. Maria J. V. G et al. JMIR SG. 2021;09 :04
2. Yang L. et al. IEEE MultiMedia. 2018;25:04 (8-18).
3. Guinet A. L. et al. CMBBE. 2020;22 (S169-S171)

Using neural and physiological signals from wearable sensors to evaluate computer-mediated communications

Jeremy Ray, Jan Watson, Jesse Mark, Yigit Topoglu, Rajneesh Suri, Hasan Ayaz
Drexel University, Philadelphia, PA 19104, USA

Introduction: Geographically dispersed workforces can benefit from efficiencies gained from improved knowledge transfer. The recent shift toward hybrid work has presented computer-mediated communications as an important medium for knowledge transfer. The overall goal of this study is to understand factors impacting the efficacy of computer-mediated communications using neural and physiological signals during realistic business scenarios and immersive real-world tasks. This study specifically aims to explore the impact of video bandwidth, information content complexity, and distractions on knowledge transfer performance, with cognitive and affective state assessment of participants with a neuroergonomic approach [1].

Methods: Thirty-three adult volunteers (aged 39.84 years, 15 females) were paid to participate in this study. Participants were seated in front of a computer and watched a series of sixteen 60-second audio/video clips of basic DNA and fingerprint evidence collection methods used for online training by law enforcement agencies. Task conditions were bandwidth (high/low), content (easy/hard), and distractions (with/without), each with 2 repetitions. During the entire session, their prefrontal cortex brain activity was monitored with a functional near-infrared spectroscopy (fNIRS) ultra-thin flat sensor, heart rate (HR) with a wrist-based optical heart rate monitoring (OHRM) sensor, and electrodermal activity (EDA) measured using finger-based electrodes, with battery-operated, wireless, and wearable hardware. For the fNIRS processing, raw light intensity data were low pass filtered with a cut-off frequency of 0.1 Hz to attenuate high-frequency noise and SMAR coefficient of variation-based statistical filter for motion artifacts, and finally, hemoglobin concentration changes for each optode were calculated using the MBLL and were averaged across time for each conversation block. For EDA, skin conductance was measured using a wireless finger-based EDA sensor in micro-Siemens at a frequency of 127.97 Hz. It included two probes attached using rubber-coated wires and two finger connectors, placed on two fingers on the left hand. For the EDA signal processing, time-synchronized blocks for each of the 16 video blocks were processed. Average skin conductance response (SCR) for the video block was extracted, with baseline correction. For the wrist-based OHRM, an optical heart rate monitor was used to record the HR rate of each subject. Based on the event markers, we took the average HR and delta HR for each video condition block. For each modality, linear mixed models were used for statistical analysis with fixed factors of bandwidth, content complexity, distraction, and up to 3-way interactions, and subject as the random effect, with covariates including age and gender.

Results. Analysis of the fNIRS HbO activity shows that there is a significant interaction between content and bandwidth with covariates, Figure 1, top left. For easy content, changes in bandwidth did not significantly impact mental effort, but for hard content, low bandwidth requires more mental effort ($F_{(1,403.7)}$=12.03, p<.001).

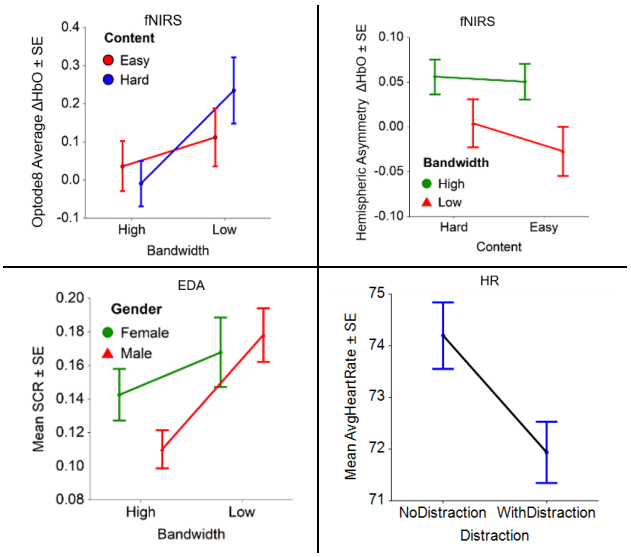

Figure 1. Impact of task conditions. Clockwise from top left: mental effort (fNIRS HbO), emotional valence (fNIRS hemi), emotional arousal (avg HR), and (SCR)

For the fNIRS prefrontal hemispheric asymmetry (emotional valence), when bandwidth is low, valence is more negative ($F_{(1,488)}$=7.8, p<.05), Figure 1, top right. When bandwidth is high, valence is more positive. Average HR is lower when distractions are present ($F_{(1,485.1)}$=5.6, p<.05), Figure 1, bottom right. Overall SCR is higher when bandwidth is low ($F_{(1,460)}$=7.92, p<.05), Figure 1, bottom left. Male SCR is higher than females when bandwidth is low.

Conclusions: This study demonstrated the use of biomedical signals in the neuro-bio-behavioral analysis of computer-mediated information exchange. We used real-world scenarios (DNA and fingerprint evidence collection instructions) to assess the efficacy of information transfer during various types of communication. Among these, bandwidth consistently had the most impact across all the conditions. It is notable that the high bandwidth scenarios outperform the low bandwidth scenarios in almost every case. For distractions, another study could explore more intrusive disruptions, such as audio loss. It is possible during this experiment that the distractions were not intrusive enough. Future work following this study could incorporate more intrusive disruptions such as noise distortion and other types of interruptions. The approach described in this study can be applied to refining communications in different domains such as telemedicine user interfaces to improve healthcare provider/patient portal user experiences.

References:

1. Dehais, F., Karwowski, W., & Ayaz, H. (2020). Brain at Work and in Everyday Life as the Next Frontier: Grand Field Challenges for Neuroergonomics *Frontiers in Neuroergonomics*, 1(1).

Acknowledgements: HA has equity in fNIR Devices LLC that licensed IP from Drexel University and manufactures the optical brain imaging sensor used in the study.

Assessment of Classification Algorithms for Determination of Cancerous Mammography Images

Madison Raza, B.S.,[1,2] Kendra Batchelder, M.A.,[1,2] Andre Khalil, Ph.D.[1,2]
[1]Department of Chemical and Biomedical, University of Maine, Orono ME.
[2] CompuMAINE Lab, University of Maine, Orono ME.

Introduction: Breast cancer has become the most common cancer, with approximately 300,000 new cases and 45,000 deaths per year in the United States.[1] Screening digital mammography is used to examine breast composition, where density is known to be an independent risk factor for breast cancer.[1,2] Approximately 50% of women have dense breasts characterized by the BI-RADS system. Density has the possibility to obscure masses due to similarity in presentation to tumors in mammography, 1 in 8 instances of breast cancer are missed in screening.[1] There is need to establish image-based risk assessment models which quantify breast composition. Gerasimova-Chechkina *et al.* and Marin *et al*. described the breast environment through quantification of spatial organization of mammographic tissue using a scanning window approach, a regular grid is defined by spatial organization characteristics of the mammogram. Three regions were identified fatty, healthy dense, and risky dense, where risky regions are areas with possible tumor associated tissue disruption.[3,4]

Methods: Spatial organization images generated from mammograms were analyzed using the Metric Space Technique.[3-5] A total of 78 cancerous and 20 benign mediolateral oblique (MLO) images were used for preliminary analysis. Each pixel represented a 256 x 256 section of the original mammogram and pixel intensity represented the level of spatial organization as quantified by the Hurst exponent via the 2D Wavelet-Transform Modulus Maxima method.[3,4] Pixel ranges between -0.2 and 0.45 represent anti-correlated spatial organization in fatty tissue, between 0.45 and 0.55 represent uncorrelated spatial organization in risky dense tissue, and between 0.55 and 1 represent long range correlated spatial organization in healthy dense tissue. The Metric Space Technique output functions, *i.e.,* the distribution of area, intensity, component, and filament morphology, were calculated for each patient.[5] The area under the curve of each tissue characteristic region, of each output function was assigned as metrics to each patient and were used to train classification algorithms. General linear models (glm) and k-nearest neighbor (KNN) models were trained with and without weights on different combinations of metrics and evaluated using ROC AUC statistics.

Results: Population statistics were analyzed for benign versus cancerous metrics using the Wilcoxon rank-sum test, *p*-values less than 0.05 indicated a statistically significant difference. Metrics with statistical differences were used to train classifier models for tumor classification as cancerous or benign. Looking at the distribution of components risky dense metric as the predictor for the glm ROC AUC score was 0.68 with 0.97 sensitivity and 0 specificity, for the KNN model (k = 7) ROC AUC of 0.75 with 0.9 sensitivity and 0.4 specificity, and for the KNN model with weights (k = 5) ROC AUC was 0.79 with 0.92 sensitivity and 0.1 specificity. The ROC curve for the KNN with and without weights for the distribution of components risky dense metric as the predictor can be seem in **Figure 1**. The distribution of component risky dense metric as a predictor indicates discrimination between the cancerous and benignclasses using the KNN model , but due to zero specificity it does not indicate

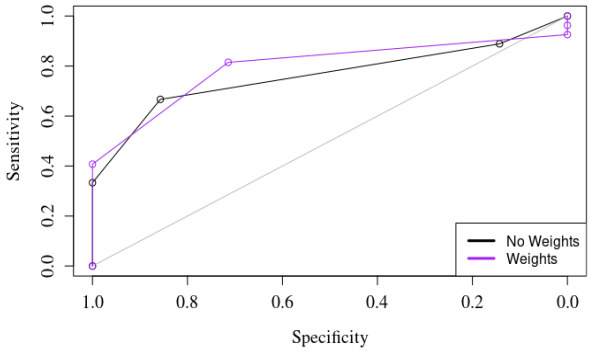

Figure 1. Representative ROC curve, where distribution of components risky dense metric was used to classify cancerous images in a KNN model.

discrimination of the glm model. Analysis for distribution of area and intensity was analyzed and determined to discriminate between cancerous and benign images based on the ROC AUC scores.

Conclusions: Generation of metrics from the Metric Space Technique output functions yielded statistical differences between benign and cancerous images. The metrics were used as predictors to train KNN and statistical general linear models. Due to class imbalance the general linear models yielded low specificity, prompting a move to KNN models. Based on the ROC AUC, and average specificity, and sensitivity of the resultant KNN models, the models yielded discrimination between benign and cancerous images from predictor metrics. Further work to finalize and test models on a more balanced dataset is needed.

References:

1. *Breast Cancer*. (2023). American Cancer Society. https://www.cancer.org/cancer/breast-cancer.html
2. Boyd N. et al. Lancet Oncol. 2005;6(10):798–808.
3. Gerasimova-Chechkina E. *et al*. Front Physiol. 2021;12(660883).
4. Marin Z. *et al*. Med. Phys. 2017;44(4);1324-1336
5. Adams F. ApJ. 1992;387:572-590.

Acknowledgments: The primary author would like to thank the Bioscience Association of Maine for providing a summer internship award in support of continued work at CompuMAINE Lab. Thank you to CompuMAINE members for support and a welcoming “home base”. Research reported in this publication was supported by the National Cancer Institute of the National Institutes of Health under award number R15CA246335.

Evaluating Synthetic Transmembrane Receptor-Peptide Ligand Interaction in Programed Mammalian Cells

Matthias Recktenwald, Sebastián L. Vega, Nichole Daringer
Rowan University

Introduction: In biology there are dynamic interactions between cells and the extracellular matrix (ECM). For instance, cells sense biophysical and biochemical signals in the surrounding tissue and respond by secreting matrix-modifying molecules that affect ECM stiffness and composition. Advances in synthetic biology have brought about the ability to program cells with transmembrane receptors that respond to soluble and cell-laden ligands; however, there is limited research investigating synthetic receptors capable of responding to material-laden ligands. Hydrogels are soft materials that can be designed to enable receptor-ligand interactions between programmed cells on (2D) or in (3D) and peptide-functionalized hydrogels. The long-term goal of this work is to merge synthetic biology and materials science to develop a new class of cell-hydrogel communication between cell receptors and peptides. Towards this, this abstract reports the programming of HEK293 cells with novel transmembrane cell receptors which results in the transcription of matrix modifying molecules upon binding with peptides that can be patterned onto hydrogels using a thiol-norbornene click chemistry.

Methods: The intracellular signaling platform was developed by Dr. Nichole Daringer during her postdoc training in the Collins lab. Briefly, it utilizes a reversible leucine zipper dimerization domain to recruit a CD3z substrate (S) towards one half of the receptor. The intracellular region of the other half of the receptor has a kinase specific to CD3z. Once phosphorylated, the substrate recruits a Zap70 SH2 domain (Figure 1A). Using this scheme, bringing together two split fluorescent proteins connected to the substrate and SH2 domains results in fluorescence which is measured using flow cytometry (manuscript in preparation).

Receptors were designed to bind to two orthogonal epitope tag peptides (HA or FLAG). Candidate receptors were identified *de novo* by using ten computationally derived amino acid sequences provided by the Pantazes research group. The optimal binding proteins were selected through sequential testing in biological quadruplet of the full platform in HEK293 cells by transfecting plasmids containing the genes for each receptor half, the split mNeonGreen halves connected to the substrate, and SH2 domains and a phosphatase to reduce background. After a 12-hour incubation, media was aspirated and replaced with 25 nmol of soluble peptides connected with a short flexible amino acid sequence. After 24 hours, the mean mNeonGreen expression levels of each sample were measured and reported in arbitrary units above the value of the background only samples (SH2, substrate domains and phosphatase only) from that round of testing.

To form hydrogels functionalized with peptides for receptor-ligand communication, hyaluronic acid macromers were modified with norbornene (NorHA) and reacted with di-thiol crosslinkers to form hydrogels. Unreacted norbornene groups in the hydrogels then underwent a second reaction to pattern hydrogels with thiolated ligand peptides of interest. Epitope tag peptide ligands were formed using a solid-state peptide synthesizer (CEM, Liberty Blue). The molecular weight of each peptide was verified using MALDI mass spectrometry. As proof of principle to demonstrate peptide patterning, thiolated HA-FLAG was synthesized with a GFP molecule, patterned using a striped photomask, and imaged using a confocal microscope.

Results: The receptors activated the intracellular domain of programmed HEK293 cells as evidenced by a significantly higher mNeonGreen expression in the peptide/receptor matched groups over the no ligand groups (One tailed T-test, p=0.05, n=4) (Figure 1B). MALDI results for each peptide suggested a yield of the expected amino acid sequence above 99%. Figure 1C shows MALDI for thiolated cFLAG-HA-GFM mass/charge spectra which has a 99.98% yield. This peptide was tethered to the NorHA scaffold in a vertical stripe pattern (Figure 1D).

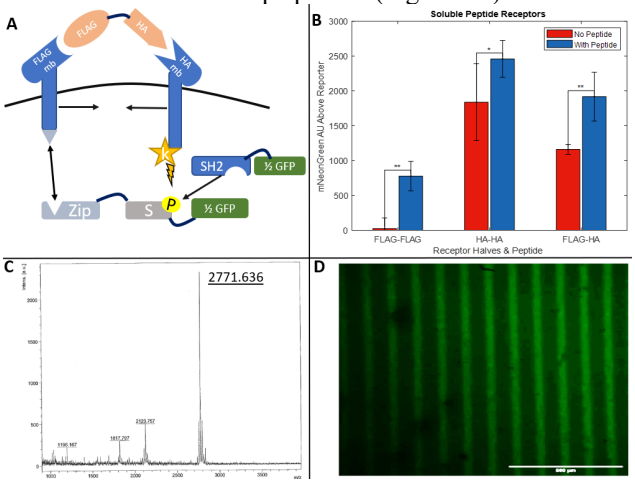

Figure 1. A) Schematic of HEK293 receptors. B) Soluble peptide receptor flow cytometry data. C) MALDI results with expected peak of 2271.6 m/z for cFLAG-HA-GFM peptide. D) Confocal microscopy image of photopatterned cFLAG-HA-GFM peptide in a NorHA scaffold.

Conclusions: Preliminary data shows that HEK293 transmembrane receptors selectively respond to soluble FLAG-HA peptide ligands by inducing a 2x fold increase in HEK293 mNeonGreen signal above background. FLAG-HA peptides can also be spatially tethered to NorHA hydrogels as evidenced by selective binding seen by confocal images of NorHA hydrogels photopatterned with a vertical stripe mask. Future work will focus on testing receptor-ligand communication of programmed HEK293 cells encapsulated in peptide-laden NorHA hydrogels and in transcription activation of other cell types including human mesenchymal stem cells.

Acknowledgements: The authors would like to acknowledge The Pantazes group and Dr. M. Benmassaoud for their contributions to this work and funding (NSF EAGER 2037055).

Title of Abstract: Fibrin network pore size drives the enzymatic degradation of blood clots

Rebecca Risman[1], Victoria Percoco[1], Mitali Shroff[2], Brittany Bannish[3], Valerie Tutwiler[1]
1) Rutgers University, Department Biomedical Engineering, Piscataway, NJ 08854
2) Rutgers University, Department of Cell Biology and Neuroscience, Piscataway, NJ 08854
3) University of Central Oklahoma, Department of Mathematics and Statistics, Edmond, OK 73034

Introduction: Blood clots perform a critical biological function in cessation of bleeding following injury. However, their function is transient and ultimately after performing their physiological function they must be resolved (fibrinolysis), through the cleavage of fibrin(ogen) by a fibrinolytic enzyme. Excessive, early fibrinolysis can lead to bleeding whereas impaired fibrinolysis can result in heart attacks and strokes (thrombosis). The balance of resolution is a critical step in preventing life threatening complications, however it is poorly understood how changes in the fibrin structure influence the biochemical regulation of fibrinolysis.

Methods: We used turbidimetric experiments to assess the biochemical regulation of intrinsic fibrinolysis and microscopy studies to characterize the microstructure for fibrinolysis in human blood plasma with varying fibrin network structure. Experiments are combined with a 3D stochastic multiscale computational fibrinolysis model to probe the individual influence of changes in network density, pore size, and fiber diameter. One-way ANOVA tests were performed using Prism 9.0 to compare fibrin network density behavior and scenario simulations.

Results: Experimental studies show that increasing fibrinogen concentration leads to changes in fibrin density, pore size, and fiber diameter and ultimately results in impaired fibrinolysis (Figure 1). Analysis of simulations and experiments indicate that the pore size of the fibrin network makes the most significant contribution to the rate of fibrinolysis (Figure 2). We show that this effect is strongly influenced by the ratio of protein:enzyme when compared to absolute enzyme concentration.

Conclusions: Our findings suggest that fibrin structure, particularly the pore size of the fibrin work which is altered in pathological conditions, is an important contributor for the development of enzymatic treatments with increased efficacy in treating bleeding and/or thrombosis.

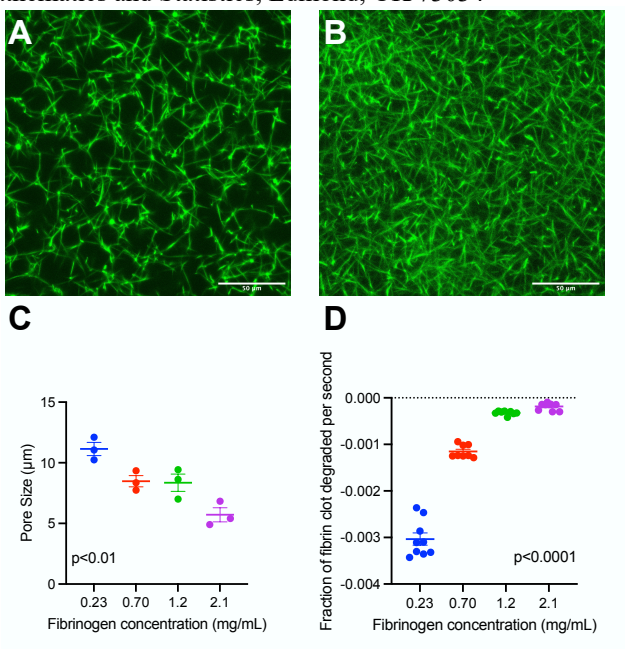

Figure 1. Loose (A) and dense (B) fibrin network densities were formed using concentrations of fibrinogen, as can be seen with confocal microscopy. Pore size (C) was measured from confocal microscopy images. Degradation rate (D) was measured from turbidimetric assays.

Figure 2. Clot scenarios with varying pore size, number of fibers, and fiber diameter were simulated using our model of fibrinolysis. Two scenarios with one different parameter (i.e., same number of fibers and fiber thickness, but different pore size) were compared. The fold differences of the degradation rates of the compact clot vs the uncompacted clot was compared. Comparing dense vs loose networks (i.e., changing pore size) showed the largest fold difference.

References:

1. Bannish BE et al. Sci Rep. 2017;7(1):6914
2. Risman RA et al. Biophys J. 2022; 121(17):3771-3285

Acknowledgements:
NIH R00HL148646-01 (V.T.); New Jersey Commission for Cancer Research COCR22PRF010 (R.R.); NIH T32 GM135141 (R.R.)

Smart CPR Trainer Abstract NEBEC 2023

Authors: Brigid Protzmann, Cassi Ronan, Robert Dillon, Stephanie Rodgers, Susan Freudzon, PhD.
Fairfield University

Need

The objective of the Smart CPR Trainer is to ensure proper CPR practices and certification. There is a need in the market to define the qualifications for life saving resuscitation to users. Users of the Smart CPR Trainer will be students training in cardiopulmonary resuscitation who are looking for real-time and post-performance feedback. Existing solutions on the market fail to provide users with informative feedback, which in turn leads to limitations in cardiopulmonary resuscitation performance. The goal of our design is to provide users with visible quantitative and qualitative feedback during CPR training.

Design Inputs

The design inputs for this project were based on feedback from physicians, nurses, and first responders trained in CPR. One of the main constraints for the Smart CPR Trainer's design is that it must fit in a commercially available mannequin used for CPR. The design incorporates a standard adult mannequin (Prestan), an Arduino circuit board, and ultrasonic distance and force resistive sensors.

The main priority for the Smart CPR Trainer is to provide a device that can be used with a commercially available CPR mannequin with a user-friendly application interface. It is critical that the design assesses CPR performance in accordance with the regulations defined by the American Heart Association; 100-120 compressions per minute reaching a depth between 2.0 and 2.5 inches.

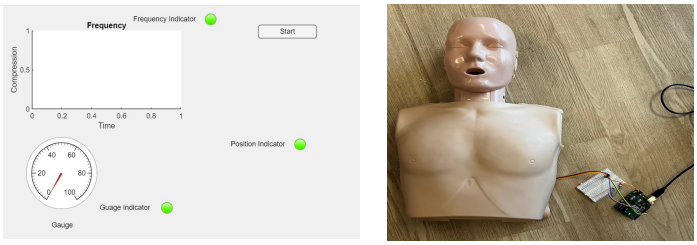

Figure 1: The Matlab app (left) features a start button, pressure gauge, and frequency graph. The Smart CPR Trainer (right) features the mannequin (Prestan), ultrasonic sensor, and Arduino circuit board.

Solution

The Smart CPR Trainer is designed to provide users with quantitative feedback during CPR training. An ultrasonic distance sensor is used to measure the depth of the user's chest compressions. Data obtained throughout training is collected using an Arduino microcontroller and displayed by a Matlab app, that shows the frequency and rate of chest compressions.

Verification Results

Verification testing was conducted to ensure the ultrasonic sensor was providing an accurate measure of compression depth during chest compressions. Nine wooden rods were cut to limit compression depth (1.5 inches and 3.75 inches). These rods were placed inside the mannequin next to the internal compression spring. Compressions were performed with the chest coming in contact with the top of each rod. The height of the rods were compared to the compression depth recorded by the ultrasonic sensor. During each trial, the ultrasonic sensor remained within 5% of the actual compressed depth.

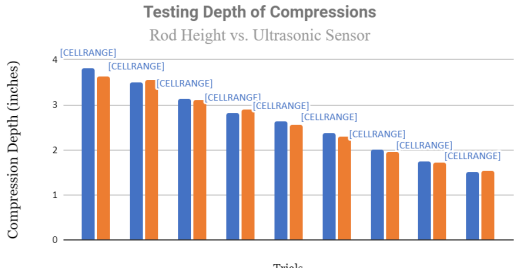

Figure 2: The graph shows the compression test results. The height of the wooden rods are shown in blue and the height measured by the ultrasonic sensor and Arduino are shown in orange.

Conclusion

Our design was successful in determining the depth of CPR chest compressions. The Smart CPR Trainer provides accurate qualitative and quantitative performance feedback within the adult mannequin device using the ultrasonic sensor and an Arduino and Matlab interface.

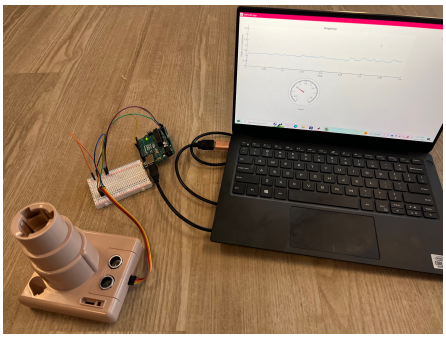

Figure 3: The compression spring and ultrasonic sensor connection with the Arduino circuit board, and a visual display of its interface with the Matlab app.

In order to increase the impact of our device in CPR performance testing we plan to run a series of usability tests with nursing students at Fairfield University. Compatibility testing with those that are CPR certified will ensure the practicality and usefulness to the device in the real world.

Acknowledgements

The Smart CPR Trainer Senior Design team would like to thank the Fairfield University Hardiman Scholars Fund for providing the necessary funding for this project.

Sensor Integration into Endovascular Rotating Hemostatic Valve

Grace Haas, Madeline Jones, Isabella Rosales, Michael West,[1] Douglas Yung, PhD[1], Hesham Masoud, MD[2]
[1]Biomedical and Chemical Engineering, Syracuse University, Syracuse, New York
[2]Cerebrovascular Clinic, Upstate Medical University, Syracuse, New York

1) User Need:

1.a) Use Case

Surgeons use rotating hemostatic valves (RHV) to control the entry of a guidewire and catheter into the bloodstream during endovascular surgeries[1]. An integral part of the hemostatic valve is the O-ring, the portion on the end of the RHV. It cinches on the catheter and wire and provides resistance for the doctor during surgery[1]. A torque is also used during the surgery to provide additional aid in pushing the wire and catheter through the RHV.

1.b) Problem Impact

Learning to perform an endovascular surgery is difficult due to the many bifurcations and complexities of blood vessels. Medical students' extensive practice does not fully prepare for real-time surgery[2,3]. This surgery is so difficult that companies have designed practice artificial patient models for students. However, these models are bulky, expensive, and inaccurate to real vasculature. The VIST® Lab from Mentice is a catheter lab training setup utilizing a full body mannequin and two fluoro/control screens. It is a very large model (requiring its own room) that is expensive for hospitals to house, while still not accurately portraying vasculature for practice.

1.c) Scope (Objective)

The goal of this project is to integrate sensors into the rotating hemostatic valve itself to gather force, distance traveled, and rotation data. Doctors and students will be able to view this data, improving teaching methods and facilitating precise control of these variables during surgery.

2) Design Inputs

2.a) Constraints:

Surgeons require free use of their hands during surgery, constricting design options to outside the surgeon's hand. Furthermore, surgeons all use a standard RHV design and might be unwilling to change to a different design, so another constraint is that the RHV structure must largely remain unchanged.

2.b) Requirements:

The most important design feature is readable, accurate data from force, linear displacement, and rotation sensors. Surgeons and students will use this data to analyze and improve their technique.

3) Solution

3.a) Design - Intended Use:

Using Autodesk Fusion 360, a more ergonomic model of the O-ring was designed and 3D printed with extrusion technology. This O-ring model can attach securely to any RHV, as its connection point is the same exact size and shape as existing O-rings. For the internal sensors, two rotary encoders were chosen to collect angular rotation and linear displacement data. A small insert will be placed into the second encoder to rotate as the catheter and guidewire travel over it, which will transfer into linear displacement of the wire.

3.b) Build - DEMO

The encoders were housed within the new O-ring model, and the force sensor was fixed to the torque. In addition to the encoders, a battery, wireless charging transmitter, and Adafruit board were housed in the model.

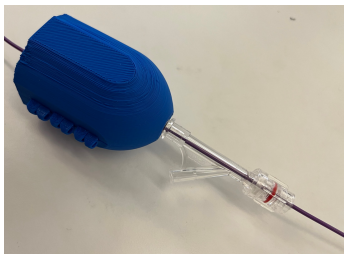

Figure 1: RHV O-ring housing with internal encoders

4) Verification Results

4.a) Introduction (i = 1 … N)

Force, linear displacement, and rotation data must be readable and accurate.

4.b) Methods (i = 1 … N)

Force data was taken with a force gauge to compare with sensor data. Linear measurements with a caliper were taken to confirm accuracy of linear encoder.

4.c) Results (i = 1 … N)

Results verified that solution accurately measured data.

5) Conclusion

5.a) Summary:

The O-ring in an RHV can be enlarged to accommodate internal sensors, and the torque can be adapted with force sensors. From these points, accurate force, rotation, and linear displacement data can be measured.

5.b) Revisions:

Scaffolding must be optimized to fit all internal sensors, charging components, and data transmission parts, and this optimization will decrease model size for ease of surgeon use. In addition, the model can be manufactured from plastic that can be sterilized for operating room use.

5.c) Impact (Future Version):

With these improvements, doctors will be able to adapt any RHV to be 'smart' and use the data collected to set quantifiable goals for students on how to improve their surgical technique.

References:

1. Namba K. et al. Intervent Neurorad. 2007;13;51-53
2. Ghumman SS. et al. Amer Jour of Cardio. 2022;170;160-165
3. Young J. et al. Ann Intern Med. 2011;155:309-315

Acknowledgements: We would like to thank Syracuse Office of Undergraduate Research and Creative Engagement and the SU Bioengineering and Chemical Engineering Department for funding this work.

Insulin-like Growth Factor Biomaterial Driven Intracellular Signaling for Peripheral Artery Disease Treatment

Abhishek Roy[1], Joseph Dodd-o[1], Zain Siddiqui, PhD[1], Erika Aguas, PhD[2], Arslan Hashmi[1], Aisha Khan[1], Yoshifumi Kobayashi, PhD[3], Emi Shimizu, PhD[3,4], Vivek Kumar, PhD[1,4]

1. Department of Biomedical Engineering, New Jersey Institute of Technology, Newark, NJ, 07102, 2. Department of Biomedical Engineering, Rutgers University, Piscataway, NJ, 08854, 3. Department of Oral Biology, Rutgers School of Dental Medicine, Newark, NJ, 07103, 4. Department of Endodontics, Rutgers School of Dental Medicine, Newark, NJ, 07103

Introduction: Peripheral Artery Disease (PAD) results from plaque-driven occlusion of vasculature and causes peripheral ischemia, impaired gait and claudication. Approximately 8.5M people in the US suffer from PAD, costing the healthcare system approximately $60B/yr. Although smaller diameter blood vessel replacements of the occluded femoral and popliteal arteries may reperfuse this ischemic tissue, arteriosclerosis within micro vessels remain unaddressed. Addressing this issue requires a biomaterial that is injectable, degradable and provides sustained angiogenic while preserving myogenic signaling response. We have developed a self-assembling peptide (SAP) hydrogel-based platform, termed SLIGF, to promote these properties through an IGF receptor binding peptide and to potentially regenerate microvasculature and muscle preservation within the lower extremities.

Methods: The SLIGF-IGFR interaction was characterized by static docking using Rosetta FlexPepDock, followed by 200ns molecular dynamics simulation using GROMACS with a CHARMM036 forcefield to probe the electrostatic and van der Waals binding. Additionally, the number of hydrogen bonds and the intermolecular contacts were quantified across the 200ns trajectory. The peptide was synthesized using solid phase peptide synthesis and the purity and identity was confirmed with HPLC and ESI-MS. The structural and mechanical characteristics were determined using FTIR, CD, SEM, AFM, and rheology. The downstream of IGF receptor signaling was detected by Western blot analysis. The angiogenic and the myogenic efficacy of the biomaterial was tested using tube formation and myoblast fusion assay. Ongoing work seeks to optimize the IGF-1c mimic through computational modeling and to improve mimic presentation by doping peptide domains with glycine spacers and addition of the self-assembling sequence.

Results: Hydrogen bond analysis performed on the original peptide, mimic, and SL-conjugated mimic indicates conservation of key hydrogen bonds between the peptide ligand and IGFR; further substantiated by the similar intermolecular contact scores. Our preliminary data has shown the ability for this biomaterial to be thixotropic, injectable, biodegradable, cytocompatible in vitro (C2C12 cells) and biocompatible in vivo (subcutaneous implants in Wistar rats). Additionally, we demonstrate angiogenic capability and increased Akt phosphorylation (downstream of IGF receptor signaling) which indicates cell myotube hypertrophy. (Figure 1). Similarly, to our previously published studies [1], these hydrogels degrade over a 1-month period with significant cellular infiltration and matrix deposition.

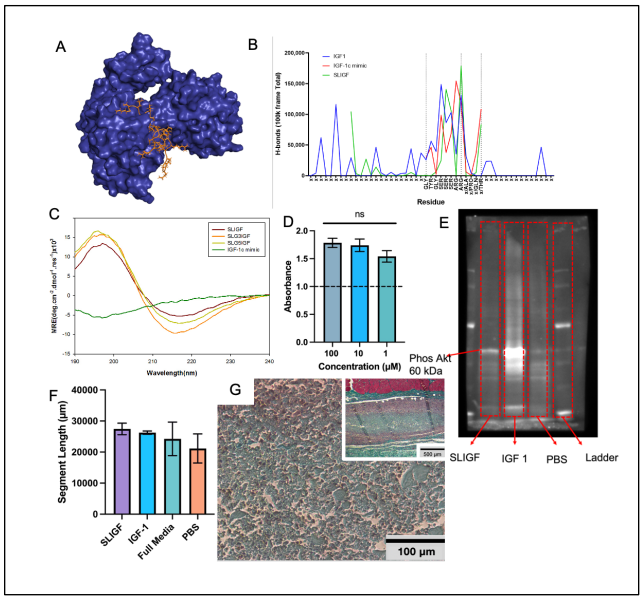

Figure 1: (A) SLIGF-IGFR complex (B) Hydrogen bond analysis (C) Circular dichroism (D) Cytocompatibility (CCK8 assay) (E) Phos-Akt western (F) EC tube formation (G) Biocompatibility

Conclusion: The proposed work investigates rational design of SAP hydrogels for myogenesis and angiogenesis within poorly vascularized tissues and may offer an alternative biomaterial strategy for revascularization. Further, potential augmentation of the IGF mimicking peptide with glycine spacers may provide new insights into the therapeutic strategies involving myogenesis and angiogenesis. Ultimately, we aim to develop an off-the-shelf acellular biomaterial to guide in vivo microvasculature regeneration and muscle perseveration for treatment of PAD.

References:

1. Siddiqui, Z., et al., Angiogenic hydrogels for dental pulp revascularization. Acta Biomater, 2021. 126: p. 109-118.

Acknowledgements: We thank Dr. Jonathan Grasman, NJIT Undergraduate Research and Innovation (URI) program and the National Science Foundation (NSF) for supporting the project.

Fabrication of Nanoparticles loaded Microparticles for Sustained and Targeted Delivery of Zoledronate to Activated Macrophages for the Modulation of Inflammation in Osteoarthritis

Paul Sagoe[1, 2], Yohely Espiritusanto[1, 2], Era Jain, PhD[1, 2]
1 Department of Biomedical and Chemical Engineering, 2Bioinspired Institute, Syracuse University, Syracuse, NY

Introduction. Synovitis is now increasingly being recognized as a major contributor to osteoarthritis (OA) progression and pain. Inflamed synovium is often associated with an influx of cells, particularly macrophages that release pro-inflammatory and catabolic mediators upon activation[1]. As a result, targeting activated macrophages represents a promising therapeutic strategy to modify disease outcomes of OA. Bisphosphonates (BPs) are a class of drugs that exhibit high affinity and toxicity against macrophages; however, their rapid clearance from the joint renders them ineffective when administered via intraarticular injection[2,3]. To overcome this limitation, we have developed a novel therapeutic system based on nanoparticles in microparticle formulation (NiM) for the sustain and target delivery of zoledronate (Zol), a potent third-generation BP, to activated macrophages for the treatment of OA.

Methods: Polymeric microparticles(MP) made up of Polyethylene glycol- polylactic-co-glycolic acid (PEG-PLGA; Sigma Aldrich) were synthesized using a coaxial flow-phase separation method and characterized using a bright-field-inverted microscope. Calcium-complexed Zol nanoparticles(CaZol NP) were synthesized via a reverse micro emulsification method. Further characterization of CaZol NP was done by dynamic light scattering (DLS) and transmission electron microscope (TEM). Loading of CaZol NP into microparticles (CaZol NIM) was achieved by adding the nanoparticles in suspension to the organic phase (PEG-PLGA in dichloromethane) used for the microparticle preparation. Successful encapsulation of Zol in CaZol NIM formulation was confirmed by Fourier transform infrared (FTIR) and energy-dispersive x-ray (EDAX). The pH-responsive behavior of CaZol NP and CaZol NiM formulations was studied with inductively coupled plasma–optical emission spectroscopy(ICP-OES). To study the uptake of particles using confocal microscopy, Raw 264.7 macrophages were stimulated with lipopolysaccharides (LPS; Invitrogen) and treated with coumarin6-labeled particle formulations for 2 hours.

Results: The average size of microparticles and nanoparticles were determined as 6.7±3.4 µm and 44.6±3.1 nm respectively (Fig. 1 A, B). The quantified value of Phosphorus(P) from EDAX for CaZol NP, CaZol NiM, and PEG-PLGA MP(control) relative to carbon and oxygen were 7.93%, 0.23%, and 0% respectively. The FTIR spectrum of the Zol and CaZol particles showed a characteristic C-N stretching band at 1580 cm^{-1} and a broad C=C stretching band at 1452 cm^{-1} due to the vibration in the imidazole ring in Zol. Additionally, the presence of the phosphate group in Zol was confirmed by 1150 cm^{-1} and 1070 cm^{-1} bands which correspond to P=O and a P-O stretching respectively[4]. The strong band at 1748 cm^{-1} corresponds to the C=O stretch in LA and GA of PLGA, and the characteristics peak at 1083 cm^{-1} showing the C-O-C stretch confirms the presence of PEG. Compared to CaZol NP, the release behavior at both acidic and neutral pH showed a minimization of initial burst release for CaZol NiM(Fig.1C). This finding was further supported by uptake studies wherein a higher uptake level of coumarin6-labeled nanoparticles was observed for the CaZol NP formulation compared to the CaZol NiM, indicating the sustained release potential of the latter.

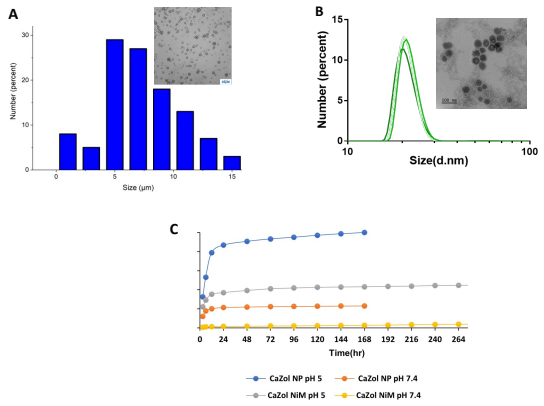

Fig1 A) PEG-PLGA microparticles characterization **B)** TEM and DLS characterization of CaZol nanoparticles **C)** In-vitro Release of CaZol NP and CaZol NiM at pH 5.0 and 7.4

Conclusions: Altogether, we were able to successfully encapsulate nanoparticles in microparticles and achieve pH-sensitive sustained release. Given the ability of PEG-PLGA microparticles to act as a suitable external carrier to tune drug release, limit drug movement to non-specific tissues, and incorporate targeting ligands; loading Zol as nanoparticles into microparticles promises to enhance the drug's efficacy for the curative treatment of OA.

References:

1. Kraus et al., Osteoarthritis and Cartilage (2016)
2. Murat, et al. Knee Surgery, Sports Traumatology, Arthroscopy (2015)
3. Thea and Holen., Journal of translational medicine (2011)
4. Au, K.M.,et al., Biomaterials, 82, pp.178-193

Acknowledgments: This work was supported by DoD Discovery Award W81XWH-22-1-0020 and CUSE funds by Syracuse University.

A Smart-Assistant & Augmented-Reality Display integrated BCI Targeting At-home Use for People Living with ALS

Mohammad Sahal[1], Tim Bunker[1], Yashodha Ravichandran[1], Grace Feldman[1],
Terry Heiman-Patterson, MD[2], Hasan Ayaz, PhD[1].
1 School of Biomedical Engineering Science and Health Systems, Drexel University, Philadelphia, PA 19104 USA
2 Temple University, Lewis Katz School of Medicine, Philadelphia, PA 19140 USA.

Introduction: Amyotrophic lateral sclerosis (ALS) is an idiopathic, fatal neurodegenerative disease of the human motor system [1]. People living with ALS (PALS) experience progressive, and rapid loss of voluntary movement, potentially leading to a locked-in clinical state [2]. Given the progressive loss of motor function including the ability to speak, PALS could significantly benefit from using a Brain Computer Interface (BCI) since BCIs offer an opportunity for communication (by spelling) and environmental control (TV, lights, etc.) that is independent of a caregiver, providing increased independence and restored autonomy which leads to improved quality of life [3]. Recently, BCI technology has also been used within smart homes to control appliances [4]. BCI-based smart homes are useful since adapting smart home technology for BCI use creates access to existing technologies that were previously inaccessible to PALS. In this abstract we aim to expand our earlier work [6] and present preliminary results with Augmented Reality (AR) integrated P300 BCI to enable PALS to select predefined environmental control commands in an in-home setting.

Methods: A team visited the participants' homes to set up a smart home demo. The participants went through a short calibration before testing the system on a traditional monitor as well as on an AR headset. We used 10 trials with 10 repetitions per selection both for calibration and online runs. The P300 matrix was a 3x3 icon matrix displaying icons for the following commands: weather update, stream Netflix on TV, stop streaming, news update, turn on/off smart light, play music, stream security camera feed on tv and stop. The calibration was first done on a traditional monitor after which the participants ran online runs to control the smart devices with both Google Assistant (Home Mini) and Amazon Alexa (Echo 3rd Gen). The same process was repeated on the AR headsets. We used System Usability Scale (SUS: survey to test system usability) [6] and Nasa Task Load Index (TLX: survey to determine individual task load while using an interface) [7] to gauge the subjective usability of the system.

Results: The proposed system was tested with three PALS and three healthy controls. The pilot study showed accuracies of up to 100% on traditional computer screen and up to 75% on AR headset on PALS. There was no relation between the severity of ALS and accuracy. Preliminary results show that the lower the ALSFRS-R score (19-33) (more progressed ALS) the higher the SUS score (97.5-45). There was no significant relation between the severity of ALS symptoms in PALS and their TLX score (6.7 – 45.8). This preliminary work suggests that not only are PALS able to use this system, but they find it easy to use without significant fatigue or effort.

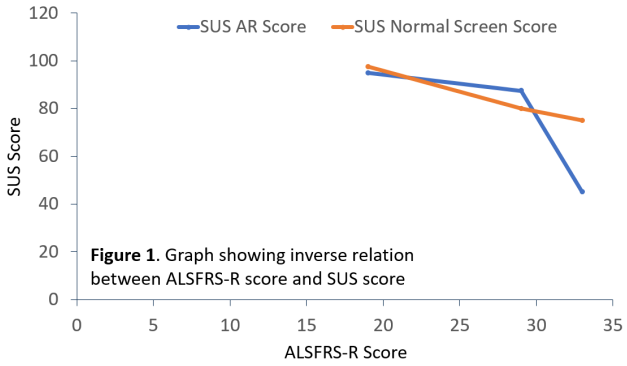

Figure 1. Graph showing inverse relation between ALSFRS-R score and SUS score

Conclusions: Integration of smart assistants in a mobile P300 BCI interface advances assistive technology to improve the quality of life of PALS. The overall system is smart assistant brand agnostic. The current system was tested with basic functions on Amazon Alexa and Google Assistant. Although preliminary, it is interesting that those PALS that were most severely affected found the systems most useable. These initial results show promise of the widespread applicability and usability of the system. Further testing will be needed to test the robustness of the system with more complex commands and with other smart assistants. Testing will also be needed in an open-world environment. We are working in collaboration with the ALS Hope Foundation and the MDA/ALS Center of Hope clinic in Philadelphia, PA to deliver and set-up Results our systems in the homes of PALS to serve their daily needs.

References:

[1] Matthew, et al (2011). Amyotrophic lateral sclerosis, The Lancet, Volume 377, Issue 9769.
[2] Keon, et al (2021). Destination Amyotrophic Lateral Sclerosis. Frontiers in neurology, 12, 596006.
[3] Holz, et al (2015). Long-Term Independent Brain-Computer Interface Home Use Improves Quality of Life of a Patient in the Locked-In State: A Case Study. Physical Medicine and Rehabilitation, 96(3), S16-S26.
[4] Kosmyna, et al (2016). Feasibility of BCI control in a realistic smart home environment. Frontiers in human neuroscience, 10, 416.
[5] Sahal, et al (2021). Augmented Reality Integrated Brain Computer Interface for Smart Home Control. Springer.
[6] Brooke, (1995). SUS: A quick and dirty usability scale. Usability Eval. Ind. 189.
[7] Hart, et.al (1988), "Development of NASA-TLX (Task Load Index): Results of empirical and theoretical research." Advances in psychology. Vol. 52.

Acknowledgements: We would like to acknowledge all the undergraduate students from Drexel's CoNQuER Lab that have worked on the project and the MDA/ALS Center of Hope for continued collaboration.

BioFlow: A Modular Low Cost Perfusion System for *In Vitro* Studies

Jaselin M. Rodriguez, Jasdeep Singh, Esha Navaneethakrishnan, Ramita Sajankila, Jordan E. Hungreder, Jonathan M. Grasman, PhD
Department of Biomedical Engineering, New Jersey Institute of Technology, Newark, NJ

1) User Need:

1.a) Use Case

BioFlow functions as a cost-effective, modular perfusion system that enables 2, 4, or 8 samples to be run in parallel, utilizing a single peristaltic pump.

1.b) Problem Impact

Multi-sample, perfusion systems, designed for academic research applications, typically cost over $2000. BioFlow is a cost-effective alternative that can accommodate up to 8 samples and costs $641 to construct.

1.c) Scope (Objective)

BioFlow aims to increase throughput, utilizing modular and bifurcation design techniques to evenly distribute flow and shear stress onto 2, 4, or 8 samples simultaneously.

2) Design Inputs

2.a) Constraints:

The device must accommodate multiple samples using a single medium reservoir and single peristaltic pump. The device must also fit inside an incubator (<17.5 x 18.5 inches) and be cost-effective (<$700).

2.b) Requirements:

Components of the BioFlow that are in direct contact with biological reagents must be biocompatible. Bioflow must allow for multiple samples to be placed within the system, without leakage. Additionally, consistent/similar shear stress must be exerted onto the samples (0.162), regardless of the number of samples being used.

3) Solution

3.a) Design - Intended Use:

BioFlow **(Fig 1)** consists of a peristaltic pump, cell medium reservoir, tubing, custom-built sample inserts (designed for 2, 4, or 8 samples), and corresponding sample holders with end ports (**Fig 2**), all designed in a modular fashion for enhanced functionality and user experience.

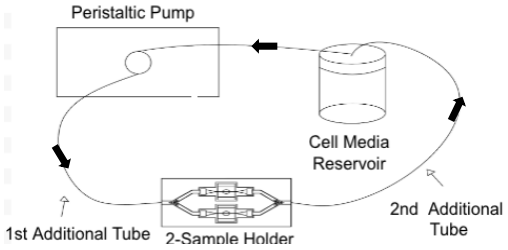

***Figure 1**. Schematic of BioFlow (any sized sample holder can be inserted into workflow).*

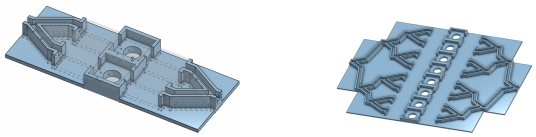

***Figure 2**. 3D CAD model of 2 and 8-sample holder.*

3.b) Build - DEMO

A 3D-printed PLA sample holder accommodates two samples with indents to stabilize the tubing and hold everything in place (**Fig 3**). The bifurcated design employs Y-connectors to allow for equally distributed fluid flow throughout. Luer locks connect the tubing to the needle, which is inserted into the PDMS mold for sample loading, and there is a window in the base to visualize the sample.

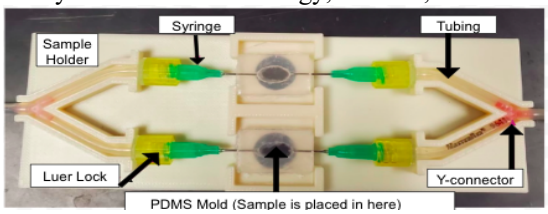

***Figure 3**. Structural design of 2-sample prototype*

4) Verification Results

4.a) Introduction (i = 1 … N)

Fluid modeling software (ANSYS) and prototype testing shall be conducted to validate systems requirements.

4.b) Methods (i = 1 … N)

Simulation of the different configurations shall verify that consistent shear stresses are exerted onto samples in each sample holder configuration; the required flow rate for 2, 4, and 8 sample holders should be 2, 4, and 8 times the input flow rate of single channel systems (0.0821 m/s), respectively. A test run of the 2-sample configuration was performed to demonstrate functionality of the device.

4.c) Results (i = 1 … N)

The simplified 2-sample ANSYS model verified consistent flow rate (0.062 m/s) (**Fig 4A**) and a median pressure of 0.048 Pa (**Fig 4B**) subjected onto the two samples. We were able to achieve the target flow rate 0.162. A shear stress of 2 Pascals should be favorable in supporting endothelial cells in the sample holder [1].

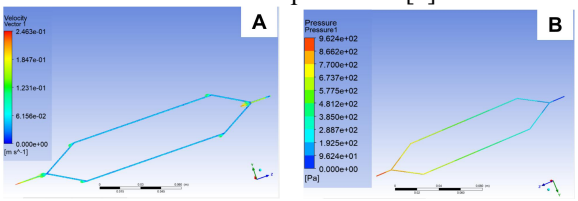

Figure 4: ANSYS results for simplified 2-sample holder assessing (A) velocity and (B) pressure in the device.

The 2-sample prototype testing revealed no leakage, demonstrating successful implementation of the design.

5) Conclusion

5.a) Summary:

Prototype testing of the 2-sample holder confirmed modularity and functionality of the system. Integration and use of the 4, and 8-sample holders is still in the testing phase. Overall, with our product we can greatly increase throughput and reproducibility in web labs, at a fraction of the cost compared to our competitors.

5.b) Revisions:

Testing of the 4-sample and 8-sample configurations are still required. Further ANSYS modeling is required to ensure similar shear stress and validate required flow rates.

5.c) Impact (Future Version):

The geometry of the design may be modified to increase the number of samples that can be integrated into the system.

References

1. Vion AC et al. “Endothelial cell orientation and polarity are controlled by shear stress and VEGF through distinct signaling pathways,” Frontiers (Volume 11) 2021.

Acknowledgements: We acknowledge funding from NJHF (PC14-22) and startup funds provided by NJIT